Li-ION TRANSPORT AND OPTICAL MODULATION IN THIN-FILM BATTERY ELECTRODES

Von der Fakultät Chemie der Universität Stuttgart
zur Erlangung der Würde eines
Doktors der Naturwissenschaften (Dr. rer. nat.)
genehmigte Abhandlung

Vorgelegt von

Yug JOSHI

aus Kanpur, Indien

Hauptberichter:	Prof. Dr. Guido Schmitz
Mitberichter:	Prof. Dr. Joachim Maier
Prüfungsvorsitzender:	Prof. Dr. Oliver Clemens

Tag der mündlichen Prüfung: 27. Juli 2021

Institut für Materialwissenschaft (IMW) der Universität Stuttgart

2021

Abstract

The optical modulation of lithium manganese oxide ($LiMn_2O_4$, LMO) and lithium titanate ($Li_4Ti_5O_{12}$, LTO) due to Li-ion insertion is quantitatively characterized. Ion beam sputtering is used to deposit the layers of respective materials on top of already sputtered platinum which acts as the current collector/reflector. The structure and morphology of the layers were probed using X-ray diffraction, scanning electron microscopy, and transmission electron microscopy. Well-defined intercalation states were prepared electrochemically and investigated by optical spectrometry in reflectance geometry. The obtained dispersion curves were then modeled using the Clausius-Mossotti dispersion equation to obtain the complex refractive index as a function of wavelength at various intercalation states.

A continuous change in the effective resonant wavelength with lithium intercalation was observed. This was found to be consistent with the evolution of the band structure upon ion insertion. In LMO, two significant resonances were identified in the visible region of the spectrum, which shifts with the degree of intercalation. By associating this shift with the evolving band structure, the resonances were attributed to electronic transitions between the O-2p band and the split Mn-d band.

In the case of LTO, the mechanism and effect of the phase transformation (from spinel structured $Li_4Ti_5O_{12}$ to rock-salt type $Li_7Ti_5O_{12}$ upon lithium insertion) on the optical response is studied. The same model (using Clausius-Mossotti dispersion) unveils the presence of one and two major resonant wavelengths/frequencies in the case of $Li_4Ti_5O_{12}$ and $Li_7Ti_5O_{12}$, respectively, in the UV/visible/NIR region of light. The single resonance in the case of $Li_4Ti_5O_{12}$ is allocated to a transition from O-2p to Ti-t_{2g} i.e., across the band-gap. Whereas for the $Li_7Ti_5O_{12}$ phase, the two resonances were characterized for the electronic transitions from O-2p to empty Ti-t_{2g} and from filled Ti-t_{2g} to empty Ti-e_g. The concentration dependence of the

derived dielectric constants indicates a fast lithium-ion transport through the grain boundaries. This helps in nucleating the grain boundaries with a conductive lithium-rich phase. This increases the electronic conductivity of the thin films in the initial stages of intercalation and explains the debated understanding of the fast dis-/charge capability of $Li_4Ti_5O_{12}$ electrodes on a nanoscale.

On a micrometer scale, the diffusion is controlled by the bulk diffusion. To investigate the kinetics of lithium migration at this length scale, an innovative technique is developed that employs optical microscopy in a constrained region of the sputtered thin-film sample. At this constrained region, lithium is blocked from entering the LTO structure directly from the electrolyte. Therefore, the technique enables the observation of the lateral transport of lithium through the electrode due to the optical contrast generated in this material during the ion insertion and subsequent phase transformation. The poor diffusivity of lithium in its end phases (or $Li_4Ti_5O_{12}$ and $Li_7Ti_5O_{12}$) is confirmed but, this poor diffusivity challenges the notion of high dis-/charging performance reported in this material. Surprisingly, the movement of the phase boundary is hindered which has been refuted in prior reports. However, this hindrance is confirmed here by the slow, linear growth kinetics of the Li-rich phase in the initial stages of the lithium transport. Interestingly, the partial solubility of lithium in the spinel structured $Li_{4+\delta}Ti_5O_{12}$ phase increases the diffusivity of lithium in this spinel phase drastically. This drastic increase in diffusivity along with the reduction in the size of the electrode seems to be compensating for the kinetic hindrance experienced by the phase boundary.

Kurzfassung

In dieser Arbeit wird die optische Modulation bei der Einbringung von Li-Ionen in Lithiummanganoxid ($LiMn_2O_4$, LMO) und Lithiumtitanat ($Li_4Ti_5O_{12}$, LTO) quantitativ charakterisiert. Dafür werden dünne Schichten der jeweiligen Materialien mittels Ionenstrahlsputtern auf einer zuvor gesputterten Platinschicht abgeschieden. Die Pt-Schicht fungiert dabei als Stromkollektor / Reflektor. Die Struktur und Morphologie der hergestellten Dünnschichten werden mittels Röntgenbeugung, Rasterelektronenmikroskopie und Transmissionselektronenmikroskopie untersucht. Nach der elektrochemischen Herstellung und Einstellung definierter Interkalationszustände werden diese durch optische Spektrometrie in Reflexionsgeometrie untersucht. Die erhaltenen Dispersionskurven werden dann basierend auf der Clausius-Mossotti-Dispersionsgleichung modelliert, um den komplexen Brechungsindex als Funktion der Wellenlänge bei verschiedenen Interkalationszuständen abzuleiten.

Es wird gezeigt, dass die Variation der effektiven Resonanzwellenlänge mit der Änderung der Bandstruktur des jeweiligen Materials bei der Lithium-Interkalation übereinstimmt. In LMO gibt es zwei signifikante Resonanzfrequenzen im sichtbaren Bereich des Wellenlängenspektrums, die sich mit dem Interkalationsgrad verschieben. Diese werden auf elektronische Übergänge zwischen dem 2p-Band von Sauerstoff und dem geteilten d-Band von Mangan zurückgeführt.

Im Fall von LTO wird zusätzlich der Einfluss der Phasenumwandlung von spinellstrukturiertem $Li_4Ti_5O_{12}$ zu $Li_7Ti_5O_{12}$ (Steinsalz-Typ) auf die Lithiuminsertion untersucht. Die Modellierung auf Basis der Clausius-Mossotti-Dispersion offenbart hierbei das Vorhandensein von einer, im Falle von $Li_4Ti_5O_{12}$, bzw. von zwei, im Falle von $Li_7Ti_5O_{12}$, Hauptresonanzwellenlängen / -frequenzen im UV / sichtbaren / NIR-Frequenzbereich des Lichts. Die Einzelresonanz der $Li_4Ti_5O_{12}$-Phase kann einem Übergang von O-2p zu Ti-t_{2g} (über die Bandlücke) zugeordnet werden. Dahingegen

entsprechen die Resonanzen der $Li_7Ti_5O_{12}$-Phase den elektronischen Übergängen von O-2p zu leerem Ti-t_{2g} und von gefülltem Ti-t_{2g} zu leerem Ti-e_g. Die Abhängigkeit der abgeleiteten Dielektrizitätskonstanten von der Konzentration weist auf einen schnellen Lithiumionentransport durch die Korngrenzen hin, wodurch es zur Ausscheidung einer leitenden Lithium-reichen Phase an den Korngrenzen kommt. Dies erhöht die elektronische Leitfähigkeit der Dünnschichten in den Anfangsstadien der Interkalation und erklärt das umstrittene Verständnis der schnellen Entlade- / Ladefähigkeit von $Li_4Ti_5O_{12}$-Elektroden zumindest im Nanobereich.

Im Mikrometerbereich wird die Diffusion durch die Volumendiffusion gesteuert. Um die Kinetik auf dieser Längenskala zu untersuchen, wird ein innovatives Verfahren entwickelt, um den lateralen Transport von Lithium in einem eingeschränkten Bereich der Dünnschichtelektrode mittels optischer Mikroskopie zu beobachten. Die Veränderung des optischen Kontrasts, der in diesem Material während der Phasenumwandlung erzeugt wird, emöglicht die Messung der Kinetik des Lithiumtransports. Dabei kann das schlechte Diffusionsvermögen von Lithium in seinen reinen Endphasen ($Li_4Ti_5O_{12}$ und $Li_7Ti_5O_{12}$) bestätigt werden, was allerdings nicht die hohe Entlade- / Ladeleistung erklärt. Zusätzlich behindert die Phasengrenze die Lithiumausbreitung, was in früheren Berichten bestritten wurde. Dies kann hier jedoch durch die lineare Wachstumskinetik der Li-reichen Phase in den Anfangsstadien des Lithiumtransports experimentell demonstriert werden. Interessanterweise erhöht die Teillöslichkeit von Lithium in der spinellstrukturierten $Li_{4+\delta}Ti_5O_{12}$-Phase die Reaktionsrate drastisch, was die kinetische Hinderung an der Phasengrenze zu kompensiert scheint und die Fähigkeit zum schnellen Entladen / Laden eines Elektroden Partikels endlicher Größe erklären würde.

Table of Contents

1 Introduction

Energy is needed to power everything, even life itself. The way of energy production has evolved over the centuries, and so has its storage and distribution (not in regards to the biochemical reaction, for which the mitochondria and the chloroplast are responsible). At present, we are surrounded by a plethora of gadgets and tools which are powered directly by batteries. Obviously, these batteries are needed to be charged/replaced from time to time, but their importance in our daily lives cannot be denied, ranging from powering gadgets for everyday use like a watch, a car to life-saving tools like a pacemaker for someone's heart.

1.1 Lithium-ion batteries

The batteries that exist today represent the culmination of more than 200 years of work which was initiated by Luigi Galvani at the University of Bologna, Italy, and by Alessandro Volta at the University of Pavia, Italy. They both had a different explanation for the twitching of a dead frog's leg when it came in contact with two metallic wires. This led Alessandro Volta to develop the first electrochemical cell (in 1800) using a series of zinc and silver plates separated by a cloth socked in sodium chloride solution (Voltaic pile).[1] The discovery provided, for the first time, a reliable source of direct current until 1831. In that year Michael Faraday gave the operating principle of electric generators. Although the working principle of the 'pile' in terms of 'contact tension' between the metals, as proposed by Volta, was disproved by Michael Faraday's laws of electrolysis in 1834[2], the significance of the 'pile' cannot be underestimated. Following the invention of the 'pile' huge progress took place in the 19th century in terms of electrochemical batteries. In 1859, a French scientist Gaston Planté invented the first rechargeable (or secondary battery) lead-acid battery. Subsequently, in 1866, a French engineer, Georges-Lionel Leclanché revealed his design of a battery based on a zinc-rod as a negative electrode (anode) and a manganese oxide–carbon mixture as a positive electrode

(cathode) immersed in an aqueous ammonium chloride solution. Soon after, in 1901, Swedish engineer Waldemar Jungner invented a rechargeable nickel-cadmium battery.[3] The progress however slowed at the beginning of the 20th century. But, in the late 20th century with the increase in demand for portable electronics and the development of medical implants, the need for batteries with an increased power density and long battery life was felt. This led to a shift from zinc, or any other material, to lithium. The choice fell on lithium due to its very low reduction potential of -3.04 V vs the standard hydrogen electrode, and its low molar weight (6.94 $g \cdot mol^{-1}$). This results in a very high gravimetric capacity of 3862 $mAh \cdot g^{-1}$. The first lithium (-iodine) based primary or non-rechargeable battery came to existence in late 1969, with some of them still in use today.[3] However, the prospect of using pure lithium metal as a secondary battery electrode has a severe safety issue. The formation of lithium dendrites upon multiple charging cycles causes short circuits and result in thermal runaways. This was the primary reason that intercalation reaction-based electrodes, where the ion can be inserted and removed reversibly (for instance MS_2, *M*=Ta, Nb, Ti, Mo, and transition metal oxides), were explored since the 1970s. However, they could be commercialized in a rechargeable battery only in 1991 by Sony.[4] The problem of short circuit and thermal runways was solved by the use of two different intercalation-based materials for both cathode and anode[3], an idea demonstrated by Scrosati and Lazari in 1980[5]. Sony used $LiCoO_2$ as cathode material (reported by Goodenough in 1981[6]) and hard carbon as anode material for their battery, which undergoes the following reaction:

At Anode: $$6C + z\mathrm{Li}^+ + ze^- \rightarrow \mathrm{Li}_z\mathrm{C}_6 \qquad \textit{1-1a}$$

At Cathode: $$\mathrm{LiCoO}_2 \rightarrow \mathrm{Li}_{1-z}\mathrm{CoO}_2 + z\mathrm{Li}^+ + ze^- \qquad \textit{1-1b}$$

The above battery was coined as a “rocking-chair battery” or lithium-ion battery, where the concentration difference of the lithium ions is used to create a potential difference between the electrodes. This potential difference is what powers a

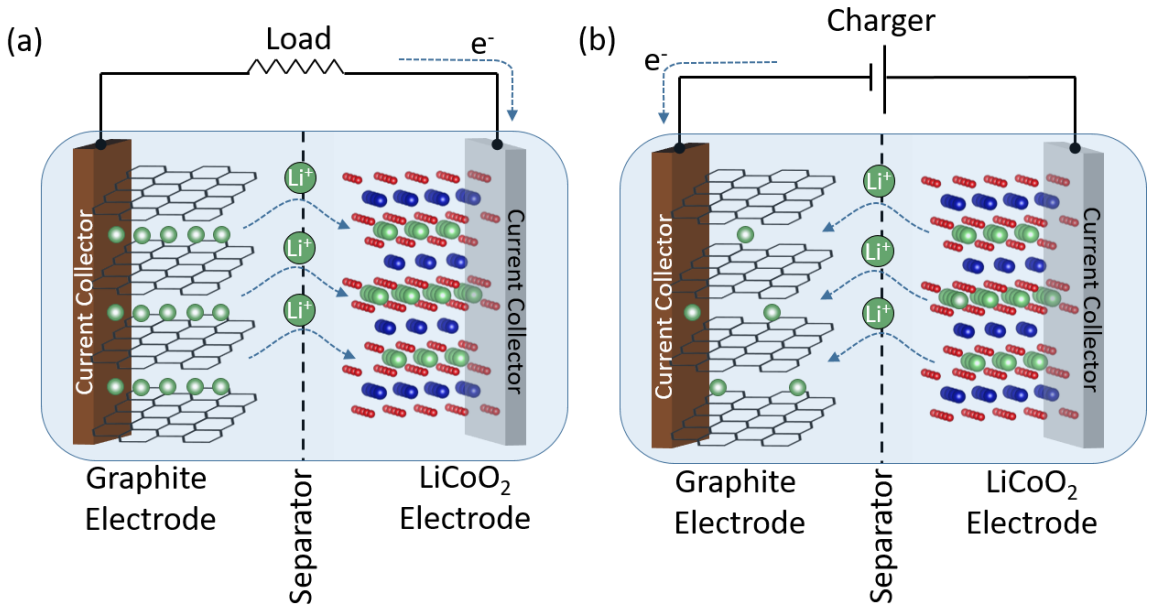

Figure 1-1: *(a) Discharging and (b) charging of a lithium ion battery. In the $LiCoO_2$ electrode, the green, blue and red atoms are of lithium, cobalt and oxygen, respectively.*

battery. During dis-/charging a battery, the lithium ions move from one electrode to the other via the electrolyte which is usually a salt of lithium dissolved in organic solvents. In the above chemical reactions (Equation 1-1a and 1-1b), the forward reaction signifies the charging of the battery where the potential difference between the cathode and the anode is increased by increasing the difference in the concentration of lithium between the two electrodes. The processes of dis-/chargin are schematically represented in Figure 1-1. To date, various materials have been commercialized for such lithium-ion batteries. These include $LiCoO_2$[6], $LiMn_2O_4$[7], $LiFePO_4$[8,9] etc. as cathode material, and Hard carbon, Graphite, $Li_4Ti_5O_{12}$,[10] etc. as anode material. Moreover, continuous research is being conducted for exploring new materials.

The specific gravimetric capacity of a material (Q_{th}) or the amount of charge in mAh that a material can store per unit gram is given by Equation 1-2 as[11]:

$$Q_{th} = \frac{1000 \cdot z \cdot \mathrm{F}}{3600 \cdot \mathrm{M_w}} \qquad 1\text{-}2$$

where M_w is the molecular weight ($g \cdot mol^{-1}$), F is the Faraday's constant, and z is the charge taken by a mole of material, i.e., number of moles of the inserted species in a mole of the host material times the valence of the inserted species.

The migration of lithium ions from either of the electrodes changes the electronic structure around the atoms and, consequently the band structure of the material, which in turn causes a change in the electronic properties of the electrode. Since, the electronic and optical properties are related to each other, by dis-/charging a battery electrode, its optical properties can also be modified. As the optical response/change is not a primary task of a battery, not much attention is given to this property in the battery research community. However, electrochromic (EC) materials exploit this very principle to achieve a change of color by varying the metal-ion concentration electrochemically. Such materials are generally used in applications such as smart windows and mirrors etc.[12]

1.2 The optical behavior of Electrochromic materials

Color of a material is nothing but the frequency of light emitted by it. However, most of the materials don't emit light/electromagnetic (or EM) radiation/energy spontaneously and are dependent on external stimuli, be it thermal, electromagnetic, etc. Hence, the perception of color depends on the type/energy of the stimuli.

Light is composed of electromagnetic radiation (for visible light the wavelength varies from 450 nm to 750 nm), the energy of this radiation E_λ is given by Equation 1-3[13]:

$$E_\lambda = \frac{hc}{\lambda} = h\nu \qquad 1\text{-}3$$

where h, c, λ, and ν are the Planck's constant, speed of light in vacuum, the wavelength of the radiation, and the frequency of the radiation, respectively. Whenever this energy is incident on a material, it can either be absorbed, reflected, or transmitted. The absorptions can be due to either electronic or atomic

vibrations, the latter occurs in the case of infrared (IR) light. Transmission is mostly due to the presence of a band-gap, in the electronic structure of a material, which is larger than the incident photon energy. Reflection, predominantly, is due to the presence of free electrons or due to the overlap between the valence band and the conduction band which results in: (i) spontaneous excitation and relaxation of electrons thereby reflecting/emitting light; (ii) high absorption coefficient when a photon tries to penetrate through the material. The material property governing these different phenomena can be quantified by a single term, the 'Complex Refractive Index' (CRI) given by Equation 1-4[14]:

$$n_l^*(\lambda) = n_l(\lambda) - i \cdot k_l(\lambda) \qquad 1\text{-}4$$

where, n_l^* is the complex refractive index of a material 'l', n_l is the real part of CRI which is the ratio of phase velocity of light in vacuum to that in medium 'l' and k_l is the imaginary part of CRI describing the absorption of light quantifying the attenuation of light as it is traversing through the medium in accordance with Beer-Lambert's law[15,16], see later Equation 1-7. Mathematically, the CRI can be defined using various models such as Cauchy's method,[17] Sellmeier dispersion formula,[18] Lorentz dispersion,[19] etc. The Cauchy's and Sellmeier dispersion formulae are empirical relations lacking a physical justification whereas the Lorentz dispersion formula is based on a physical representation of an atom. It is derived by considering that an incident EM wave forces the electron cloud, held together by the positively charged nucleus of an atom, to oscillate. This representation resembles a spring-mass system, where the continuously varying electric field from the incident EM wave applies a force on the electron cloud held by a restoring spring force. It results in the oscillation of the electrons with a natural frequency, ω_o ($\omega_o = \sqrt{k_E/\mathrm{m_e}}$, where k_E is the spring constant and $\mathrm{m_e}$ is the mass of the electron). In the case of gases, the electrons from neighboring atoms do not interact with each other due to less atomic density. Hence, in this case, usually there is no damping due to the neighboring atoms. Therefore, a simple spring-mass

system without any damping can describe the displacement and consequently the polarization, which is related to the dielectric constant. From the dielectric constant the refractive index can be obtained to be[20]:

$$n_\alpha^* = 1 + \frac{N\mathrm{q_e^2}}{\epsilon_o \mathrm{m_e}} \sum_j \frac{f_j}{\omega_{0j}^2 - \omega^2} \qquad 1\text{-}5$$

where, N is the number of electrons per unit volume, $\mathrm{q_e}$ is the charge of an electron, ϵ_o is the permittivity of free space, f_j is the strength of the j^{th} oscillator, ω_{oj} is the resonant frequency of the oscillator, and ω is the frequency of incident electromagnetic (EM) wave ($\omega = 2\pi c/\lambda$).

In the case of high pressurized gases or metals, the electrons from the neighboring atoms influence each other. This can be described by a frictional force which results in damping of the oscillator and consequently in dissipation of its energy in the form of heat. When this additional damping term is considered, the refractive index can be written as[20]:

$$n_\alpha^* = 1 + \frac{Nq_e^2}{\epsilon_o m_e} \sum_j \frac{f_j}{\omega_{0j}^2 - \omega^2 + i \cdot \omega\gamma_j} \qquad 1\text{-}6$$

where, γ_j is the damping of the j^{th} oscillator. As is clear from the above equation this damping term is responsible for the 'complex' nature of the refractive index which is represented in Equation 1-4, with a real and an imaginary part. According to Beer-Lambert's law[15,16], the attenuated amplitude of the incident EM wave is given by[14]:

$$A = A_0 \cdot e^{-\frac{2\pi}{\lambda} k \cdot L} \qquad 1\text{-}7$$

where A_0 and A are the initial and final amplitude of the EM wave, L is the optical path length, k is the imaginary part of CRI.

Finally, in the case of a dense non-metallic medium, an additional contribution of an induced electric field resulting from the polarization of neighboring atoms or molecules (forming a dipole) has to be considered. This results in Equation 1-8.

$$\frac{(n_\alpha^*)^2 - 1}{(n_\alpha^*)^2 + 2} = \frac{N q_e^2}{3\epsilon_o m_e} \sum_j \frac{f_j}{\omega_{0j}^2 - \omega^2 + i \cdot \omega \gamma_j} \qquad 1\text{-}8$$

The above equation is known as the Clausius–Mossotti[21,22] relation. Throughout this study, this relation is used to describe the CRI of the material.

From the nature of Equation 1-8 and 1-4, it is clear that the real and imaginary parts of the refractive index are related to each other. Therefore, it should be possible to extract the real part of CRI if the imaginary part is known and vice-versa, this is quantitatively given by the Kramers-Kronig relation[14,23,24].

As has been mentioned before, when an EM wave is incident on a material, it can either be absorbed, reflected, or transmitted. The amplitude of the electromagnetic wave, as a consequence of reflection from an interface, is the product of incident amplitude and the reflection coefficient. The reflection coefficient (r_{lm}) is given by Fresnel's equation which is given in Equation 1-9[25] when light enters medium m from medium l (assuming normal incidence).

$$r_{lm} = \frac{n_m^* - n_l^*}{n_m^* + n_l^*} \qquad 1\text{-}9$$

Using the definition of the CRI as per Equation 1-8 and the Fresnel's reflection coefficients, the intensity of reflected light emerging from a multilayer stack after incurring multiple reflections at the interfaces can be obtained, as has been shown by O.S. Heavens.[26] The final expression, derived for an opaque platinum back layer representing the sample geometry used in this thesis, is presented and employed in Chapter 3 section 3.3.

In a quantum mechanical picture, the electronic transitions from one energy level to another can be represented in the same way as in Equation 1-8, the difference

being the definition of the strength of the oscillator. This term will now signify the transition probability and can be described as[14]:

$$f_{ij} = \frac{2m_e\omega_{ij}}{3\hbar}|\langle j|r|i\rangle|^2 \qquad 1\text{-}10$$

where f_{ij} is the strength of the oscillator for a transition from i^{th} to j^{th} energy level, ω_{ij} is the frequency of the transition being equal to the resonant frequency. In Equation 1-10, the matrix element on the right-hand side originates from Fermi's golden rule.

As stated previously, EC materials change their color upon electrochemical insertion of ions which signifies a change in their CRI. A change in CRI will also change the intensity and wavelength of the propagating light. In a quantum mechanical language, this modulation of the CRI is due to the filling of the band structure with electrons brought by ion insertion. This results in a modification of electronic transitions energy, and/or changes in the Fermi level, in the band structure of the material i.e., ion insertion will lead to a change in ω_{ij}, $|\langle j|r|\rangle i|$ in Equation 1-10 and/or γ_j and ω_{0j} in Equation 1-8.

A typical EC device consists of a stack of an EC material, an ion-conductive membrane, and a mixed ionic/electronic storage layer which is either electrochromically not active or its action complements the effect of the primary EC layer. Optically transparent and electronically conducting electrodes are added on top of the outer electrodes which act as current collectors. By controlling the external voltage, the mobile ions are shifted back and forth between the storage and the EC layer[27].

To date, WO_3 is the state-of-the-art EC material applied in smart windows and mirrors. The electrochromic behavior of WO_3 was first reported in 1930[28]. It was caused by the absorption of hydrogen ions. Later in 1969, another study reported the optical change in WO_3 when exposed to UV light[29]. In 1984, the optical response was documented upon lithium intercalation[30]. Since the optical response is due to

a change of the electronic band structure via intercalation, a similar optical function, if not better, can be expected for any battery electrode material.

So far it has been established, that ion insertion leads to a change in CRI, which is the origin of the EC effect. However, the swiftness of the change of CRI has to be governed by the kinetics of ion insertion. Therefore, this EC effect can, in principle, be used to investigate the migration of lithium in the electrodes. To implement this concept, a basic understanding of the physics of atomic and ionic migration is crucial, which is introduced briefly in the subsequent sections.

1.3 Kinetics of atomic migration

1.3.1 Solid-State diffusion

The phenomenon of intermixing/movement of atomic species had long been acknowledged and utilized before its quantitative description by Adolf Fick in 1855[31]. Prior to his work, the first quantitative description was given by Thomas Graham. Graham studied the inter-diffusion of gases in 1833[32] and proposed that the rate of diffusion of a gas is inversely proportional to the square root of its density. This was refuted by Fick in 1855 with his work focusing on the diffusion of salt in water.[33] He made a direct analogy between the phenomenon of mass transport and heat conduction. The latter had already been described by Fourier in 1807.[33] Fick proposed that the driving force for diffusion was the 'solution density'. For solids this can be replaced by the concentration of the atomic species and therefore the diffusion flux in a single direction, J can be written as[33]:

$$J = -D\frac{\partial C}{\partial x} \qquad 1\text{-}11$$

where D is the diffusion coefficient, C is the concentration and x is the diffusion length. Equation 1-11 is known as Fick's first law. While Fick's first law is used for steady-state conditions, Fick's second law is generally used to determine the concentration as a function of time. It is described in Equation 1-12 for a constant diffusion coefficient:

$$\frac{\partial C}{\partial t} = -\frac{\partial J}{\partial x} = D\frac{\partial^2 C}{\partial x^2} \qquad 1\text{-}12$$

In 1905, Albert Einstein[34] and a Polish scientist Marian Smoluchowski[35], independently, gave a physical explanation of atomic migration based on the random jumps or the Brownian motion of atoms. These random jumps are originating from the thermal vibrations of the atoms, and the diffusion coefficient is linked to the mean free displacement of atoms. The jumping rate depends on the respective energy of the lattice site and the energy barrier required for each jump.

For chemical diffusion or inter-diffusion of atoms, the random jumps are more favorable towards a lower Gibbs free energy state, i.e., the flux due to atomic movement is associated with the gradient of the chemical potential (or molar free energy), as proposed by Onsager in 1931[36]. If the chemical potential is constant throughout there will be no average movement of the atomic species. Therefore, the flux can be defined by Equation 1-13[37]:

$$J = -M \cdot \frac{\partial \mu}{\partial x} \qquad 1\text{-}13$$

where M is the mobility of atoms. Now, for dilute solutions the chemical potential can be defined as the following equation:

$$\mu = \mu_0 + k_b T \ln c \qquad 1\text{-}14$$

where μ_0 is a constant, k_b is the Boltzmann constant, T is the Temperature, and c is the mole fraction. Substituting the definition of chemical potential in Equation 1-13 yields Fick's first law. Now, from Equation 1-11, 1-13, and 1-14 the mobility can be expressed as a function of diffusion and mole fraction as[37]:

$$M = D \cdot c/(k_b T) \qquad 1\text{-}15$$

Concentration-dependent diffusion

As highlighted before, Equation 1-12 is valid for a constant diffusion coefficient. While a constant diffusion coefficient is often a reasonable starting assumption,

however, the diffusivity of lithium in a number of the battery materials is reported to be significantly concentration-dependent.[38–41] This is probably because lithium atoms diffuse via interstitial vacancies, hence the migration will depend on the occupancy of lithium or the number of available interstitial sites. To check if the diffusion coefficient is concentration-dependent or not, the concentration profiles induced by the diffusion of atoms should be considered. If these profiles do not resemble the analytical solution obtained by solving the differential equation given in Equation 1-12, then the diffusion coefficient is most likely varying with the concentration. For instance, the solution of Equation 1-12 for a semi-infinite diffusion with a constant concentration on one end is given by an error function. If in this case, the experimentally obtained concentration profiles are not representing an error function, the diffusion coefficient is probably concentration-dependent and, hence will also vary with location. In such cases, Equation 1-12 is invalid and there would be an additional term in the equation arising from the gradient in the diffusion coefficient. The evolution of the concentration would now follow the equation:

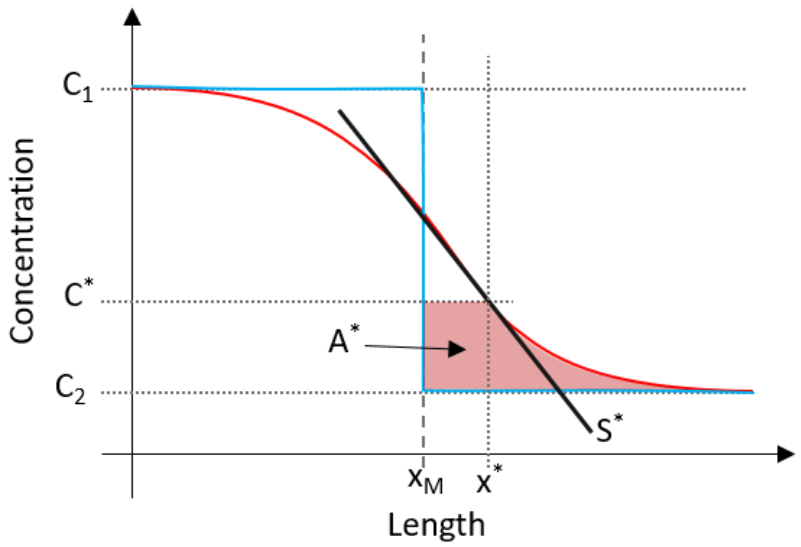

Figure 1-2: *Concentration profile before diffusion (blue curve) and after inter-diffusion (red curve). The shaded area (A*) shows the area considered in the Boltzmann-Matano method, S* is the slope of the concentration profile at a concentration of C* and x_M marks the position of the Matano plane.*

$$\frac{\partial C}{\partial t} = -\frac{\partial J}{\partial x} = \frac{\partial}{\partial x}\left(D\big(C(x)\big)\frac{\partial C}{\partial x}\right) = \frac{\partial D}{\partial x}\cdot\frac{\partial C}{\partial x} + D\frac{\partial^2 C}{\partial x^2} \qquad 1\text{-}16$$

The above differential equation has no general analytical solution. And therefore the determination of the diffusion coefficient is not possible directly. However, for an inter-diffusion experiment, starting with a step like concentration profile (see blue curve in Figure 1-2) and with the appropriate boundary conditions (described later), the above equation can be transformed into an ordinary differential equation, by substituting Equation 1-17 into equation 1-16.[37,42,43]

$$\zeta = \frac{x - x_M}{\sqrt{t}} \qquad 1\text{-}17$$

In the above equation, x_M represents the position of the Matano plane which acts as a reference plane in an inter-diffusion experiment. For the geometry considered in Figure 1-2, the position of x_M is determined iteratively by equating the areas, bounded by the concentration profile and the y-axis of the Matano plane, on either side of the plane. With the substitution of Equation 1-17, Equation 1-16 transforms to:

$$-\frac{\zeta}{2}\cdot\frac{\partial \mathrm{C}}{\partial \zeta} = \frac{\partial}{\partial \zeta}\left(D(C)\cdot\frac{\partial \mathrm{C}}{\partial \zeta}\right) \qquad 1\text{-}18$$

The above equation can be integrated within the limits of C* and C_2 yielding the following equation:

$$-\frac{1}{2\sqrt{t}}\int_{C_2}^{C^*}(x - x_m)\cdot\partial \mathrm{C} = D(C^*)\cdot\left.\frac{\partial \mathrm{C}}{\partial x}\right|_{x^*} - D(C_2)\cdot\left.\frac{\partial \mathrm{C}}{\partial x}\right|_{x_\infty} \qquad 1\text{-}19$$

The integral on the left-hand side represents the shaded area, A*, in Figure 1-2. Now, if the gradient of concentration at the terminating concentration (for instance say C_2) tends to zero, the second term on the right-hand side of the Equation 1-19 becomes zero. And finally, the diffusion coefficient can be obtained

at concentration C* by determining the shaded area (A*) and the slope of the concentration profile at C* (marked by S* in Figure 1-2) as:

$$D(C^*) = -\frac{1}{2\sqrt{t}} \cdot \frac{1}{\partial C/\partial x}\bigg|_{x^*} \cdot \int_{C_2}^{C^*} (x - x_m) \cdot \partial C \qquad 1\text{-}20$$

Two-phase reaction

The previous sub-section clarified the methodology to obtain the concentration-dependent diffusion coefficient. In this sub-section, we'll see the effect of phase

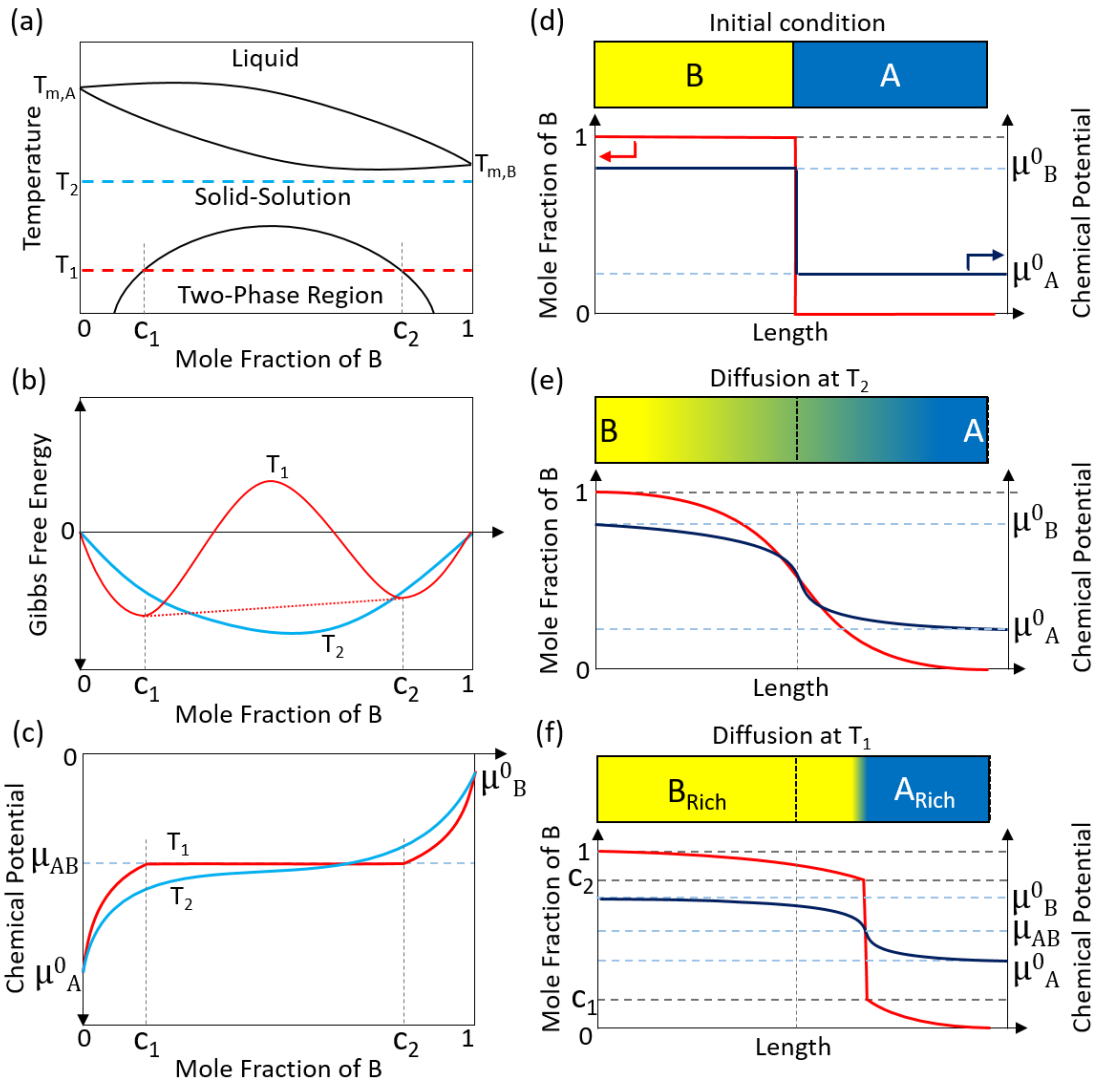

Figure 1-3: *(a) Exemplary phase diagram of a binary A-B alloy. (b) Gibbs free energy curve at two selected temperature, T_1 in the two-phase region and T_2 in the single phase region. (c) The respective chemical potential at the two temperatures. (d) The initial condition for an inter-diffusion experiment for the A-B couple, i.e., a bar of B is joined to a bar of A. Inter-diffusion of B and A after some time, t, at temperature corresponding to a (e) solid-solution, and/or (f) two-phase region.*

separation on the concentration profiles. The phase separation or a two-phase reaction is shown by some of the well-known battery materials, e.g. $LiFePO_4$ and $Li_4Ti_5O_{12}$, etc. The evolution of the concentration profiles in such cases can be understood by considering the definition of the flux in terms of chemical potential as given by Equation 1-13.

Let's start by considering a hypothetical binary system A-B, having a phase diagram similar to Figure 1-3 (a). In the solid-state section of the phase diagram, two regions can be identified, a solid-solution region and a two-phase region. The corresponding (hypothetical) Gibbs free energy curves for these regions are given in Figure 1-3 (b), marked by T_1 and T_2 for the two-phase and solid solution region, respectively. Now, the molar free energy or the chemical potential is nothing but the change of Gibbs free energy per unit change in concentration, mathematically given as:

$$\mu_A = \left.\frac{\partial G}{\partial n_A}\right|_{T,P,n_B} \qquad 1\text{-}21$$

In the above equation, μ_A is the chemical potential of A at constant temperature (T), pressure (P), and number of moles of B (n_B); G is the Gibbs free energy; n_A is the number of moles of A. The corresponding chemical potential for the two conditions i.e., solid-solution and two-phase region, are given in Figure 1-3 (c). As is clear from the figure, in the two-phase region the chemical potential is constant, whereas for the case of solid-solution the chemical potential varies monotonously.

Now, consider a hypothetical inter-diffusion experiment initiated by joining two semi-infinite bars of A and B, and having a step-like concentration profile as shown in Figure 1-3 (d). Consequently, the chemical potential is also a step function (solid dark-blue line in the figure). Now, as stated before the difference in the chemical potential is what drives the migration of atoms. But depending on the temperature (be it T_1 or T_2) the concentration profile will be different as shown in Figure 1-3 (e) and (f) for T_2 and T_1, respectively. For the solid-solution case or T_2, see Figure 1-3

(e), all the concentrations of A in B and/or B in A are possible as is apparent from the Gibbs free energy curve in Figure 1-3 (b). However, in the two-phase region or at T_1, the Gibbs free energy for the concentration between c_1 and c_2 is marked by the common tangent between the minima of the individual Gibbs free energy of the two phases, as shown by a dotted red line in Figure 1-3 (b). Any solubility of A in B and/or B in A which results in a concentration between c_1 and c_2 must be stabilized by phase separation. Therefore, in the inter-diffusion experiment, any concentration between c_1 and c_2 is impossible. Hence, a sharp phase boundary is obtained as shown in Figure 1-3 (f). However, the chemical potential remains a continuous function as is seen by the solid blue line in Figure 1-3 (f). The net movement of the phase boundary arises from the differences in the inter-diffusion coefficients, assuming the vacancy concentration is in equilibrium on either side of the phase boundary for a substitutional diffusion mechanism. The solution of Fick's second law, Equation 1-12, for the concentration profile remains the same for either side of the phase boundary, however, a sharp concentration jump marking the phase boundary cannot be directly obtained by the standard Fick's law described in terms of concentration, Equation 1-12. But, when the flux is written in terms of chemical potential, as in Equation 1-13, and subsequently multiplying and dividing by ∂c we obtain Equation 1-22:

$$J = -M \cdot \left(\frac{\partial \mu}{\partial c}\right) \cdot \frac{\partial c}{\partial x} \qquad 1\text{-}22$$

In the two-phase region i.e., between c_1 and c_2, the term in the bracket becomes zero as the chemical potential remains constant. Therefore, a concentration between the solubility limits is hardly obtained, and if they do, the further incoming or outgoing flux will drive the reaction such that the phase separates and the concentration will either be greater than c_2 or less than c_1. Hence, a concentration profile can be modeled for a two-phase reaction using the finite-difference method as has been shown in the work of Erdélyi and Schmitz[44].

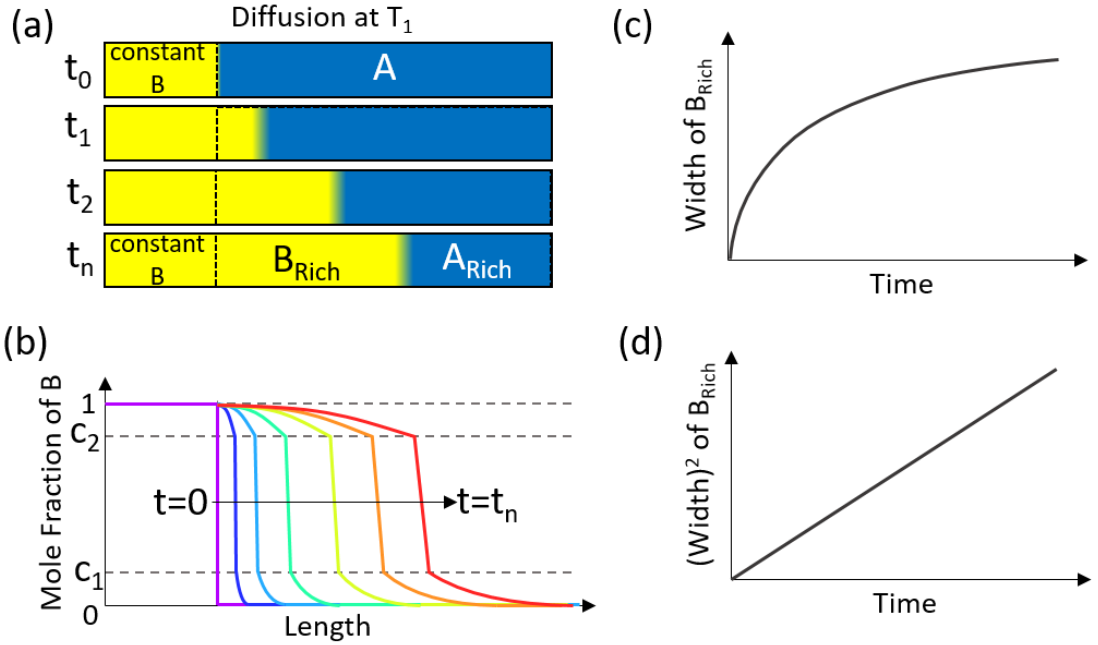

Figure 1-4: *(a) A schematic of an inter-diffusion experiment used in this thesis, the concentration on the left side is maintained constant. t_0 represents the starting condition, t_i is some arbitrary time after the diffusion of atoms have started. (b) The concentration profiles at different times from the inter-diffusion experiment shown in (a). (c) The parabolic growth of the B_{Rich} phase versus time. (d) The square of the width of the B_{Rich} phase versus time.*

A two-phase semi-infinite diffusion

Now considering the same A-B system, as discussed above, but a simpler experimental geometry (which will be eventually utilized in Chapter 5 of this thesis) as shown in Figure 1-4 (a). In this geometry, the concentration on one side is maintained constant and only the B_{Rich} phase is growing with time. The hypothetical concentration profiles are shown in Figure 1-4 (b).

Now, if there is no hindrance at the phase boundary, using finite difference to solve Equations 1-12, 1-13 and using an appropriate definition of μ, the growth of the B_{Rich} phase can be modeled in a similar way as done by Tomán et al.[45]. This results in a parabolic growth i.e., the width of the B_{Rich} phase is proportional to the square root of time as shown in Figure 1-4 (c) and (d). The figures (c) and (d) are essentially the same, only in Figure 1-4 (c), the width is plotted as a function of time whereas in Figure 1-4 (d), the square of width is plotted versus time. From the slope of Figure

1-4 (d), the averaged diffusion coefficient (independent of concentration) can be directly evaluated. A more detailed description is given in the subsequent section.

1.3.2 Effect of interfaces: Linear to parabolic behavior

In the previous sub-section, a case of migration of atoms in a two-phase material has been discussed. However, certain deviations have been found experimentally from the ideal picture described before.[46] This is especially true for phase growth in some silicon-based[47–49] and hydrogen-based[50,51] compounds. In these cases, it has been reported that in the initial stages of atomic migration, a linear phase propagation (as is shown in Figure 1-5 (b)) is observed rather than the conventionally assumed parabolic dependence. This has been explained by the existence of a kinetic barrier at the phase boundary (defined here as barrier coefficient, κ).

For simplicity, let the B-rich phase be named β-phase and the A-rich phase be named σ-phase. Considering Figure 1-5 (a) as the hypothetical concentration profile after some time. The movement of the phase boundary by an amount dw in time dt needs $(c^{\beta}_{min,\kappa} - c^{\sigma}_{max}) \cdot \rho \cdot dw$ atoms. Where ρ is the atomic density, $c^{\beta}_{min,\kappa}$ is the non-equilibrium concentration of the β-phase due to the existence of the barrier coefficient and c^{σ}_{max} is the equilibrium concentration in σ-phase. The respective concentrations are shown in Figure 1-5. Now, from mass conservation[52]:

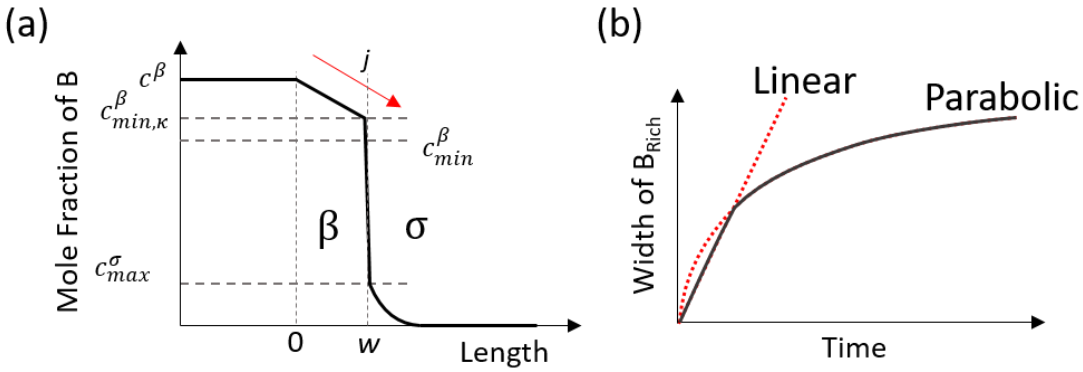

Figure 1-5: *(a) A hypothetical concentration profile for the semi-infinite geometry. (b) The linear to parabolic transition for the growth of the β-phase.*

$$\left(c^{\beta}_{min,\kappa} - c^{\sigma}_{max}\right) \cdot \rho \cdot dw = j \cdot dt \qquad 1\text{-}23$$

where j is the incoming flux of atoms. Rearranging Equation 1-23 gives:

$$\frac{dw}{dt} = \frac{1}{\rho \cdot \left(c^{\beta}_{min,\kappa} - c^{\sigma}_{max}\right)} \cdot j \qquad 1\text{-}24$$

Assuming a constant concentration gradient in the β-phase, the flux under a diffusion-controlled growth through the β-phase is written according to Fick's first law as:

$$j = \rho \cdot D^{\beta}_{Li} \cdot \frac{\left(c^{\beta} - c^{\beta}_{min,\kappa}\right)}{w} \qquad 1\text{-}25$$

where c^{β} is the maximum solubility of lithium in the β-phase. But, in a steady-state condition, practically the same flux needs to cross the interface, which is in terms of the barrier coefficient, κ is[46]:

$$j = \rho \cdot \kappa \cdot \left(c^{\beta}_{min} - c^{\beta}_{min,\kappa}\right) \qquad 1\text{-}26$$

where c^{β}_{min} is the lower solubility limit of lithium in β-phase, in equilibrium condition. Now, using Equations 1-25 and 1-26, the flux in terms of equilibrium concentrations can be written as:

$$j = \frac{\rho \cdot D^{\beta}_{Li}}{\left(w + {D^{\beta}_{Li}}/{\kappa}\right)} \cdot \left(c^{\beta} - c^{\beta}_{min}\right) \qquad 1\text{-}27$$

From Equation 1-27 and 1-26, the non-equilibrium concentration can be written in terms of equilibrium concentrations and the transport coefficients as:

$$c^{\beta}_{min,\kappa} = \frac{\left(w \cdot c^{\beta}_{min} + \left({D^{\beta}_{Li}}/{\kappa}\right) \cdot c^{\beta}\right)}{\left(w + {D^{\beta}_{Li}}/{\kappa}\right)} \qquad 1\text{-}28$$

Substituting the value of $c^{\beta}_{min,\kappa}$ from Equation 1-28 and j from Equation 1-27 to Equation 1-24 and integrating within the limits of w_0 to w for width and 0 to t for time, yields the final Equation 1-29 to model the growth of the β-phase in the presence of a interfacial barrier.

$$t = \frac{c^{\beta} - c^{\sigma}_{max}}{\kappa \cdot (c^{\beta} - c^{\beta}_{min})}(w - w_0) + \frac{c^{\beta}_{min} - c^{\sigma}_{max}}{2D^{\beta}_{Li} \cdot (c^{\beta} - c^{\beta}_{min})}(w^2 - {w_0}^2) \qquad 1\text{-}29$$

If the barrier is neglected, $\kappa \to \infty$, (the first term on the right-hand side) in the above equation, then a normal parabolic growth relation can be obtained which was already discussed in Figure 1-4 of the previous sub-section.

While the above growth relation is derived for the phase boundary, a similar kinetic barrier can be expected wherever a rearrangement of atoms at an interface is required for the phase propagation. For instance, at the Butler-Volmer interface in a battery electrode[53].

1.3.3 Migration in ionic compounds

While the physics of solid-state diffusion is important to understand the migration of lithium inside of an electrode, additional factors should also be considered which play a crucial role in governing the kinetics of lithium migration in a full battery. For instance, the migration of lithium from a liquid electrolyte to the solid electrode; migration of electrons from the current collector towards the electrode/electrolyte interface so as to neutralize the charged lithium-ion in the electrolyte. Additionally, there are effects stemming from the charge accumulation at the different interfaces which could provide additional electronic resistances[54].

The charge transfer kinetics or current at the electrolyte/solid electrode are generally described by the Butler-Volmer equation[55–57]:

$$I = I_0 \cdot (e^{-\frac{\alpha \cdot z \cdot q_e \cdot \eta_{eff}}{k_b \cdot T}} - e^{\frac{(1-\alpha) \cdot z \cdot q_e \cdot \eta_{eff}}{k_b \cdot T}}) \qquad 1\text{-}30$$

where I_0 is the exchange current; α is the charge transfer coefficient; z is the valence of the mobile ion, same as in Equation 1-2; q_e is the elementary charge; η_{eff} is the effective over potential which drives the reaction forward. The effective over-potential is defined as[57]:

$$\eta_{eff} = \eta + IR_{film} \qquad 1\text{-}31$$

where R_{film} is the film resistance and η is further defined as[57]:

$$\eta = \Delta\phi - \Delta\phi^{eq} \qquad 1\text{-}32$$

where $\Delta\phi$ is the potential difference between the solid, electron-conducting electrode and the electrolyte; $\Delta\phi^{eq}$ is the equilibrium reaction voltage, determined by the Nernst Equation as[57]:

$$\Delta\phi^{eq} = -E_0 + \frac{k_b \cdot T}{q_e} \ln \frac{a_{lyte}}{a_{cell}} \qquad 1\text{-}33$$

where a_{lyte} and $a_{electrode}$ are the activities of lithium in the liquid electrolyte and the electrode, E_0 is the standard half-cell potential given by the difference between the electrochemical potential difference between the anode and the cathode over the elementary charge. Considering equations from 1-30 to 1-33, Fick's laws and by defining the electrochemical potential of the electrode, a kinetic model describing a full battery can be made as has been done by Smith and Bazant[58].

In the above equations, from 1-31 to 1-33, the effect of electron conduction is only considered in the definition of η_{eff} in Equation 1-31. But, if the material is a mixed electronic and ionic conductor or is having less electronic conductivity, the electronic conduction not only affects the over-potential at the surface of the electrode but also the charge neutralization at the surface. In such case, merely Fick's law will not govern the ion insertion/migration but also Ohm's law has to be considered, which is combined together as[59,60]:

$$i_{ion} = -z \cdot q_e \cdot D_{ieon}^{chem} \cdot \nabla c_{ion} + t_{ion} \cdot i_{tot} \qquad 1\text{-}34a$$

$$i_{eon} = q_e \cdot D_{ieon}^{chem} \cdot \nabla c_{eon} + t_{eon} \cdot i_{tot} \qquad 1\text{-}34b$$

where i_{ion} and i_{eon} are the current density, t_{ion} and t_{eon} are the transference number, of the ionic and electronic species; D_{ieon}^{chem} is the common chemical diffusion taking into consideration the ionic and electronic diffusion and conductivity and is given as[59,60] (assuming no trapping sites for any species):

$$D_{ieon}^{chem} = t_{eon} \cdot D_{ion} + t_{ion} \cdot D_{eon} \qquad 1\text{-}35$$

where D_{ion} and D_{eon} are individual diffusivities of ions and electrons, respectively.

Taking the gradient of Equation 1-34 and applying mass conservation in 1-D across an infinitesimal length scale, an Equation similar to Fick's second law is obtained as:

$$\frac{\partial c}{\partial t} = -\frac{1}{z q_e}(\nabla \cdot i_{ion}) \qquad 1\text{-}36$$

Only in the above Equation 1-34 the transference number (representing the ratio of ionic to electronic conductivity) is considered in addition which will also control the mass flux of the inserted species.

Other regions that have been known to affect the electrochemical potential are the interfaces, either between the surface of the electrode and the liquid electrolyte, or electrode and current collector, etc. The variation of the electrochemical potential in the different interfaces of the battery are introduced very conveniently in a review article by Usiskin and Maier.[54]

It should be pointed out here that the equations in this sub-section, i.e. section 1.3.3, have not been used in this work to evaluate the diffusion coefficient and have been presented for the completeness of this thesis. This is because: (i) the sample geometry (see chapter 5) allowed us to probe the migration of already neutralized lithium ions inside of the electrode, hence, the lithium-ion migration is only governed by the variation in chemical potential and not by the electronic

conductivity; and (ii) generally, an electrode material has a significantly large electronic transference number such that the second term in Equation 1-35 can be neglected i.e., the electronic conductivity is not limiting the insertion of lithium ions.

1.4 Motivation

In contrast to microelectronics, for which the scale of integration has reached an impressive maturity, the integration in optical data processing appears still quite limited. This is primarily due to the fact that a convenient optical actuator, analogous to a field-effect transistor, does not exist on the optical side. Furthermore, the required geometric accuracy to properly control wave interference is much more demanding than for electrical routing. To the present day, micromechanical mirrors and/or thermo-refractive elements are primarily utilized to control optical signals. However, these functional elements come with a serious limitation in packaging density. If many thermo-refractive elements are densely packed, overheating or crosstalk between different subunits will become unavoidable.

The aforementioned characteristics of electrochromic material provide an innovative possibility of switching or tailoring optical signals. This can be realized by cladding a silicon waveguide with a suitable EC material and controlling the input voltage to control the lithium concentration in the cladding. Any change in lithium concentration in an EC material will consequently change its optical constants. This change in optical constant will in turn modulate the phase of EM wave traversing through the waveguide by means of evanescent-wave coupling.

Chapters 3 and **4** quantify the optical properties of two established battery electrodes namely $LiMn_2O_4$ and $Li_4Ti_5O_{12}$, respectively, and lay the foundation towards the on-chips application of switching optical signals. As the starting step, these chapters discuss the change in the refractive index of the material and the corresponding change in the band structure with lithium insertion or removal.

Additionally, in the case of $Li_4Ti_5O_{12}$, the change in optical behavior upon lithium insertion is linked to the microstructure since it undergoes a phase transformation upon lithium insertion. The importance of grain boundaries for phase transformation is hence, elucidated.

Another area where the EC effect can be exploited is to study the migration of lithium atoms. Although the theoretical understanding of lithium insertion/ migration in an electrode through the electrolyte has reached significant maturity,[57,61–63] the knowledge about the kinetics of lithium migration in particular phases, and through relevant phase-boundaries is quite often, surprisingly, missing. While for metals and alloys, the kinetics of long-range transport can be accurately measured using sensitive techniques such as tracer diffusion experiments, secondary ion mass spectroscopy (SIMS), Auger electron spectroscopy (AES), or other methods of microscopic chemical analysis[64], with battery materials similar investigations are hindered by the high mobility of lithium at room temperature. For lithium-ion batteries, the most widely used methods to study kinetics are electrochemical impedance spectroscopy (EIS), cyclic voltammetry, potentiostatic or galvanostatic intermittent transition technique (PITT, GITT). Some studies with SIMS[65–67] and nuclear magnetic resonance (NMR)[40,68,69] have also been reported. However, in the case of SIMS, the measurements can only be taken ex-situ as it is a destructive technique. Hence, certain inaccuracy must usually be accepted due to air exposure and lithium migration during sample preparation. NMR delivers information about jumping rates and intrinsic diffusion which, however, could significantly differ from the chemical diffusion that controls the lithium migration in a concentration/chemical potential gradient under the operational conditions. The electrochemical methods do provide the kinetic information in terms of diffusion coefficients, but the specific effect of kinetic barriers at the inner boundaries, for instance in a multi-phase system, is very difficult to extract and is still under debate.

Due to the above-mentioned challenges in probing and quantifying the kinetics of lithium migration, a new methodology is developed in **Chapter 5** which tackles the problem. It uses optical microscopy for the direct visualization of lithium migration by exploiting the electrochromic function of the material. Using this innovative and effective technique a detailed kinetic description of lithium migration and the consequent phase propagation inside a battery electrode namely $Li_4Ti_5O_{12}$ is provided.

2 Experimental Methods

This chapter describes the working principle of the established techniques that have been used throughout this work. Individual parameters and the development of specific analytical methodologies will be explained in the respective chapters. This work primarily deals with thin-film battery electrodes since they provide model geometries for probing the fundamental properties of the materials. The schematic of such an electrode is given in Figure 2-1 (b).

Prior to any characterization, the sample needs to be prepared. Radio-frequency (r.f.) ion beam sputtering is used for thin-film deposition. Oxidized silicon wafers with <100> orientation were used as substrates. Firstly, a platinum layer is deposited. This layer acts as a current collector and a reflective mirror for the electrochemical characterization and reflective electrochromic characterization, respectively. Once the thin films are prepared, an appropriate annealing treatment is performed. Finally, essential structural, electrochemical, and electrochromic characterizations are commenced. For the kinetic evaluation, an additional step of e-beam lithography is needed as described in Chapter 5.

2.1 Thin-film deposition

The schematics of the custom-built r.f. ion-beam deposition system, used in this work, is shown in Figure 2-1. It is a type of physical vapor deposition, in which energetic argon atoms knock the atoms of the target, which are then deposited on the substrate to nucleate the new solid phase. The base pressure of the ultra-high vacuum (UHV) chamber is ca. 1×10^{-7} mbar. The argon plasma is generated in a small ceramic cavity of 4 cm diameter (inside the UHV chamber). The ceramic cavity is surrounded by an inductive coil. This inductive coil is powered by an r.f. source (Roth & Rau AG) operating at 13.56 Mhz and delivering a power of 130 W-150 W. The device can be thought of as a transformer, where the inductive coil acts as the primary coil and the discharge plasma acts as a secondary coil. Due to the

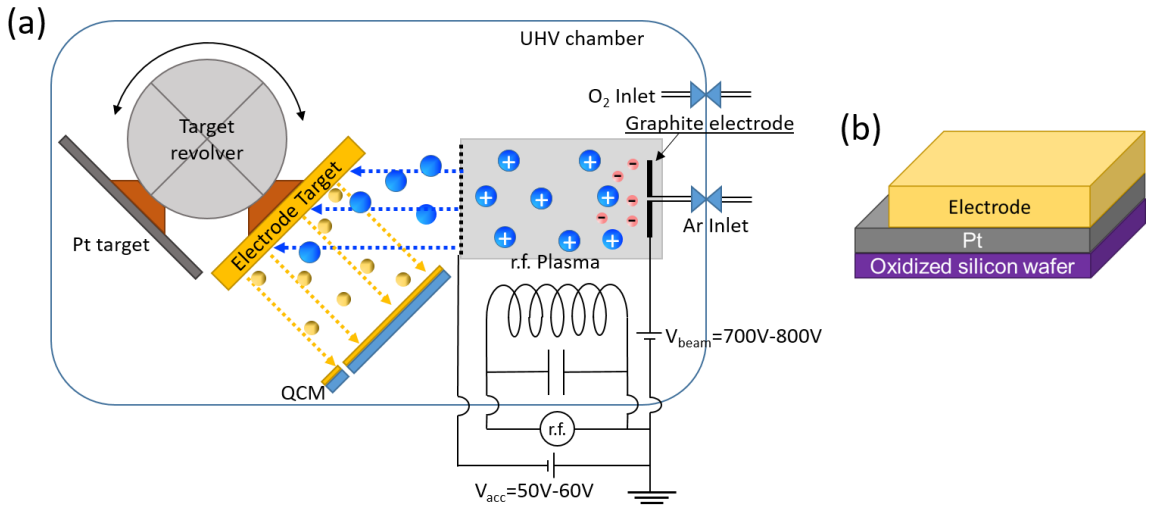

Figure 2-1: *Schematics of (a) the r.f.-ion-beam sputtering, and (b) the sputter deposited sample.*

high frequency of the r.f. source, the argon atoms in the ceramic cavity gets ionized. To initiate the plasma generation, the argon gas is purged into the cavity. As soon as a single argon ion is generated, due to high pressure during purging, an avalanche of atomic collisions creates a stabilized plasma. The chamber pressure during the stable sputtering is ca. $2\text{-}4\times10^{-4}$ mbar. The charged plasma is accelerated towards the target by applying a potential of 700 V to 800 V, generating a beam of ions. An additional potential of ca. 50-60 V is applied at the semi-permeable grids to focus the beam towards the target. A beamswitch switches the beam and accelerator potential synchronously, i.e. changes the polarity, so as to release the electrons from the graphite electrode placed at the rear end of the ceramic cavity, to neutralize the beam. The switching frequency is ca. 11.6 kHz operating the reverse polarity for roughly 20% of the beamtime.

Additionally, for the oxide layer deposition, a partial oxygen atmosphere, along with argon plasma, is maintained in the sputter chamber. This is done to achieve correct stoichiometry of atoms in the deposited layer. For sputtering multi-layers, at a time four target materials can be installed in the chamber. An oscillating quartz balance is used to record the thickness of the deposited layer during sputtering.

2.2 Structural characterization

Once the sample is sputtered, the structural characterization is undertaken to determine appropriate sputtering and annealing conditions. The following techniques are used to determine the crystal structure and the morphology of the sample.

2.2.1 X-ray diffraction

X-rays are produced by the rapid deceleration of charged particles. They are high-energy electromagnetic radiation having wavelengths ranging from a few angstroms to a few nanometers. As the wavelength of the X-rays is in the same order as the lattice spacing of a crystal, they are diffracted by the periodic arrangement of the crystal lattices. The spatial relation between the diffracted beam, the incident beam, and the surface of the sample unravels the structure of the crystal. The obtained diffraction pattern can be elucidated by using Bragg's law i.e. when the X-rays with wavelength, λ are incident on parallel atomic planes (separated by a distance, d) at an angle θ (between the X-rays and the plane), they constructively interfere with each other if:

$$2 \cdot d \cdot \sin(\theta) = y \cdot \lambda \qquad 2\text{-}1$$

Where y is called the order of reflection, it can take any integer value, provided the value of $\sin(\theta)$ does not exceed 1. It represents the number of wavelengths in the path difference between the rays scattered by the adjacent planes. While the inter-planar spacing determines the diffraction angle, the position and the species of the atoms in a lattice determines the intensity of the diffracted rays (for a powder diffraction pattern).

In this work, X-ray diffraction (XRD) is used to determine the crystal structure of the deposited layer, before and after appropriate heat treatment. Two different diffractometers were used throughout this work, a Siemens D5000 using θ-2θ

geometry and a Bruker D8 general area detection diffraction system using a detector scan at an incidence angle of 10°.

2.2.2 Electron microscopy

Louis de Broglie gave the idea of matter waves in his doctoral thesis in 1924[70], which also revealed the wave nature of electrons. This led to the idea that images could also be generated with the help of an accelerated beam of electrons. The main reason for using electrons was to increase the resolution of the microscope. The foundation for the development of an electron microscope was led by the innovation of electron optics by H. Busch (1926).[71] Subsequently, two different geometries were considered for positioning the sample which led to the development of a transmission electron microscope (TEM) and a scanning electron microscope (SEM).

Transmission electron microscopy

In a transmission electron microscopy, an assembly of electromagnetic lenses (condenser lenses) focuses a beam of electrons to pass through the sample and the transmitted scattered electrons are focused onto a photographic plate or a camera with the help of another set of electromagnetic lenses (objective lens and projector lenses). In this work, a Philips CM200-FEG instrument was used for TEM analysis. As the electron beam has to pass through the sample, careful sample preparation is needed. For this, a dual-beam equipment (FEI Scios Dual-Beam microscope), with an ion-beam and an electron beam was used to make electron transparent foils from the prepared thin-films.[72] The TEM is used in this work to analyze: (i) the crystal structure using selected area electron diffraction (SAED) of the deposited and annealed films; and (ii) the microstructure and film thickness of the samples.

Scanning electron microscopy

In this type of instrument, the sample need not be electron transparent and the objective lens is placed before the sample. The incoming electrons strike the sample as a sharp probe and the resultant scattered electrons are collected by a

detector. The beam of electrons scans the surface of the sample and the collected intensity, from the scattered electrons, from each pixel is converted into a gray-scale image. In this work, a FEI Scios Dual-Beam instrument was used as SEM mainly for the lithography process (described in chapter 5), while a FEI Quanta was used for inspecting the morphology of the sample coated using the aforementioned lithography process.

2.3 Electrochemical characterization

To study the intercalation kinetics and mechanism of lithium insertion in a battery electrode, various electrochemical characterization methods have been developed. These are initiated by devices known as potentiostats and/or galvanostats. Throughout this study, two different potentiostats have been used namely Bio-logic VSP 300 and Gamry Interface 1000. The different electrochemical methods used in this work are explained below.

2.3.1 Cyclic voltammetry (CV)

In this method, an increasing voltage is applied through the electrodes and the resulting current is measured, following a decrease of the voltage in a reversed manner to complete a cycle. Generally, the voltage is varied linearly and the

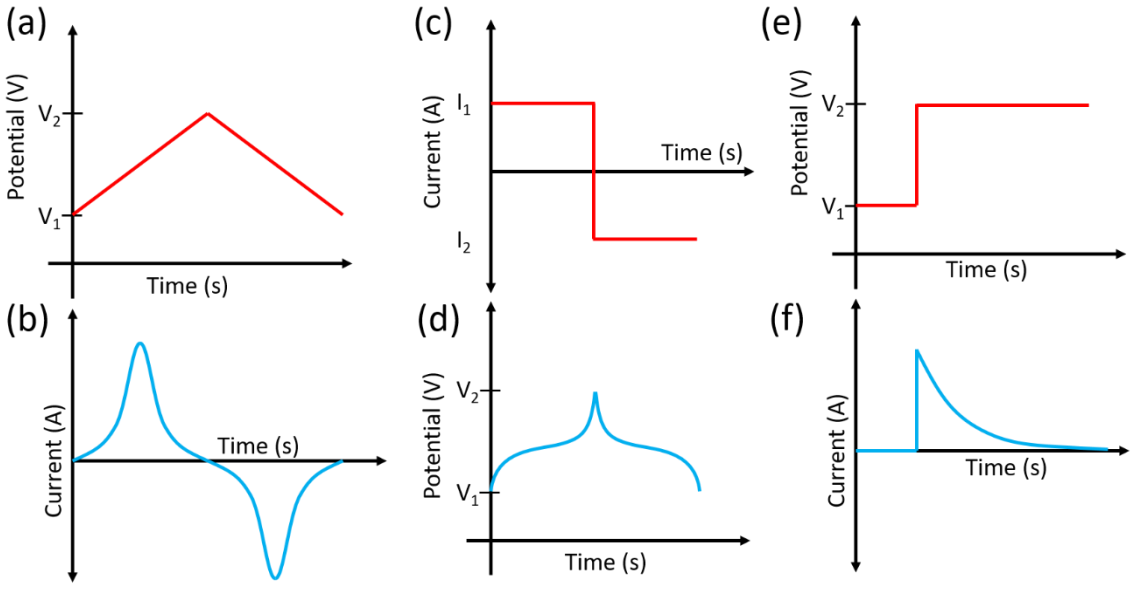

***Figure 2-2**: Input in CV, CP and CA are shown in (a), (c) and (e), respectively. The respective output of CV, CP and CA are shown in (b), (d) and (f).*

resulting variation in the current is recorded, see Figure 2-2 (a) and (b). The amount of current signifies the flux of ions intercalated or de-intercalated at a particular voltage.

2.3.2 Chronopotentiometry (CP)

A constant current is applied through the electrodes and the resulting voltage variation is measured, see Figure 2-2 (c) and (d). The technique is useful in estimating the capacity of an electrode. Furthermore, the slope of the voltage vs time/capacity can give an impression of the mechanism of the ion insertion, be it via a single-phase process (a slightly sloped profile) or a phase transformation process (a flat plateau shaped profile).

2.3.3 Chronoamperometry (CA)

This technique is mostly used to determine the kinetics of ion insertion. In this method, a constant voltage is maintained versus a reference electrode and the resulting current is measured, see Figure 2-2 (e) and (f). In this work, the technique is used to obtain a fixed charge state by maintaining a particular voltage for a long duration of time.

2.4 Electrochromic characterization

As mentioned before, EC material changes color upon ion insertion/ removal. This change can be quantified either by using a reflectance spectrum or a transmission spectrum. These spectra can be modeled by using Fresnel's coefficients and by defining the refractive indices of the materials (as mentioned in Chapter 1). To simplify a physical model describing the experiment, in this work, the active electrodes were deposited on top of a platinum layer (≈100nm) which acts as an almost perfect mirror for EC characterization. Therefore, only the knowledge of the reflectance through the electrode layer is sufficient to determine the optical constants. Furthermore, Fresnel's coefficients depend on the refractive indices of the materials forming the interface. Therefore, an ex-situ methodology is used for quantitative modeling as the reflectance can be measured in an air/argon

atmosphere, for which the refractive indices are known. The qualitative reversibility of the optical change is also important which is studied by using in-situ electrochromic characterization. The description and the implementation of the respective methods are described in detail in Chapter 3 and Chapter 4. Additionally, a method exploiting the electrochromic behavior of material to study the diffusion of lithium ions in the thin-film battery electrode is developed in this work and is described in chapter 5.

3 Optical Change in Thin-Film $Li_xMn_2O_4$ Electrode upon Li-ion De-/Intercalation

The spinel structured lithium manganese oxide ($LiMn_2O_4$ or LMO) is a thoroughly researched cathode material for lithium-ion batteries. It has been under investigation for more than three decades. A unit cell of LMO consists of 8 formula units where oxygen atoms are occupying the 32e position, manganese is occupying the 16d position (or octahedral sites) and lithium is occupying predominantly the 8a sites (or tetrahedral sites) as shown in Figure 3-1.[73] The migration of lithium atoms between two 8a sites is mediated by the neighboring empty 16c voids[74] (light blue octahedra in Figure 3-1).

Numerous studies have characterized the material for its functional properties such as electronic conductivity, lattice vibration, etc.[75–82]. However, only in 2016, a characteristic change in color due to lithium intercalation was reported in LMO.[83] This would indicate a change in its optical properties during lithiation. A quantification in terms of optical constants and tailoring these constants via dis/charging has been studied in the paper by the author of this work[E1]. The article

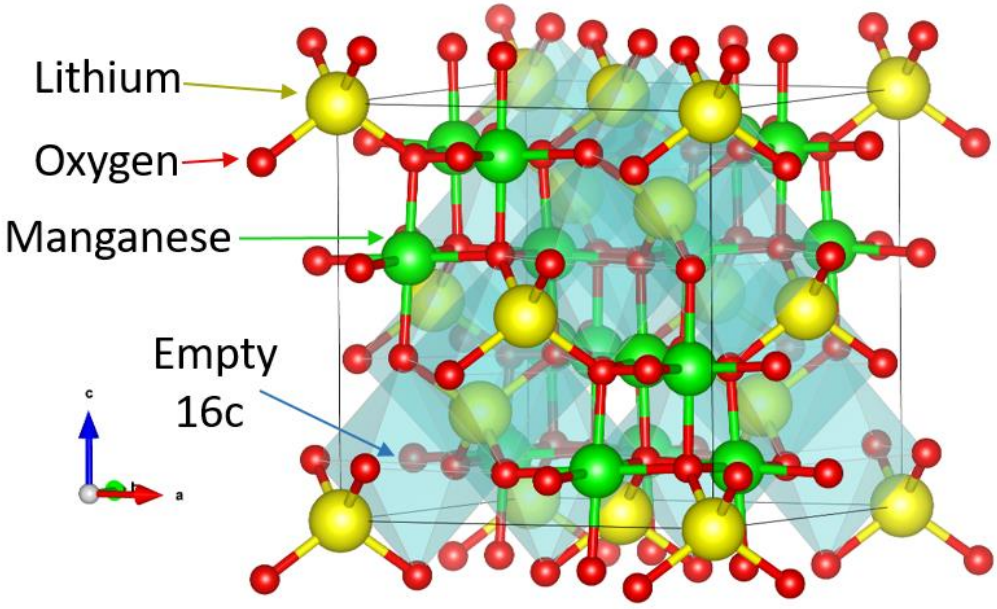

***Figure 3-1**: Crystal structure of $LiMn_2O_4$.*

is one of the published works towards the completion of this thesis. The present chapter describes the findings discussed in the article. This includes the quantification of the optical constants (the complex refractive index, CRI) and its change during intercalation by varying the lithium content of $Li_xMn_2O_4$ from $x = 0$ to $x = 1$. Furthermore, the change in optical constants is linked to the band structure of the material gathered from various sources.[73,77,81,85–87] Also, an innovative method of recording the reflectance spectrum in-situ during the electrochemical reaction is demonstrated (Figure 3-2(c)) that provides an additional time resolution to the spectrometry.

3.1 Experimental realization

3.1.1 Thin-film preparation

The LMO layer has been deposited using r.f.-ion beam sputtering. The required target was prepared from cold-pressed powder (Sigma-Aldrich CAS no. 12057-17-9), followed by sintering at 900°C for 10 h.[88] For structural stability, the sintered powdered cake was glued onto a metal disc of 80 mm diameter using a two-component conductive epoxy glue. First, a layer of platinum was sputtered with a pure argon plasma (working pressure 1×10^{-4} mbar). Subsequently, LMO was sputtered using a mixture of argon: oxygen (7:3, total pressure 1.3×10^{-4} mbar) as a reactive gas. These parameters have been reported to obtain optimum electrochemical properties for LMO.[89] The Ar plasma was generated with an r.f. power of 140 W, and it was accelerated with a voltage of 800 V. The resulting beam was focused with a voltage of 50V. This resulted in a sputter rate of 0.6 nm min^{-1} for LMO and 2.5 nm min^{-1} for Platinum. The thickness of LMO is kept above 300 nm. The deposited bilayer is then annealed at 750°C for 1 h in air and is used subsequently for electrochemical and electrochromic characterization.

The crystallinity of the as-deposited and annealed film is measured by X-ray diffractometry (Siemens D5000) using Cu Kα radiation. The microstructure was characterized by transmission electron microscopy (Philips CM200-FEG).

3.1.2 Electrochemical characterization

The Cyclic Voltammetry (CV) and Chronopotentiometry (CP) were controlled by a Bio-Logic VSP 300 potentiostat. The electrochemical cell had a three-electrode configuration, as sketched in Figure 3-2(a). The LMO/Pt bilayer serves as the working electrode (WE) and two lithium foils as the counter (CE) and reference (RE) electrode. Hence, all the potentials reported herein, are measured with respect to Li/Li^+. The liquid electrolyte used in the electrochemical cell constitutes 1M $LiClO_4$ in a 1:1 mixture of ethylene carbonate and dimethyl carbonate. All the electrochemical cells were assembled in an argon-filled glove-box (MBraun Unilab).

The CV was performed in a potential window of 3.4 V to 4.3 V at a scan rate of $\nu = 0.1$ mV s^{-1}. The CP was executed with a constant current of ±3.6 µA applied within the same potential window. The specific capacity of the layer has been determined from the CP measurement for a particular layer thickness. The corresponding mass of the film was calculated by the known reaction volume i.e., multiplying the area of the film dipped in the electrolyte with the thickness, evaluated from the TEM micrograph, and taking into account the density of the film (4.1 g cm^{-3} at 25°C) as specified by the manufacturer (Sigma-Aldrich).

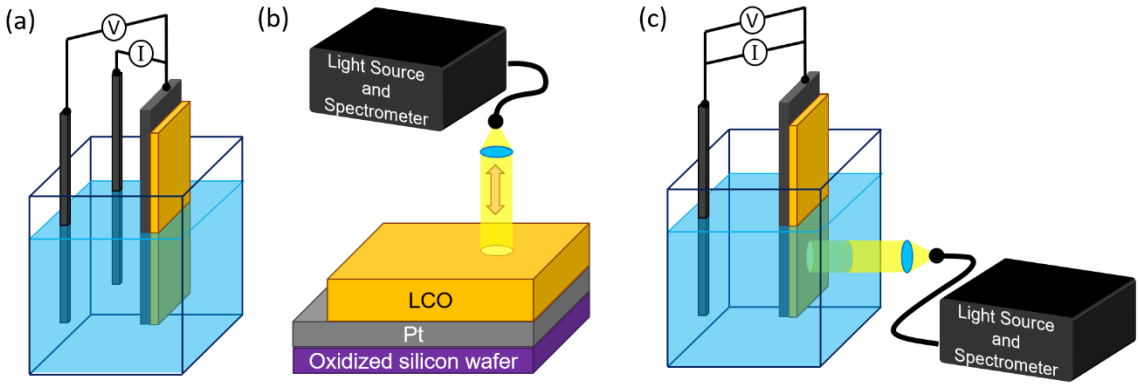

***Figure 3-2**: (a) A three-electrode set-up used for electrochemical characterization and to establish a stable, well-defined charge state for ex-situ reflectance measurement; (b) Schematics of ex-situ reflectance measurement; (c) A two-electrode set-up to measure in-situ reflectance during electrochemical dis/charging.*

3.1.3 Electrochromic characterization

The electrochromic behavior was studied via ex-situ and in-situ reflectance spectroscopy.

Ex-situ reflectance spectroscopy

In the ex-situ reflectance spectroscopy, the optical measurements are performed at stable charge states of x = 0, 0.2, 0.4, 0.6, 0.8, and 1 in $Li_xMn_2O_4$. To achieve this, firstly the sample is de/-intercalated to the desired charge state using CP. Subsequently, it is held at this potential using CA until the current drops below 0.2 µA (roughly 6 h equilibration period). After reaching the equilibrium condition, the sample is removed from the electrochemical cell and is cleaned with acetone followed by ethanol. Next, the reflectance spectroscopy is performed at normal incidence (incident light is perpendicular to the sample) in an argon atmosphere as schematically depicted in Figure 3-2(b). A BW-Tek BPS101 tungsten halogen lamp was used as a light source. This source was connected to the 'light source leg' of the Fiber Optic Reflection Probe Bundles (ThorLabs RP 29, a type of bifurcated fiber cable) on one end. The other end i.e., the 'sample leg' illuminates the sample. The resulting reflected beam is collected by another fiber at the same 'sample leg' end of the bundle and is directed to a BW-Tek Exemplar spectrometer.

In-situ reflectance spectroscopy

The in-situ recording of the optical spectrum along with the electrochemical insertion of ions is executed in a specially designed electrochemical cell. It is constructed in a quartz cuvette with a squared cross-section offering flat transparent surfaces of sufficient optical quality. Owing to the restricted space, a two-electrode configuration has been used in which LMO/Pt serves as the WE and a single lithium foil as both the CE and the RE as shown in Figure 3-2(c). The setup is operated inside a glove box under Ar protection. (Electrochemical measurement was controlled with a Gamry Interface 1000 potentiostat). The optical set-up is the same as that used for ex-situ measurements except for the fact that light is made

incident onto the quartz cuvette (in which the WE is aligned perpendicular to the incident beam, by maximizing the intensity of the reflected light). The spectra are recorded every second during a CV measurement with a scanning rate of $v = 0.1\ mV\ s^{-1}$. A point to note, in this work the optical constants are evaluated using ex-situ methodology, as in the case of in-situ characterization light has to pass through an additional layer of the electrolyte, for which the refractive index and absorption factor are unknown. Hence, reasonably assuming that the optical properties of the electrolyte are not changing over cycling (as the concentration is not changing) the in-situ data can be used to check for the qualitative reversibility of the optical behavior and to probe the dynamic change in optical response upon charging/discharging.

3.2 Results

3.2.1 Structural characterization

Figure 3-3(a) shows the XRD spectra of the representative samples of LMO in the as-deposited and annealed states. In the as-deposited condition, no characteristic diffraction peaks of LMO are observed (bottom curve of Figure 3-3(a)). Only a small bump, at 61.98° is observable (marked with *). It could be due to the {440} reflection from the LMO crystal structure. This reflection is very broad and shifted in comparison to the {440} reflection reported in the work of Wickham et al.[90] (JCP2 database) that identifies the correct position at 63.78°. The shape and the shift of the reflection spectra suggests that the LMO layer is nano-crystalline and stressed. This is usually the case for sputter-deposited layers. The nano-crystalline structure is confirmed by the bright-field TEM of the as-deposited LMO, as shown in Figure 3-3(b). The micrograph also exhibits a columnar microstructure of the LMO layer, comprising grains that are elongated in the growth direction. The inset of Figure 3-3(b) and (c) shows the corresponding SAED pattern, revealing a ring pattern consistent with the expected Bragg angles of the LMO spinel structure as shown in yellow semi-circles[90]. Over-emphasized bright spots of the {440} planes are observed which are aligned in the growth direction. This clearly indicates a <440>

fiber texture which is confirmed by a dark field image obtained using a (440) reflection in Figure 3-3(c). A major part of the thin film appears bright in this dark field image, indicating that this grain orientation is the dominant one.

After annealing, a coarser crystalline structure of the LMO layer is obtained as shown in the XRD spectra i.e., the top curve of Figure 3-3(a). Reflections at 18.75°,

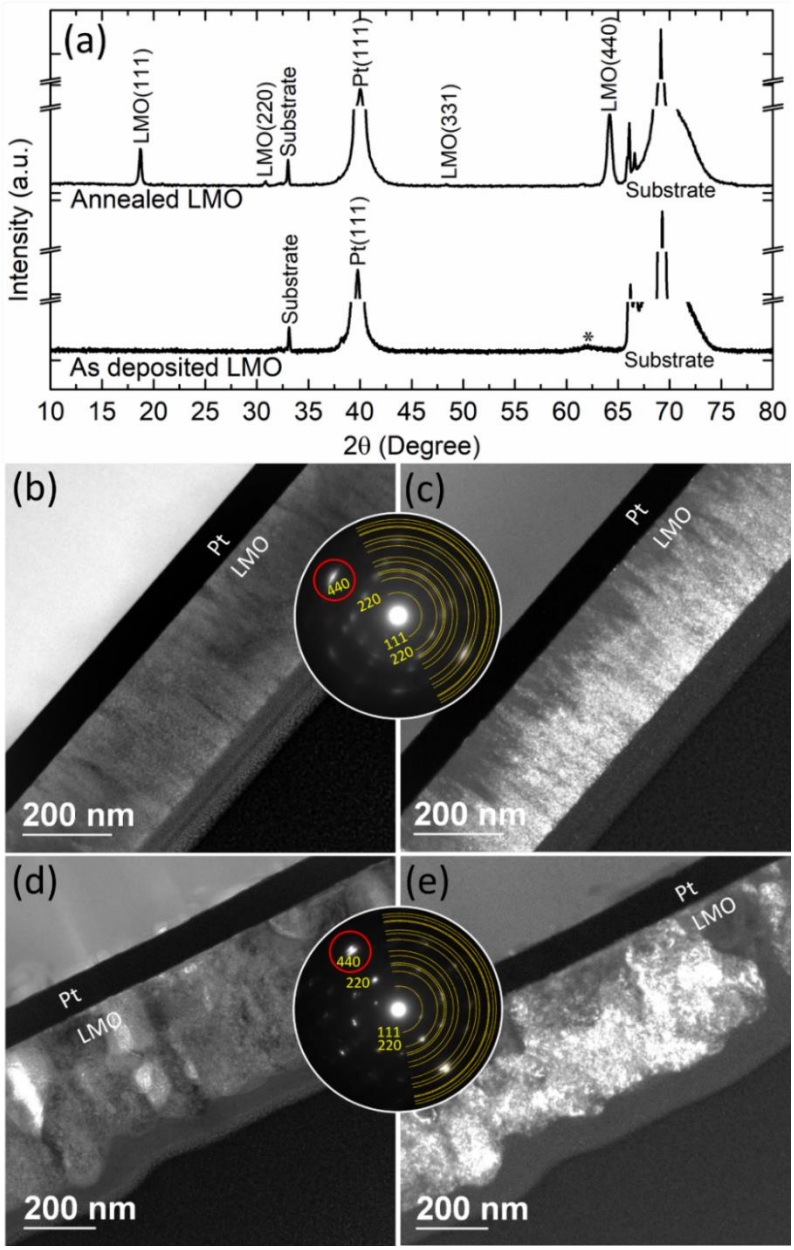

***Figure 3-3**: (a) X-ray diffractogram (using Cu Kα radiation) of the as deposited (bottom graph) and annealed sample (top graph); Transmission electron microscopy (b to e): as-deposited state: (b) bright field, (c) dark field image; Annealed state: (d) bright-field and (e) dark-field. Both dark-field images are generated using the 440 reflection marked with a red circle in the shared inset figure showing the corresponding SAED pattern.*[E1]

30.75°, 48.3°, 64° correspond to {111}, {220}, {331} and {440} lattice planes (Wickham et al.)[90]. This crystal structure is confirmed on a microscopic scale by the SAED pattern, in the inset of Figure 3-3(d) and (e). The bright-field micrograph now shows more equiaxed grains. But the SAED pattern, shown in the inset, and the associated dark field image, shown in Figure 3-3(e), still demonstrate a <440> fiber texture, which appears even more pronounced than in the as-prepared state. This strong texture also explains the unusual intensity ratios among the X-ray peaks. The ratio of the X-ray intensity resulting from the parallel lattice planes, {440} and {220} is 16.1. This is in good agreement with the literature value of 16 for a random orientation distribution (Wickham et al.[90]). In contrast, the ratios of the intensities stemming from {111} reflection to the non-parallel {220} and {440} planes amount to only 0.12 and 0.5, respectively, while they are expected to be 6.25 and 100 (Wickham et al.[90]). Such large deviations confirm that the sputter-deposited layer has indeed a very strong <440> fiber texture.

3.2.2 Electrochemical characterization

The electrochemical response of the annealed films in a CV (main diagram) and a CP (inset) measurement is shown in Figure 3-4. De/Intercalation of LMO appears in two distinct steps.[91] The two sharp peaks in the CV and the comparable two plateaus in the CP are at 4.05 V and 4.15 V, these belong to the partial reactions as stated in Equation 3-1 and 3-2:

$$\mathrm{LiMn_2O_4} \rightarrow \mathrm{Li_{0.5}Mn_2O_4} + \frac{1}{2}\mathrm{Li^+} + \frac{1}{2}\mathrm{e^-} \qquad 3\text{-}1$$

$$\mathrm{Li_{0.5}Mn_2O_4} \rightarrow \lambda\text{-}\mathrm{MnO_2} + \frac{1}{2}\mathrm{Li^+} + \frac{1}{2}\mathrm{e^-} \qquad 3\text{-}2$$

Only half of the available sites are occupied in the first step of intercalation at 4.05 V due to a repulsive Li-Li interaction. The remaining half follows at 4.15 V.[92] The capacity of LMO, as determined by the CP measurement, is shown in the inset of Figure 3-4. It corresponds to 91.76 mAh g^{-1}, for the first charge cycle, when measured with a current of 5.384 µA cm^{-2} or 0.378 C charging rate. This capacity

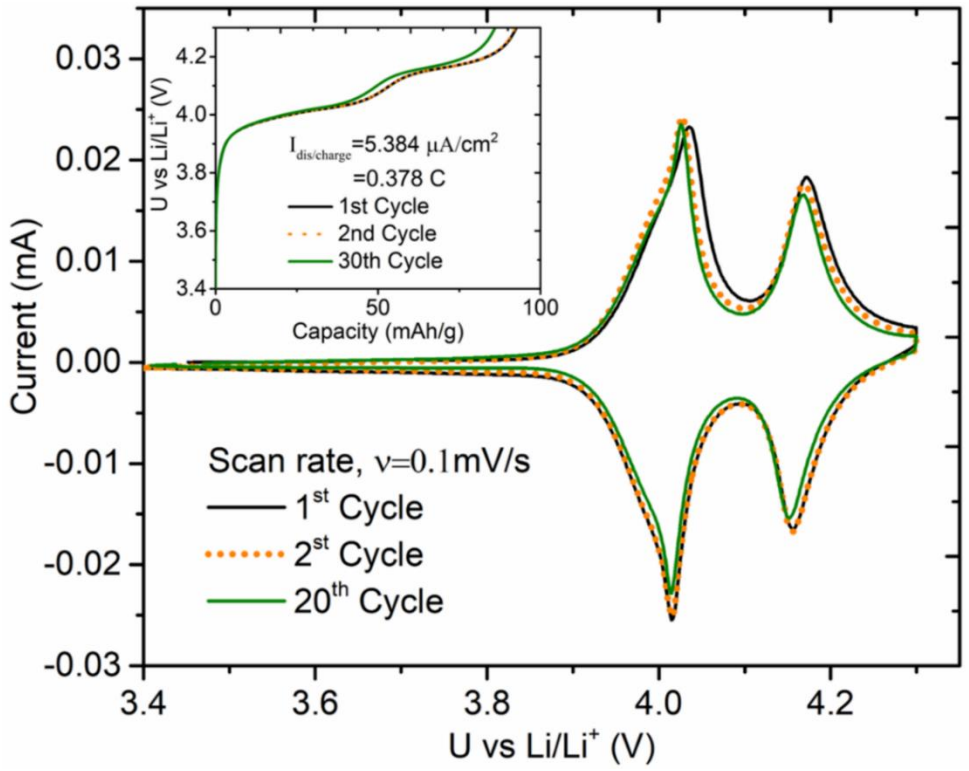

***Figure 3-4**: Cyclic Voltammetry of the annealed layer of LMO showing the reaction peaks and electrochemical reversibility for the first 20 cycles. Inset figure showing the capacity fading during the first 30 cycles as obtained from CP measurement.[E1]*

corresponds to 62% of the theoretical capacity of LMO (148 mAh g^{-1}). Since the focus of this work is on the optical response of the material, the cyclic stability is more important than the maximum capacity (capacity retention of 93% is observed between the 1st and 30th charging cycle which is sufficient to realize a reversible electrochromic function). Nonetheless, the capacity is comparable with other works on thin films of LMO. For instance, Julien et al.[93] and Xie et al.[94] reported a capacity of 78 mAh g^{-1} and 96 mAh g^{-1} for a pulse laser deposited film, and another work by Xie et al.[95] reported a capacity of 80 mAh g^{-1} for an r.f.-magnetron sputtered layer.

3.2.3 Electrochromic characterization

Figure 3-5(a) shows the spectra obtained by ex-situ reflectance spectroscopy for the $Li_xMn_2O_4$ layer (thickness of 310±5 nm) at different lithium content as stated in the figure. The fringes or maxima/minima observed are due to the optical interference between the reflected light from the two interfaces i.e. between

argon/LMO and between LMO/platinum. A shift of the maximum observed at the wavelength of 575.0 nm (for the fully lithiated condition, x = 1) to the wavelength of 671.3 nm (for fully delithiated condition, x = 0) is a clear indicator of the change in the real part of the refractive index, as the real part determines the condition of constructive/destructive interference or the phase shift (φ) of light when passing through a medium. Furthermore, it is observed that the relative reflectance of these two peaks also changes from 13.31% (for the fully lithiated state) to 19.81% (for fully delithiated state) indicating that the imaginary part (responsible for absorption) of the CRI is also varying with the lithium content.

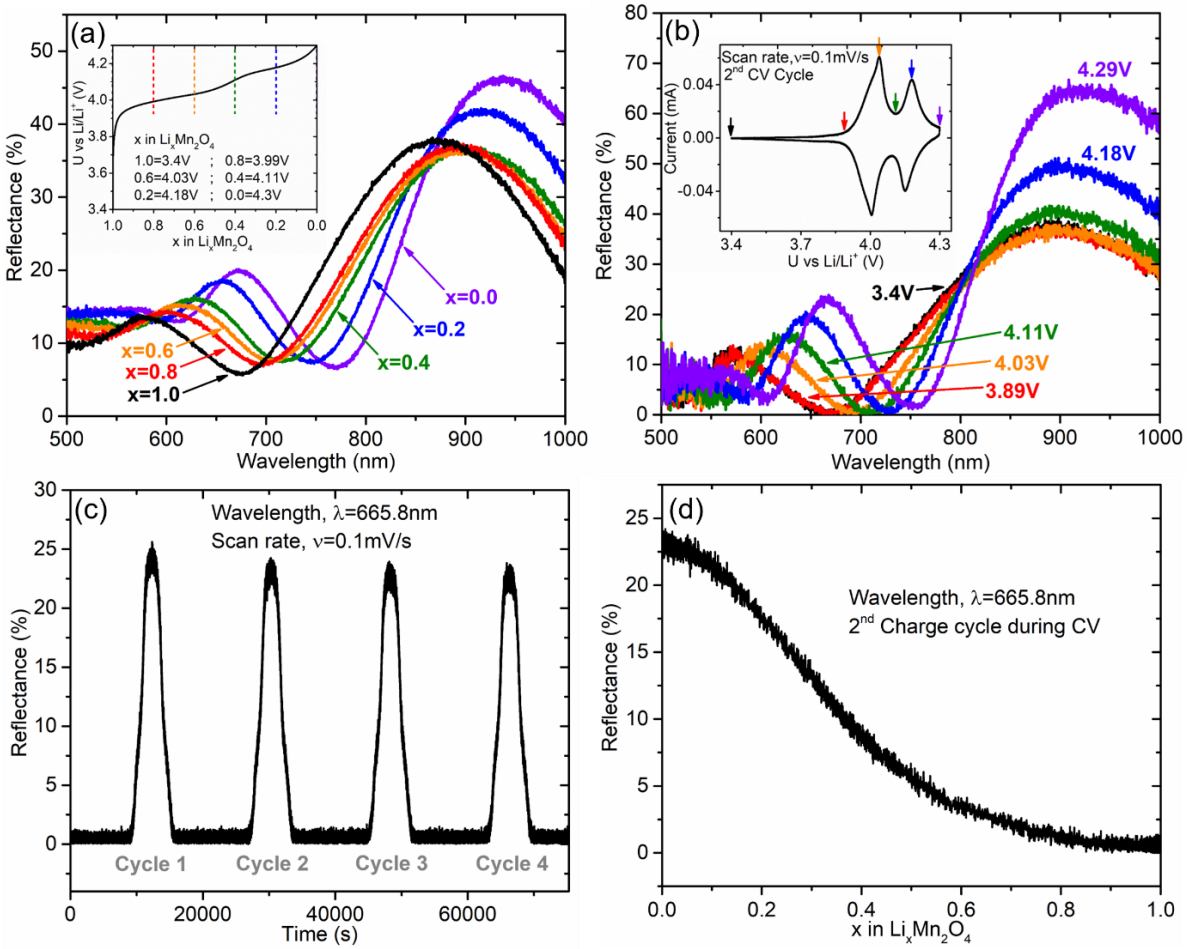

***Figure 3-5**: (a) Reflectance spectra obtained at selected stabilized charge states (depicted with dashed lines in the inset figure, showing a CP measurement of LMO); (b) Reflectance spectrum taken in-situ during cyclic voltammetry (inset figure); (c) Change in reflectance with time for a wavelength of 665.8 nm, the cell has a voltage of 3.07 V at time = 0 s (open circuit voltage) and then cycled in the voltage window between 3.4 V to 4.3 V; (d) Absolute change of reflectance with lithium content during charging.*[E1]

The reversibility of the optical response is probed with the help of in-situ reflectance spectroscopy. Several reflectance spectra, recorded during the 2nd CV cycle, are shown in Figure 3-5(b). The inset of Figure 3-5 shows the corresponding CV plot with several points marked by arrows for which the reflectance spectra are presented. The findings are similar to Figure 3-5(a), except for the fact that the minimum value is reduced. The optical reversibility during the chemical reaction is visualized by plotting the reflectance as a function of time in Figure 3-5(c) for a single wavelength of 665.8 nm. For this particular wavelength, a minimum is obtained in Figure 3-5(b) at the potential of 3.4 V (black curve hidden underneath the red curve). A point to consider here is that the measurements were initiated from a potential of 3.4 V. Hence from Figure 3-5(c), the reflectance is seen to increase during the charging (or delithiation) and to decrease during the discharging, but remain almost constant for potentials between 3.4 V and 3.8 V. This is also evident from Figure 3-5(b) in which the spectra at 3.4 V and 3.83 V are almost overlapping. This overlapping could be due to very low currents representing less mass transport in this potential range. From a careful inspection of Figure 3-5(c), it is observed that the first maximum is slightly higher than the following three, which is attributed to irreversible changes occurring predominantly in the first cycle. Furthermore, the peak intensity is slightly dropping with each cycle which can be due to the continuous capacity fading during the cyclic dis/charging, that is also visible in the CP measurement shown in the inset of Figure 3-4**.** To grasp a relation between the reflectance plots for a single wavelength and the lithium uptake/removal by the material, the current in the 2nd de-intercalation cycle of the CV is integrated over time. This integrated current is plotted together with the corresponding reflectance curve to obtain Figure 3-5(d). From the figure, it can be observed that a larger change (or larger slope) in the reflectance takes place in the second de-intercalation reaction i.e. Equation 3-2. In this reaction, the filled/removed lithium encounters no Li-Li repulsion which may shift the band-gap dominantly.

3.3 Evaluation and discussion

The bilayer system under investigation (evaluated with ex-situ measurements) has two optical interfaces: firstly, the one between the LMO (2nd medium) and the argon atmosphere (1st medium) and secondly between the LMO and the platinum current collector (3rd medium).

The equation for the reflection ($Ref(\delta,\lambda)$) is derived by the summation of the amplitude of light, reflected by the interfaces into the direction of the optical fibers as given by Equation 3-3:

$$Ref(\delta,\lambda) = \left| \left(\frac{r_{12} + r_{23} \cdot e^{-i\cdot\frac{2\pi}{\lambda}\cdot n_2^*\cdot 2\delta}}{1 + r_{12}\cdot r_{23}\cdot e^{-i\cdot\frac{2\pi}{\lambda}\cdot n_2^*\cdot 2\delta}} \right) \Big/ \mathrm{r}_{13} \right|^2 \qquad 3\text{-}3$$

where, $r_{lm} = \frac{n_m^* - n_l^*}{n_m^* + n_l^*}$ is the Fresnel's reflection coefficient between medium l and m for normal incidence; $n_l^* = n_l(\lambda) - i\cdot k_l(\lambda)$ is the CRI of medium l with $n_l(\lambda)$ and $k_l(\lambda)$ being the real and imaginary parts respectively; δ is the thickness of the thin film. The derivation of Equation 3-3 is inspired by the work of Heavens.[26] Furthermore, it is assumed that the platinum layer is opaque. This is a valid assumption since the thickness of the sputtered platinum is 100 nm. For this thickness, using the data given by Werner et al.[96] and by using Beer-Lambert's [15,16] Law, the intensity of light penetrating through the platinum layer is a mere 8.4×10^{-5} and 2.6×10^{-5} times the intensity of incident light for the wavelengths 991.8 nm and 495.9 nm, respectively. Therefore, it is safe to say that the silicon oxide layer underneath the platinum has no contribution to the measured reflectance. To determine the reflectance from the platinum surface the CRI values for platinum were adopted from the works of Werner et al.[96].

As mentioned in chapter 1, throughout this study, Clausius–Mossotti[21,22] relation, given by Equation 1-8, is used to describe the material property or CRI quantitatively. Substituting the value of the CRI from Equation 1-8 into Equation

3-3 yields the complete function used in this work for describing the reflectance spectra that are obtained with the ex-situ optical reflectometry. The initial guess of the resonant frequencies is made in accordance to the color change reported by Roeder et al.[83]. Afterward N, f_j, ω_{oj}, γ_j in Equation 1-8, are optimized using a Levenberg-Marquardt Algorithm [97–99] to obtain the best fitting.

A first attempt is made to fit the reflectance spectrum for the fully delithiated state by using three independent oscillators in Equation 1-8. The result of the best fit is depicted in Figure 3-6(a) by hollow orange triangles. The confidence of this fit (R^2) amounts to 0.97 across the entire measured wavelength range. However, it can be seen that for wavelengths less than 700 nm the model curve does not fit the experimental spectrum, as shown by the solid violet line. For further improvement, another fourth oscillator is definitely required. And indeed a remarkable improvement can be seen in Figure 3-6(a) in the fitted curve (hollow black circles) by the addition of a fourth oscillator. For this fitted curve, the confidence value even increased to 0.997 representing a nearly perfect fit on the entire wavelength range. The parameters of all the fitted curves are given in Table 3-1. These are used to evaluate the optical constants for the particular charge state as shown in Figure 3-6(b). It is noteworthy that for the wavelengths less than 565 nm, the real part of the CRI is less than unity, which is characteristic of a region of anomalous dispersion.[100] From the dispersion curve of the extinction coefficient, two strong absorption peaks are observed at 565 nm and 675 nm. These peaks correspond to a high absorption at a given resonance wavelength or frequency. This allows us to quantify, in a quantum mechanical picture, the corresponding electronic transition energy as per Equation 3-4.

$$\Delta E = \frac{h}{2\pi} \cdot \omega_{0j} = \frac{h.c}{\lambda_{0j}} \qquad 3\text{-}4$$

These resonance frequencies are also responsible for the anomalous dispersion observed in the real part of the CRI. The same steps of evaluation (with the

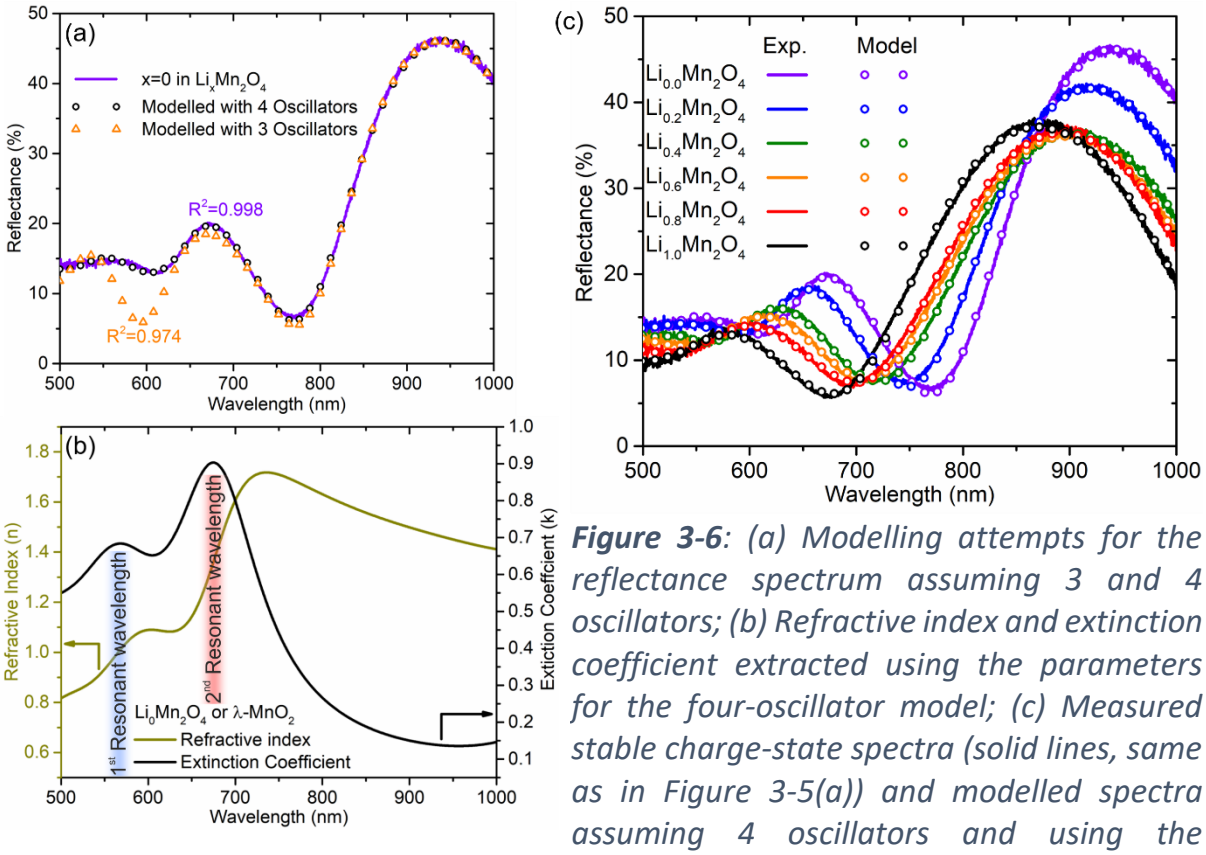

***Figure 3-6**: (a) Modelling attempts for the reflectance spectrum assuming 3 and 4 oscillators; (b) Refractive index and extinction coefficient extracted using the parameters for the four-oscillator model; (c) Measured stable charge-state spectra (solid lines, same as in Figure 3-5(a)) and modelled spectra assuming 4 oscillators and using the parameters mentioned in Table 3-1 (hollow circles).*[E1]

assumption of four relevant oscillators) are repeated for the other charging states of $x = 0.2$, 0.4, 0.6, 0.8, 1.0 in $Li_xMn_2O_4$. The model curves along with the experimental data are shown in Figure 3-6(c) and the corresponding fitting parameters are listed in Table 3-1. From the latter, the dispersion curves for the imaginary and the real part of the CRI are calculated for the studied intercalation states as shown in Figure 3-7(a) and (b). As stated previously, LMO has been recently reported to show a change in color,[83] and it is suggested here that this is due to the change in the extinction coefficient of the material. It can be seen from Figure 3-7(a), that for $x = 1$ or fully lithiated LMO, the wavelength region of least absorption (the part of the spectrum responsible for the color of the layer) is beyond the resonance wavelength of 583 nm, whereas for $x = 0$ or fully delithiated LMO, the same lies beyond 675 nm. This demonstrates that the color of the fully lithiated LMO (or $LiMn_2O_4$) will be a combination of green, yellow and red, while it will change to a combination of yellow and red when all the lithium ions are

removed from the layer to form λ-MnO_2. Thus, the quantitative description is well in agreement with the qualitative color change reported by Roeder et al.[83].

Figure 3-7(b) depicts the change in the real part of the CRI. As stated above for Figure 3-7(a), these dispersion curves may show regions of anomalous dispersion due to the presence of certain resonance frequencies. The exact values of the resonance frequencies are given in Table 3-1 which points out four resonant wavelengths (λ_{0j}) values for each charge state corresponding to the four relevant oscillators. The first (λ_{01}) and last wavelength (λ_{04}) do not fall into the spectral range of the spectrometer and therefore are only approximate. However, they are required in achieving a nearly perfect fit (all R^2>0.996). The effect of lithium intercalation by plotting the resonant wavelength λ_{02} and λ_{03} (the two resonant wavelengths which are in the spectral range of the spectrometer) versus the lithium content, is shown in Figure 3-7(c). To attribute these resonant wavelengths

***Table 3-1**: Fitting Parameters (for the 4 oscillators) for different lithium concentration.*[E1]

At. fraction of Li	$x = 0$	$x = 0.2$	$x = 0.4$	$x = 0.6$	$x = 0.8$	$x = 1$
$N \times 10^{26}$ (m^{-3})	1.14±0.02	1.12±0.02	1.30±0.01	1.22±0.04	1.21±0.04	1.27±0.04
f_1	9.27±1	9.81±1	15.58±1	4.67±2	6.84±2	6.54±2
λ_{01} (nm)	473.35±5	464.30±5	480.76±5	349.68±15	358.02±15	250.94±15
$\gamma_1 \times 10^{15}$ (rad s^{-1})	0.99±0.1	1.09±0.2	1.46±0.2	5.14±1	4.42±1	13.19±1
f_2	6.63±0.3	7.87±0.3	0.39±0.1	14.49±0.1	13.51±0.1	15.22±0.1
λ_{02} (nm)	555.30±5	542.69±5	536.17±5	481.30±5	466.74±5	445.46±5
$\gamma_2 \times 10^{15}$ (rad s^{-1})	0.72±0.05	0.90±0.05	0.32±0.05	1.37±0.05	1.38±0.05	1.52±0.05
f_3	3.80±0.1	3.61±0.1	3.71±0.1	4.55±0.1	5.26±0.1	5.24±0.1
λ_{03} (nm)	658.15±4	641.83±4	615.31±4	603.68±4	590.92±4	571.67±4
$\gamma_3 \times 10^{15}$ (rad s^{-1})	0.42±0.02	0.45±0.02	0.55±0.02	0.64±0.05	0.74±0.05	0.76±0.05
f_4	0.24±0.03	0.42±0.03	0.59±0.03	0.89±0.1	0.87±0.1	0.93±0.1
λ_{04} (nm)	1076.85±10	1100.83±10	1159.37±10	1136.64±1	1123.05±10	1122.31±10
$\gamma_4 \times 10^{15}$ (rad s^{-1})	0.25±0.05	0.31±0.05	0.30±0.05	0.08±0.01	0.07±0.01	0.10±0.01
Quality of Fit, R^2	0.998	0.997	0.997	0.997	0.997	0.997

to a particular electronic transition, the predicted density of states (DOS) of LMO (shown in Figure 3-7(d) data taken from Liu et al.[78]) is considered. From Figure 3-7(c), it is seen that both λ_{02} and λ_{03} are decreasing with the increasing amounts of lithium. This indicates that the electronic transition energy increases when lithium is intercalated into the spinel structure. Comparing this with Figure 3-7(d), it is noticed that this is only possible for the transitions occurring between the occupied O-2p band and the empty split Mn-d bands lying above the Fermi level, as these are the only possible transitions in which the energy gap is increasing upon lithium intercalation.

For $x = 1$, the two resonant wavelengths are 445.5 nm (2.8 eV) and 571.7 nm (2.2 eV) whereas for $x = 0$, these resonant wavelengths are 555.3 nm (2.2 eV) and

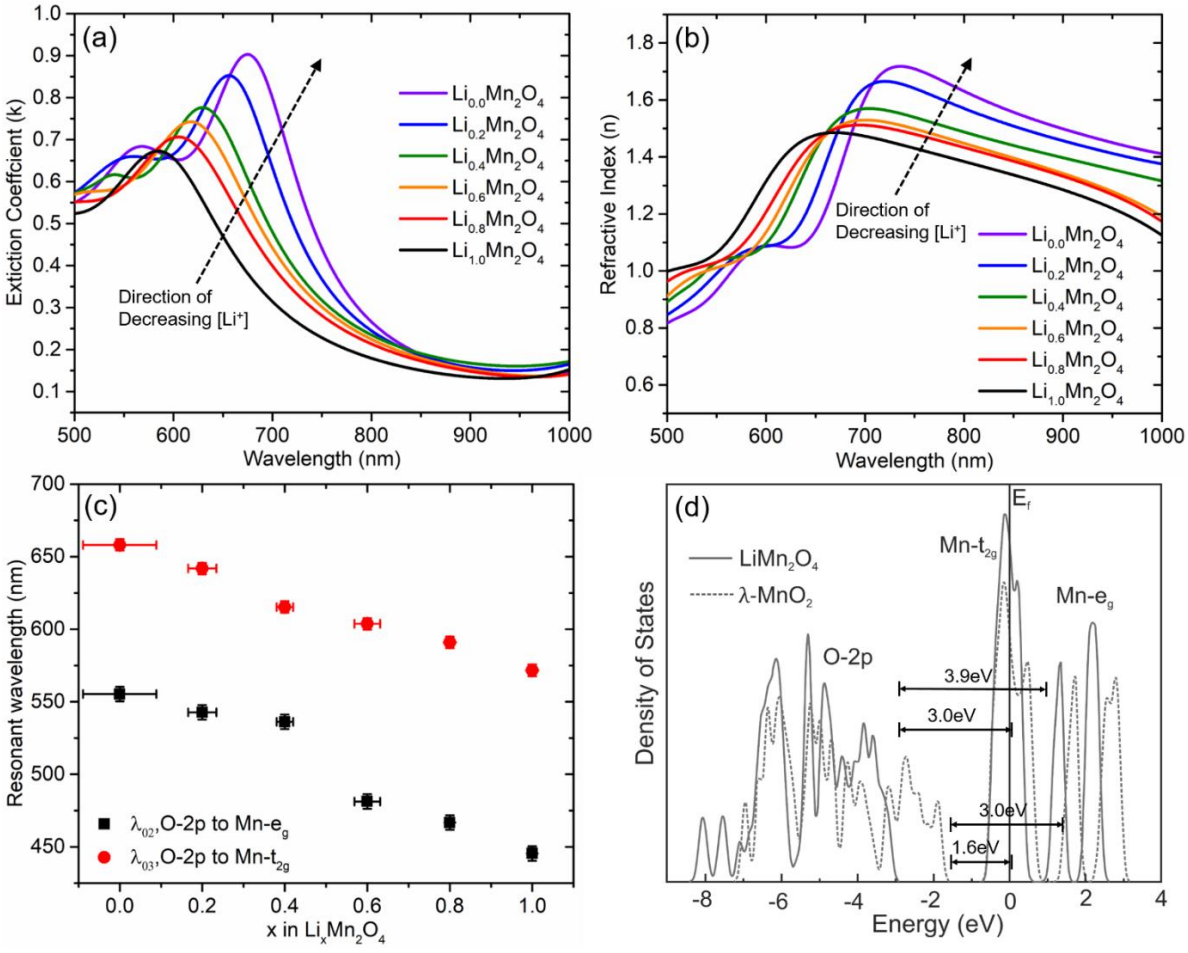

***Figure 3-7**: (a) Imaginary part and (b) real part of the CRI and its change upon (de-)lithiation; (c) Dependence of resonant wavelength i.e. λ_{02} and λ_{03} corresponding to the O-2p to Mn-eg and O-2p to Mn-t_{2g} electronic transition in accordance to the change in band structure[42] with the Li stoichiometry, as shown in (d).*[E1]

658.1 nm (1.8 eV) (see Table 3-1). These values clearly confirm the general trend reported by Aydinol et al.[101] in a first-principle-based study. They revealed stabilization of the valence band upon intercalation of Li into the transition metal oxides such as TiO_2, VO_2, MnO_2 (layered), CoO_2, NiO_2, etc. Liu et al.[78] solidified this argument of stabilization of the valence band upon lithium intercalation particularly for $LiMn_2O_4$ as demonstrated in Figure 3-7(d). They revealed the electronic transition energy between the O-2p band and the Mn-e_g as 3.9 eV for $x = 1$ and 3.0 eV for $x = 0$ and between the O-2p and Mn-t_{2g} band as 3 eV for $x = 1$ and 1.6 eV for $x = 0$. A summary of other theoretical works on DOS for LMO is given in Table 3-2. As is clearly observable, the respective values do not agree well with each other. This could be due to the fact that different approximations are used in these theoretical studies and also due to the different number of unit cells considered in the calculations. So a real matching cannot be expected in the quantitative numbers. But, the two major factors that are consistent between the theoretical studies of Liu et al.[78], and Berg et al.[87] and our experimental data are: the splitting of the Mn-d orbital and the stabilization of the valence band upon Li intercalation. Remarkably, the most recent work of Young et al.[85] using the hybrid functions, reported the stabilization of the conduction band but at the same time a decrease in the energy gap between the O-2p band and split Mn-d band upon Li intercalation which would mean a depreciated shift in the valence band upon lithiation. This stands in qualitative contrast to the previously established theoretical results of Liu et al.[78] and Berg et al.[87] that asserts an enhanced stabilization of valence band. Now, this is also inconsistent with the new measurements presented here. Further clarification of the theoretical band structure predictions in view of the new experimental data is suggested.

Quantitatively, the absorption peaks and resonant wavelengths for the fully intercalated state ($x = 1$) as presented here are in close agreement with the experimental observations of Kushida and Kuriyama[102]. They investigated only the fully lithiated LMO by transmission spectroscopy (in the wavelength range of 300-

2500 nm) and reported a strong absorption peak (or resonance) at around 400 nm (or 3.1 eV) corresponding to the O-2p to Mn-t_{2g} transition which is in agreement with this study. But two additional absorption peaks at the wavelengths of 760 nm (1.6±0.19 eV) and 620 nm (2.00±0.16 eV) were assigned to two t_{2g}-e_g transitions instead of the transitions of O-2p into the split Mn-d band. A confirmation of these suggested transitions, possibly by measuring different charge states, was not reported. But in comparison to the predicted dependence of the band structure on intercalation, these earlier suggested d-d transitions cannot explain the experimentally observed decrease of the λ_{02} and λ_{03} with intercalation of lithium.

***Table 3-2**: Previously reported values for the corresponding electronic transition arranged chronologically and the effect of lithiation on the transition energies. Last row details the values determined in this study.[E1]*

Author	Assumption or Methodology	$LiMn_2O_4$	λ-MnO_2	$LiMn_2O_4$	λ-MnO_2	Effect of Li intercalation	
		O-2p to Mn-e_g (eV)	O-2p to Mn-e_g (eV)	O-2p to Mn-t_{2g} (eV)	O-2p to Mn-t_{2g} (eV)	Δ(2p-e_g) (eV)	Δ(2p-t_{2g}) (eV)
Mishra and Ceder (1998)[73]	LDA/DFT; same result with GGA (Minority spin)	4.4	--	2.6	--	--	--
Liu et al. (1999)[78]	Molecular orbital; DV-Xα method [78,170–172]	3.9	3.0	3.0	1.6	0.9	1.4
Berg et al. (1999)[87]	LMTO method in ASA	4.0	3.7	2.4	1.8	0.3	0.6
Grechnev et al. (2002)[77]	Full-potential LMTO electronic structure method [173]	2.2	--	1.2		--	--
K. Hoang (2014)[86]	Hartree-Fock/DFT; Heyd-Scuseria-Ernzerhof [174,175]	3.8	--	1.4		--	--
Young et al. (2016)[85]	UEB/ hybrid DFT[176]	2.8	3.1	1.6	2.3	-0.4	-0.7
This Work	Experimentally by Clausius-Mossotti [21,22]equation	2.8	2.2	2.2	1.8	0.4	0.4

[a)]LDA: Local Density Approximation; [b)]DFT: Density Functional Theory; [c)]GGA: Generalized Gradient Approximation; [d)]DV-Xα: Discrete Variational Xα; [e)]LMTO: Linear Muffin-tin Orbital; [f)]ASA: Atomic Spheres Approximation; [g)]UEB: Unified Electrochemical Band)

Henceforth, it is concluded that λ_{02}, and λ_{03} represent the transition energies corresponding to the O-2p to Mn-e_g and O-2p to Mn-t_{2g} transitions, respectively.

To propose LMO as a viable candidate for the application of optical switching, a quantification of the expected phase shift and intensity modulation due to the lithium de/intercalation is needed:

$$\Delta\varphi = \frac{2\pi}{\lambda} \cdot \Delta n \cdot l \qquad 3\text{-}5$$

Using Equation 3-5 the change of phase ($\Delta\varphi$) of light passing through a path of length l when the refractive index of a material changes by Δn, for a particular wavelength of λ, can be quantified. Thus, determining the change in refractive index from Figure 3-7(b), for that for a wavelength of 750 nm a 1345 nm thick layer of LMO would be required to achieve a phase shift of π when switching between x = 0 to x = 1.

Furthermore, the attenuation of light may be accounted for in terms of the Insertion Loss (I.L.) and Extinction Ratio (E.R.) defined by Equation 3-6 and 3-7.

$$I.L. = -10 \cdot \log_{10}\left[e^{\left(\frac{-4\pi k}{\lambda}\cdot l\right)}\right] \qquad 3\text{-}6$$

$$E.R. = I.L._{x=1} - I.L._{x=0} \qquad 3\text{-}7$$

According to the data in Figure 3-7(a), an 1873 nm thick film of LMO would be required to achieve an E.R. of 30 dB at a wavelength of 750 nm. These two estimates make it obvious that an efficient optical switching may indeed be achieved by using the battery material in the optical field.

3.4 Summary

The optical response of thin films of the spinel $Li_xMn_2O_4$ (LMO) on Li intercalation, studied in the wavelength range between 500nm-1000 nm, demonstrates that the complex refractive index can be controlled by adjusting the Li content in the LMO. Quantification of the optical constants can be achieved as a function of the

intercalation state by fitting the Clausius-Mossotti expression to the measured reflectance spectra. Two significant resonances are present within the visible region of the wavelength spectrum. They are attributed to electronic transitions between the O-2p band and the split Mn-d band. The feasibility of in-situ measurements is demonstrated. They confirm the well-reversible optical behavior of the LMO layers, which enable independent kinetic studies of the intercalation reaction.

The variation of the real and imaginary part of the refractive index is so pronounced that it allows accurate optical switching using devices of micrometer size. Thus, LMO is an electrochromic material with very promising properties to be utilized in active optical devices.

4 Electrochromic Behavior in $Li_{4+x}Ti_5O_{12}$ upon Li-Ion De/-Intercalation

The previous chapter sets up the strategy to investigate the optical properties of battery materials. In this chapter, the methodology is extended to investigate a more complex system, namely lithium titanate, undergoing a phase transformation upon lithium insertion/removal. Lithium titanate or $Li_{4/3}Ti_{5/3}O_4$ or $Li_4Ti_5O_{12}$ (LTO) is considered one of the most promising anode materials for high power applications. This is due to its safe operating voltage, high cyclic stability, and *zero-strain* phase transformation during de-/intercalation of lithium.[103,104] It has a theoretical capacity of 60.8 $\mu Ah \cdot cm^{-2} \cdot \mu m^{-1}$ (or 175 mAh g^{-1}). The electrochemical activity in terms of lithium insertion in the material was first explored by Murphy et al. in 1983[105]. However, only in 1995 Ohzuku et al. exhibited its use in lithium-ion battery application and reported a nearly constant dis-/charge voltage of 1.55 V vs Li/Li^+.[10] This nearly constant voltage for de-/intercalation is indicative of a phase transformation during lithium insertion/removal. However, this phase transformation at room temperature and on a macroscopic scale has been debated in the past, with reports suggesting solid solution[106] and/or nano-domains[68] in an equilibrium condition. Nonetheless, the existence of the two phases was confirmed by direct imaging, i.e. the spinel structured $Li_{4/3}Ti_{5/3}O_4$ being transformed into the rock-salt type $Li_{7/3}Ti_{5/3}O_4$ upon lithium insertion using high-resolution transmission electron microscopy[107].

A unit-cell of $Li_{4/3}Ti_{5/3}O_4$ has 8 formula units with 32 oxygen atoms located at the 32e sites, 1/3rd of the lithium and all of the titanium atoms are occupying the 16d sites (or octahedral position) and the remaining 8 atoms of lithium are at the 8a sites (or tetrahedral position), see Figure 4-1 (a).[108] During the phase transformation to $Li_{7/3}Ti_{5/3}O_4$ phase upon lithium insertion, the atoms of lithium at the 8a sites (tetrahedral position) shift to the 16c position (octahedral position) and

the insertion of eight additional lithium atoms takes place in vacant 16c position thus filling up all of the octahedral sites.[10,108] The unit cell of $Li_{7/3}Ti_{5/3}O_4$.is shown in Figure 4-1 (b).

The preparation of powdered lithium titanate has been reported via various methodologies such as sol-gel technique,[109] hydrothermal treatment,[110] combustion technique,[111–116] spray pyrolysis.[117] For the thin-film deposition, several routes have been proposed such as r.f.-magnetron sputtering,[118] pulsed

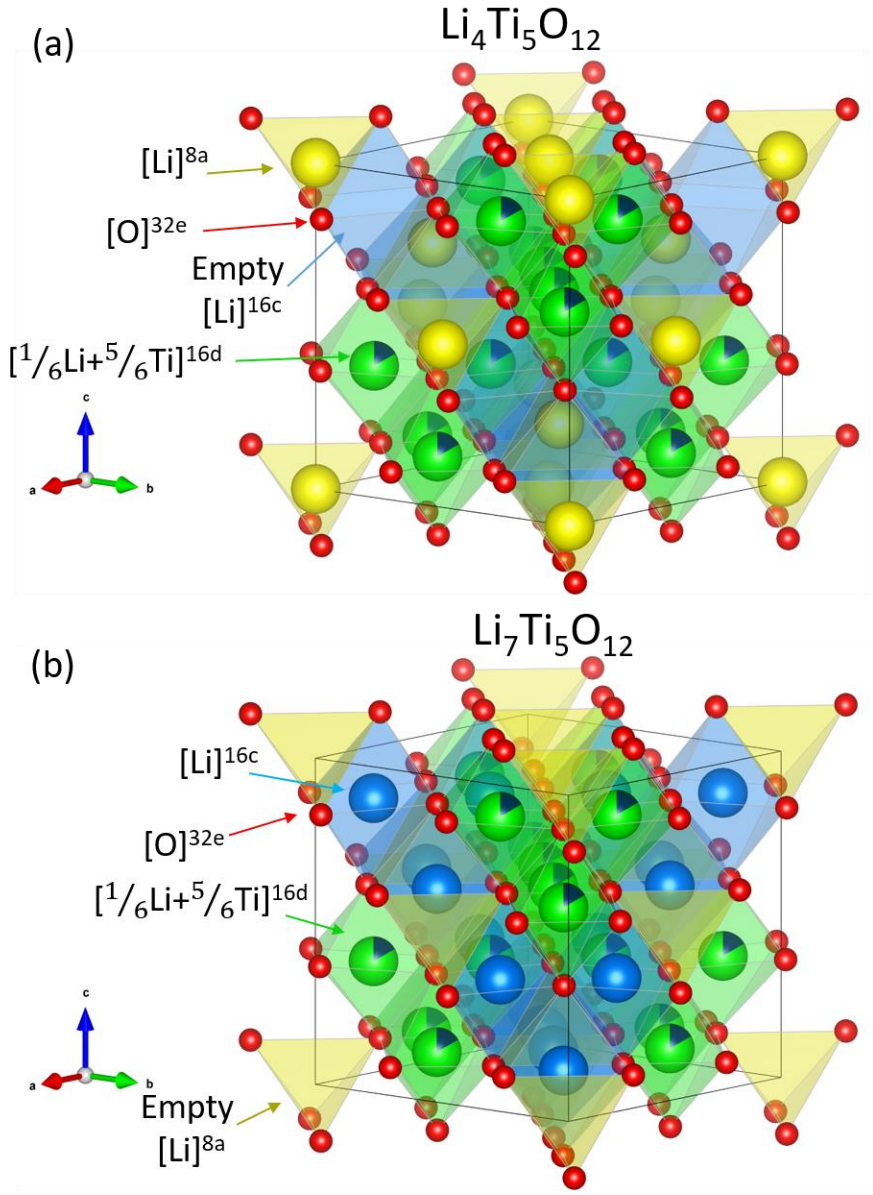

***Figure 4-1**: A unit cell of (a) $Li_4Ti_5O_{12}$ and (b) $Li_7Ti_5O_{12}$. The red, green, dark blue light blue, and yellow atoms are of oxygen, titanium, lithium at 16d, lithium at 16c, and Lithium at 8a, respectively.*

laser deposition,[119] dc-ion beam sputtering,[120] metal-organic chemical vapor deposition[121].

Regarding the optical properties, Ohzuku et al. reported an interesting change of color, i.e. from white (powdered) $Li_4Ti_5O_{12}$ phase to a blue $Li_7Ti_5O_{12}$ phase, upon lithiation.[10] This electrochromic switching was confirmed by Yu et al. in 2010 by depositing thin films of LTO on a transparent conductive oxide using pulsed laser evaporation.[122] Since then the same behavior has been confirmed experimentally by others as well.[83,123] These observations are in general agreement with the electronic structure of the material.[108,124–132] This is because $Li_4Ti_5O_{12}$ is observed as a poor electronic conductor (hence should be transparent in the visible region of light due to wide bandgap), whereas $Li_7Ti_5O_{12}$ shows metallic conductivity. However, the quantitative description of the electrochromic behavior (or the complex refractive index) with the band structure of the material was explored only recently by Joshi et al.[E2] The article was published by the author towards the completion of this thesis and the present chapter discusses its findings.

The change of color is an indicator for an alteration in the electronic transition caused by the incident EM wave. And hence as already established, it could mean a corresponding change in the optical constants and also the dielectric properties (as they are linked to the optical constants). Recently, in 2019, a theoretical study by Li et al.[130,132] simulated the electrochromic behavior of $Li_4Ti_5O_{12}$ based on the predicted electronic structure at different charge states using first-principle calculations. However, the principal two-phase reaction upon lithium insertion and the geometric distribution of the grains was not considered when generating the optical spectrum. The present chapter aims at filling this gap by quantitatively measuring and analyzing the optical spectrum. To realize the goal, the current chapter seeks the quantification of the complex refractive index (CRI) of $Li_4Ti_5O_{12}$ and $Li_7Ti_5O_{12}$ and intermediate charge states comprising a heterogeneous mixture of the two phases. Thereby obtaining an experimentally detailed description of the

optical dispersion during the electrochemically activated phase transition. Furthermore, the CRI will be interpreted in terms of the complex dielectric function (CDF). A change of the real versus the imaginary part of this dielectric function provides insight into the geometric arrangement of the two phases and thus the mechanism of the phase transformation in LTO. This is due to the fact that the optical properties of the intermediate charge states depend on the geometric phase arrangement and hence the microstructure.

4.1 Experimental realization

4.1.1 Thin-film preparation:

Here again r.f. ion beam sputtering was used for the deposition of the thin films. The Lithium titanate target was made by cold pressing the powder (EXM 1037-$Li_4Ti_5O_{12}$, Südchemie). As done for the LMO, the cold-pressed powder was glued to a steel plate for mechanical stability.[120] The sputter deposition of LTO was carried out in argon and oxygen atmosphere present in 9:1 ratio respectively. This is done to avoid any oxygen loss during sputtering. The active layer i.e. LTO was deposited upon an already deposited platinum layer (100nm thick, deposited with only argon i.e. without any reactive gas) serving as a current collector and as an optical reflector. Polished oxidized silicon wafers were used as the substrate for the deposition. The ion beam was accelerated by a voltage of 700 V and the corresponding r.f. power used to generate the argon plasma was 130 W. The base pressure prior to sputtering was below 1×10^{-7} mbar. The total working pressure during LTO deposition was 5.4×10^{-4} mbar. The deposited films were annealed in vacuum at 550°C for 30 min[134] to achieve the optimum electrochemical performance.

The crystallinity of the annealed sample was confirmed using a Bruker D8 general area detection diffraction system (GADDS) in grazing incidence geometry. An incident angle of 10° was used to perform 2θ scans using Cu-Kα (λ = 1.54 Å) radiation. The microstructure and the morphology of the layers along the depth of

the film were determined using transmission electron microscopy (Philips CM200-FEG).

4.1.2 Electrochemical characterization

The electrochemical measurements were carried out using a three-electrode setup as described in the previous chapter in Section 3.1.2. In this case, the LTO/Pt serves as the working electrode (WE) and two lithium foils serve as a counter (CE) and a reference electrode (RE). Hence, all the potential differences are measured with respect to lithium. The electrochemical cells were assembled in an argon-filled glovebox.

4.1.3 Electrochromic characterization

Ex-situ reflectance spectroscopy

The same setup, as described in Section 3.1.3, was used. The ex-situ reflectometry was performed at stable charge states ranging from $0 < x < 3$ in $Li_{4+x}Ti_5O_{12}$. To reach these states, the samples were first delithiated to 2V (at each step) and then subsequently lithiated to the required voltage corresponding to a specific charge state as determined before by chronopotentiometry. Once the desired voltage has been reached, the sample is maintained at this voltage using chronoamperometry until the current drops to 0.2 µA (roughly 6 h equilibration period). After this quasi-equilibrium state has been reached, the sample is cleaned with dimethyl carbonate and dried under argon. Subsequently, the sample is transferred into a sealed cell having flat, optically transparent faces (made from optical grade quartz glass). This is done to avoid the reaction of the $Li_7Ti_5O_{12}$ phase with the moisture present in the air. The transfer of the sample from the electrochemical cell to the sealed cell was done in an argon-filled glovebox. Reflectance spectroscopy was performed at normal incidence.

In-situ reflectance spectroscopy

A similar setup was used as described in Section 3.1.3, only this time, a redesigned cell was used which enabled the use of a three-electrode setup instead of the two-

electrode setup used in the previous chapter. LTO was acting as the WE, and two lithium foils were acting as RE and CE.

4.2 Results

4.2.1 Structural characterization

Figure 4-2(a) shows the X-ray diffraction pattern (XRD) of the annealed sample (550°C for 30 min in vacuum). All the reflections could be indexed either to spinel structured $Li_4Ti_5O_{12}$ or to Pt which is the current collector underneath the LTO layer. To confirm the phase purity on a microscopic scale, selected area electron

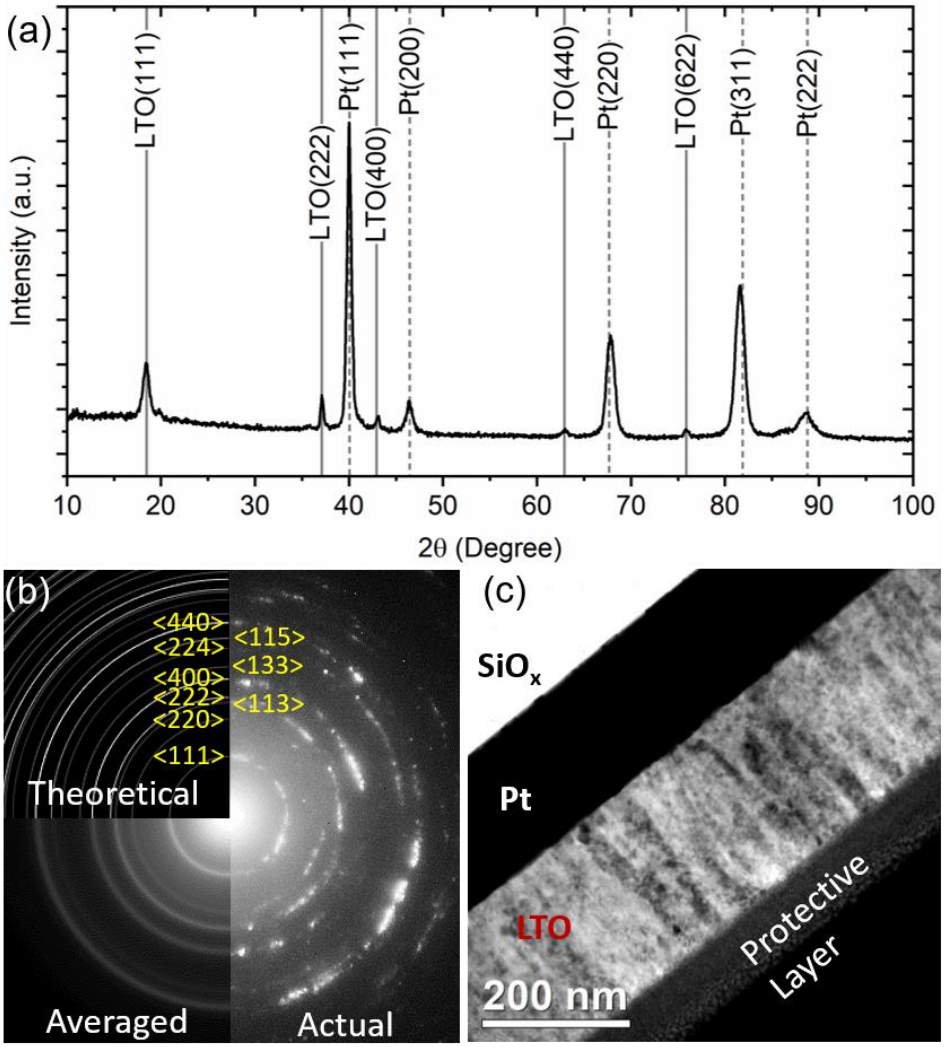

***Figure 4-2**: (a) X-ray Diffraction, using Cu-Kα, of the annealed LTO film; (b) Selected area electron diffraction pattern of the annealed film, right side of the figure shows the actual pattern, bottom left part is the azimuthally averaged diffraction pattern and top left part is the theoretical diffraction pattern of spinel structured $Li_4Ti_5O_{12}$; (c) Bright Field Transmission Electron Microscopy image of the annealed film (cross-section).*[E2]

diffraction (SAED) is performed from the LTO layer (i.e. avoiding the Pt layer) as shown in the pattern of Figure 4-2(b). The experimental diffraction pattern is shown on the right half of the figure whereas the azimuthally averaged pattern is shown in the bottom-left quarter of the figure. Both of these are in good agreement with the predicted pattern of $Li_4Ti_5O_{12}$ shown in the top-left quarter of the figure (as generated by Crystbox[135]). All the reflections are indexed for the spinel structure hence confirming its presence and the phase purity of the layer. Furthermore, Figure 4-2(c) shows the morphology of the multilayered system in bright-field TEM (BF-TEM). A well-defined and smooth LTO layer (with a thickness of 232 ± 5 nm) is seen which shows a columnar grain structure, as is frequently observed for sputter-deposited thin-films.

4.2.2 Electrochemical characterization

Figure 4-3 shows the cyclic stability of the annealed thin-film and the inset figure shows the effect of varying the charging rate on the capacity of the thin film electrode. A gradual drop from 2nd until the ending 80th intercalation step is

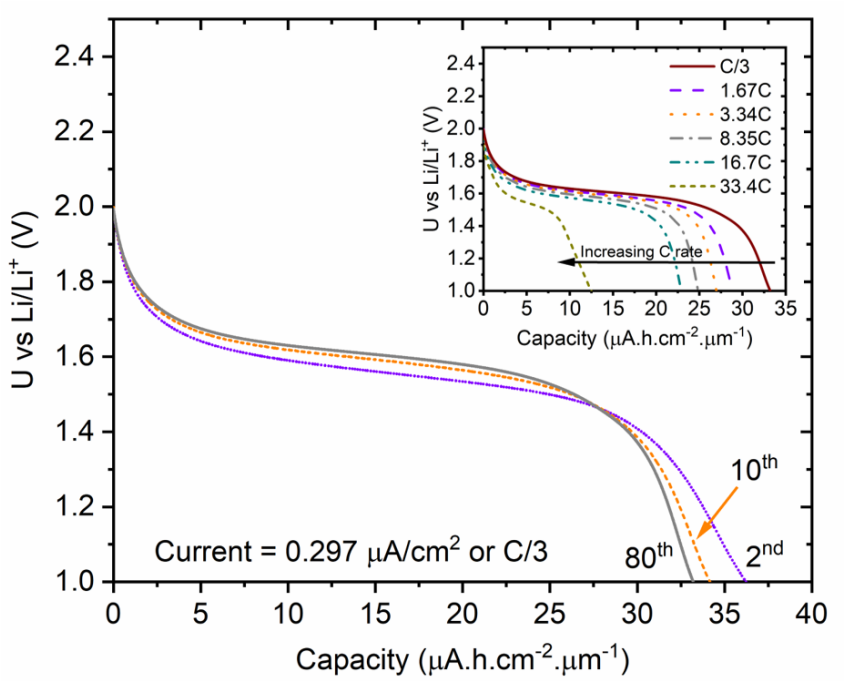

***Figure 4-3**: Chronopotentiometry (intercalation step) of the annealed sample showing the loss of capacity with cycling. The inset shows the effect of the charging rate on the capacity of the thin film electrode.[E2]*

observed. A closer look at the capacity reveals that the drop from the 2nd to the 10th intercalation cycle is more pronounced (capacity loss of ca 5.7%) than the drop between the 10th and 80th cycle (capacity loss of ca 2.7%). A similar stabilization of capacity was also reported by Colbow et al.[136], where they reported a stable performance of the electrode only after 25 cycles.[137] This is due to structural relaxation during the initial cycles.[138] To avoid any significant effects of structural relaxation, all the reflectivity measurements were performed after at least 40 running-in cycles. Nevertheless, the capacity for the 2nd cycle is 36.23 µAh cm^{-2} μm^{-1} which drops to 34.15 µAh cm^{-2} μm^{-1} after 10 cycles and finally at the end of the 80th cycle it amounts to 33.21 µAh cm^{-2} μm^{-1}. It should be noted here that the insertion plateaus are slightly shifted from the theoretical voltage of 1.55 V which is probably due to the dynamic nature of charging, i.e. the films are never in exact equilibrium. A similar behavior was pointed out by Rho and Kanamura,[139] when they compared EIS, PITT and CV. They observed in the case of EIS the voltage values were closest to 1.55 V which they obtained by maintaining the sample at this voltage for more than 4 hr. Also the nano-crystalline nature of the deposited thin-films could affect the insertion voltages and the voltage profile.[140] The inset figure demonstrates the fast dis-/charge capability of the battery electrode, where it has been cycled up to 33.4 C-rate (i.e. dis/charge in approx. 2 minutes). As mentioned before, $Li_4Ti_5O_{12}$ is a poor electronic conductor, so such high rate capability can only be explained by the thin film geometry which provides much shorter electronic diffusion lengths (refer to Discussion section).

4.2.3 Electrochromic characterization

Figure 4-4 demonstrates the electrochromic behavior of LTO in reflectance spectroscopy. Figure 4-4(a) shows the CV of the material, measured at a scan rate of 0.5 mV s^{-1}. The optical spectrum, collected from selected voltages, is shown in Figure 4-4(b), and the corresponding voltages are marked with the colored arrows in Figure 4-4(a). From Figure 4-4(a) and (b) It can be concluded that the highest reflectivity was obtained in the $Li_4Ti_5O_{12}$ phase at 2 V. The maximum reflectivity

reaches a value close to 80% reflectance at the wavelength of about 1000 nm. This agrees with the previous reports stating that $Li_4Ti_5O_{12}$ films are optically transparent.[83,122,123] Furthermore, it can be seen that during the first half of lithiation i.e. from 1.99 V to 1.55 V, a pronounced drop in the reflectance (from ca 76% to 26% for λ = 951.67 nm) is observed whereas in the second half i.e. from 1.55 V to 0.99 V only a slight drop in the reflectance spectrum appears (from ca 26% to 19% for λ = 951.67 nm). This behavior is better visualized for a single wavelength, for instance for λ = 951.67 nm, in Figure 4-4(c). In the figure, the

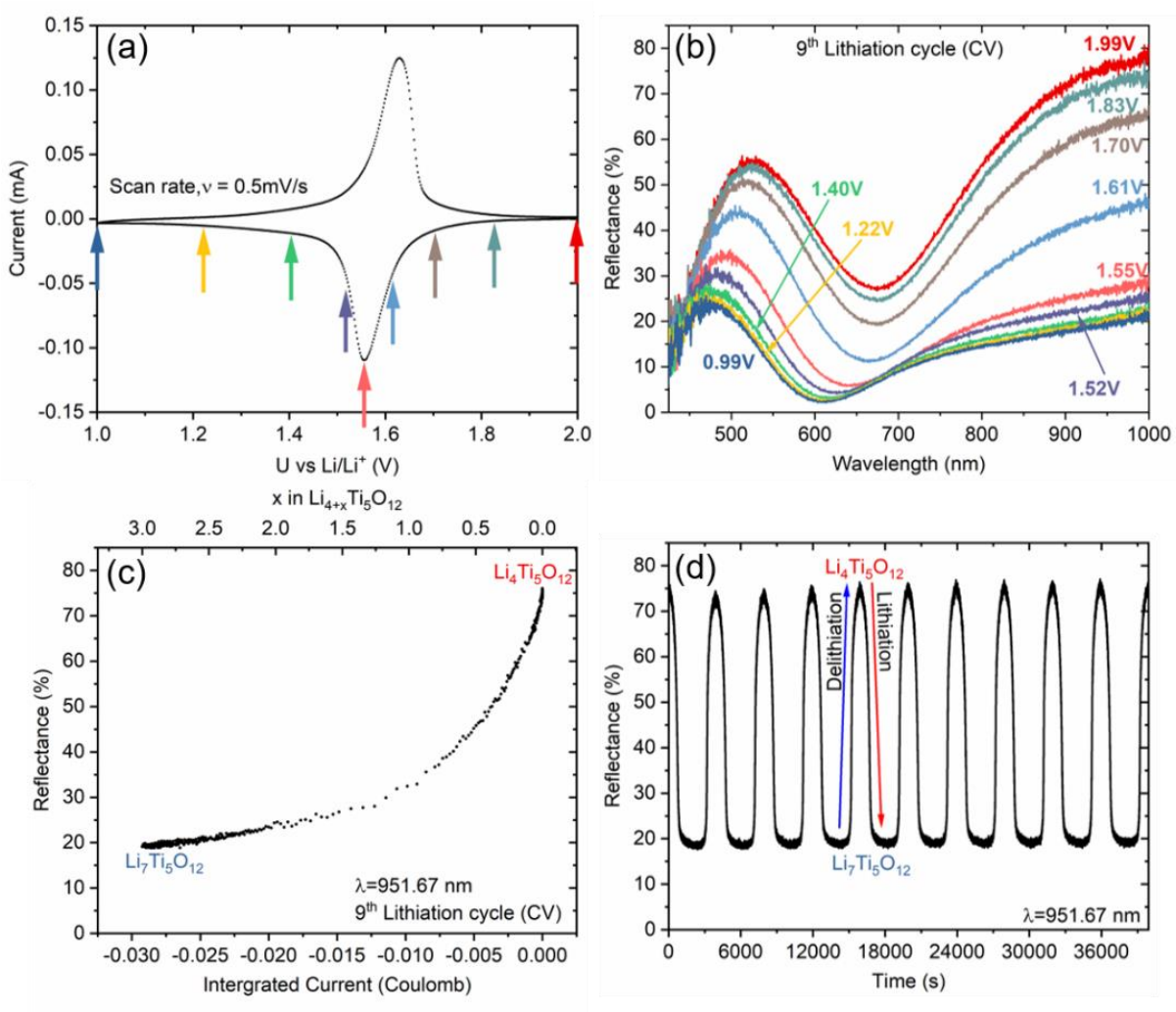

***Figure 4-4**: (a) Cyclic voltammogram at a scan rate of 0.5 mV s^{-1} as measured during in-situ reflectance spectroscopy, arrows (colored) indicating the charging states of the corresponding spectra in (b); (b) reflectance spectra at different voltages as marked by arrows in (a); (c) change of reflectance as a function of lithium content (top axis) at the selected wavelength of 951.67 nm; (d) Reversibility of the reflectance for the wavelength of 951.67 nm in 10 CV cycles.[E2]*

reflectance change versus the integrated current (from the CV) is shown. The integrated current represents the intercalation state as is clear from the upper axis of the graph. It can be seen that lithiation leads to a decrease of the reflectance from ca 76% (in the fully delithiated state) to ca 19% (in the fully lithiated state). This drastic drop in the reflectance spectra can be understood by the extinction coefficient (or absorption of light) as will be discussed in the subsequent section. Now, the optical reversibility is verified in Figure 4-4(d) during 10 CV cycles at the wavelength of 951.67 nm. There is practically no loss in the reflectance, the material exhibits an almost perfect reversible electrochromic behavior. From these data, a remarkable relative change of ca. 57% in reflectance at the extreme voltages of 1.99 V and 0.99 V must be pointed out. These results strongly suggest the potential to utilize this material for applications such as electrochromic mirrors and windows. The application of this material can also be extended to optical actuators as suggested in reference[141] and the motivation section of chapter 1.

To quantify the presented results in terms of CRI, the reflectance spectra are determined at quasi-equilibrium states using ex-situ reflectance measurements. Figure 4-5(a) shows the constant current or the CP measurement corresponding to the lithiation step used to prepare the charge states. The dashed lines mark the

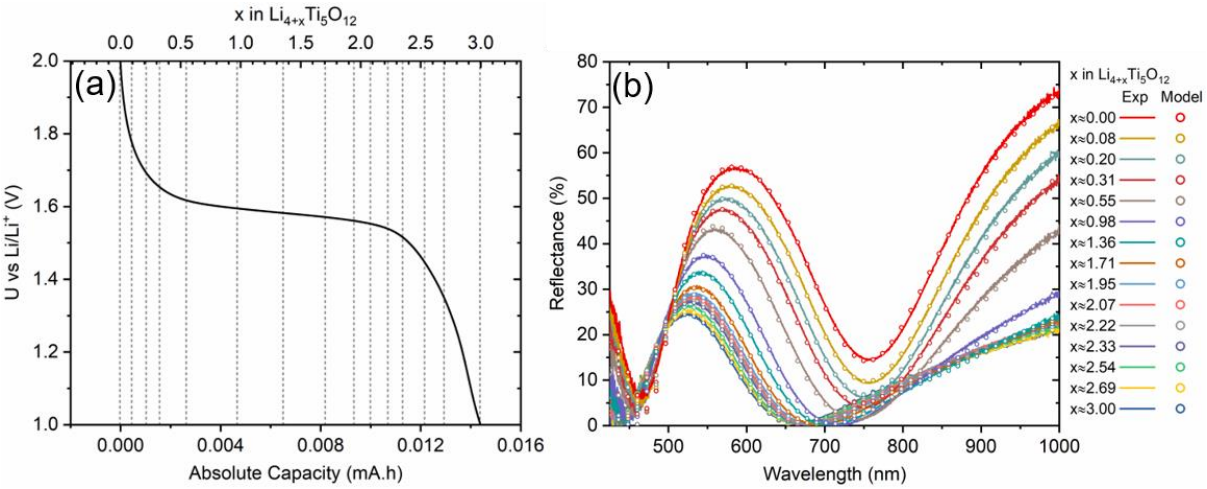

***Figure 4-5**: (a) Chronopotentiometry plot of intercalation of lithium into $Li_4Ti_5O_{12}$. Dashed lines indicate the charge states at which ex-situ spectra are measured. (b) Ex-situ reflectance spectra at different charge states as marked in (a). Solid lines represent the measured data, while open circles represent the result of the fitted analytical model.[E2]*

charge states (shown in top axis) at which the reflectance spectra are taken. Figure 4-5(b) presents the measured spectra (solid lines) of the films at different charge states between 0<*x*<3 as labeled, where *x* represents the stoichiometric amount of lithium inserted in $Li_{4+x}Ti_5O_{12}$. Hollow circles represent the result of the model description (see next section).

4.3 Discussion

4.3.1 Complex refractive index and electronic structure

As in the case of LMO, the CRI of LTO is described using the Clausius–Mossotti[21,22] relation, given by Equation 1-8. Once the mathematical description of the CRI is established, the sample geometry is considered for calculating the reflectance as stated by Equation 3-3. Only in this case, the LMO layer is replaced by LTO layer acting as medium 2. Here also the model description is completed by adopting the CRI of the platinum from the work of Werner et al.[96]. This enables us to calculate Fresnel's reflection coefficient between the active layer of LTO and Pt (i.e. r_{23}) and the theoretical reflection of platinum which is used as reference (i.e. r_{13}) in the reflectance spectrum. Since the measurements are performed in a sealed argon cuvette, argon acts as medium 1 for which the CRI is set to be equal to 1.[142,143] Subsequently, applying Equation 3-3 and 1-8 for different wavelengths, the spectra of Figure 4-5(b) are modeled. In the present case, two oscillators are used in Equation 1-8. Now the required parameters are determined by best fitting to the experimental data. Initialization of the resonant wavelength/frequency was made by considering the work of Liu et al.[128] Subsequently, all the parameters (namely $N \cdot f_j$, γ_j, and ω_{0j}) were fitted iteratively using a Levenberg–Marquardt[98,99] algorithm to minimize the residual. A point to note, attempts were made to fit the spectra with one and three oscillators as well. In the former case, the fit was not satisfactory, in the latter case, the fit parameters were not consistent for all the spectra, probably due to over parametrization. The derived model spectra are shown in Figure 4-5(b) by hollow circles. The optimized parameters are summarized in Table 4-1. With the fit parameters, the real and imaginary parts of

***Table 4-1**: Fitting parameters used to fit the spectra shown in Figure 4-5(b) at different charge states i.e. for 0<x<3 (x corresponds to amount of lithium in $Li_{4+x}Ti_5O_{12}$).*[E2]

At. fraction of Li	Nf_1	λ_{01} (nm)	$\gamma_1 \times 10^{15}$ (rad s^{-1})	Nf_2	λ_{02} (nm)	$\gamma_2 \times 10^{15}$ (rad s^{-1})	Quality of Fit, R^2
***x* = 0.00**	0.13546	753.24	0.536757	1.26141	428.429	428.429	0.9989
***x* = 0.08**	0.167368	753.831	0.563661	1.40045	422.766	0.541927	0.9989
***x* = 0.20**	0.199658	752.89	0.590603	1.57734	415.626	0.570241	0.9986
***x* = 0.31**	0.230478	752.195	0.610856	1.86085	405.537	0.609723	0.9979
***x* = 0.55**	0.311383	751.823	0.629569	2.90879	375.192	0.720096	0.9969
***x* = 0.98**	0.498834	769.057	0.553158	3.85082	351.849	0.943839	0.9976
***x* = 1.36**	0.570036	771.374	0.612947	4.02172	346.914	1.04517	0.9982
***x* = 1.71**	0.614643	765.126	0.639901	4.12397	343.454	1.16588	0.9986
***x* = 1.95**	0.636685	760.975	0.649815	4.09751	343.703	1.20228	0.9987
***x* = 2.07**	0.652684	759.054	0.663268	4.36924	337.947	1.26406	0.9991
***x* = 2.22**	0.663115	758.73	0.657545	4.33958	337.406	1.29959	0.9989
***x* = 2.33**	0.680032	757.79	0.684491	4.57342	333.525	1.32957	0.9993
***x* = 2.54**	0.708736	756.305	0.697643	4.45511	335.468	1.31946	0.9991
***x* = 2.69**	1.31946	755.815	0.716797	4.54387	333.933	1.37757	0.9991
***x* = 3.00**	0.739391	755.118	0.714125	4.34697	337.471	1.36101	0.9992

the CRI are calculated as shown in Figure 4-6(a) and (b). It should be noted here that even though the spectra are only measured for the wavelength range between 425 nm to 1000 nm, the CRI may even be reasonably described for an extended extrapolated wavelength range of 300 nm to 1000 nm. The lower resonance wavelength (or higher energy) falls just outside the range of the spectrometer, hence only a small error could appear.

From Figure 4-6(a) and (b), the evaluated change of CRI is shown when lithium is inserted from $x = 0$ to $x = 3$. From the quantitative data of Figure 4-6 (a), the reported change of color of LTO can be well understood. The $Li_7Ti_5O_{12}$ phase is known to exhibit a blue color. This corresponds to a broad extinction maximum at around 600 to 900 nm (red to infra-red) in the figure (for $x = 3$, blue curve). Thus, red light is mostly absorbed leaving blue-green in the visible spectrum. By contrast,

the $Li_4Ti_5O_{12}$ phase is known to be transparent in the full visible range. From the figure, for x=0 (red curve), the layer exhibits less absorption (or extinction coefficient) in the visible range (450-750 nm) which indicates the transparent nature of the film. To explain these observations in terms of electronic transitions, a closer look at the band structure is needed.

Several studies have reported the band structure of the terminating $Li_4Ti_5O_{12}$ and $Li_7Ti_5O_{12}$ phase using first-principle calculations.[108,124–132] Only Li et al.[130,132] addressed the intermediate charge states, but as mentioned previously, they did not consider the effect of a heterogeneous mixture of phases on the optical spectrum. Interestingly, the band-gap for $Li_4Ti_5O_{12}$, calculated in the above-mentioned studies, varies from 2 eV to 4.2 eV. The discrepancy is less in the

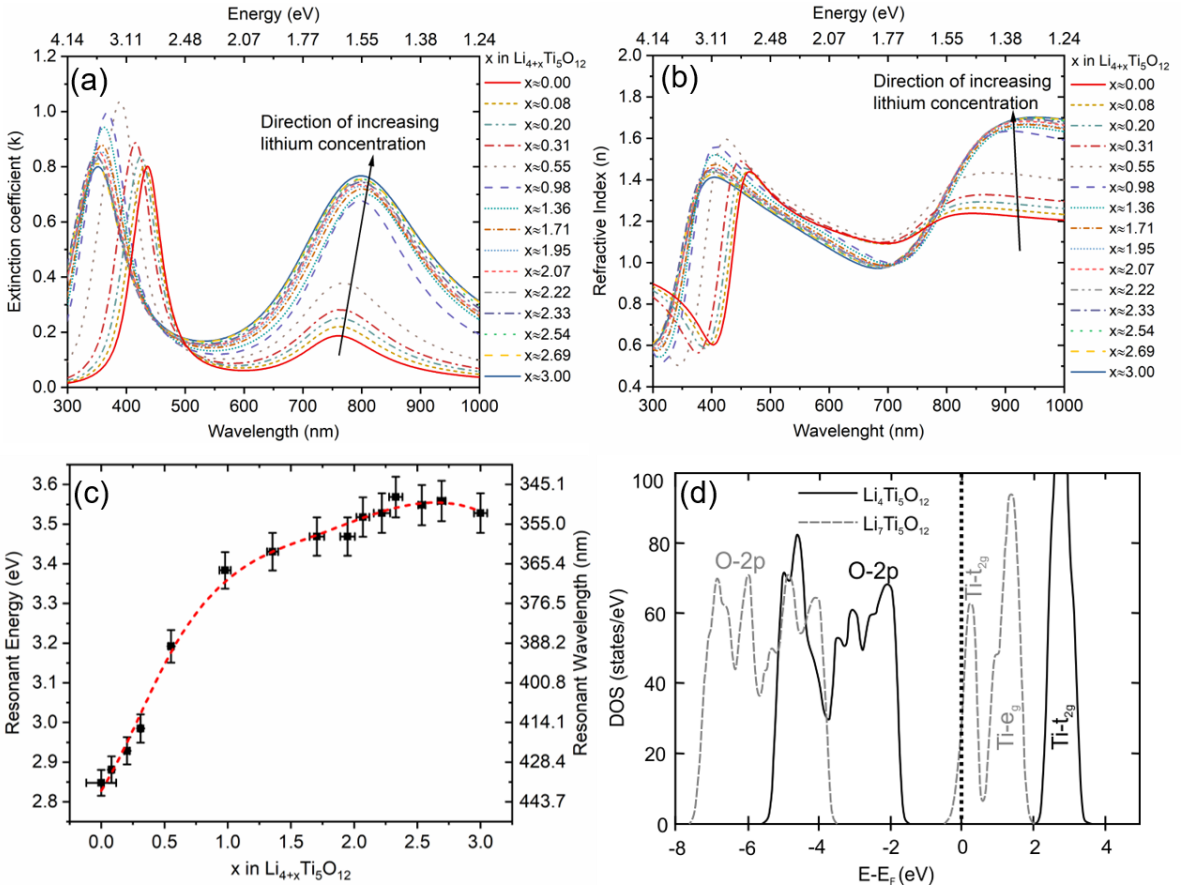

***Figure 4-6**: (a)The extinction coefficient and (b) the real part of the CRI as extracted from the model traces shown in Figure 4-5 (b); (c) change of the first resonance (higher energy, corresponding to the first maxima in (a)) with the state of charge in the LTO electrode, the red dashed line represents a cubic spline interpolation of the measurement points; (d) total density of states of $Li_4Ti_5O_{12}$ and $Li_7Ti_5O_{12}$[129].E2*

experimentally determined band gaps which are stated between 2.95 eV to 3.8 eV.[144–150] Exemplary band structure of $Li_4Ti_5O_{12}$ (solid black lines) and $Li_7Ti_5O_{12}$ (dashed grey lines) is shown in Figure 4-6(d), which is taken from the work of Sarantuya et al.[129]. For the $Li_7Ti_5O_{12}$ phase, the Fermi level (black dotted) falls into the partially filled Ti-t_{2g} band thereby making this phase a metallic conductor. Whereas, the $Li_4Ti_5O_{12}$ phase shows an insulating behavior with the band-gap of 3.9 eV.

In Figure 4-6(a), for all intercalation states $0 < x < 3$ two absorption maxima are seen which should correspond to dominating electronic excitations. For $x = 3$ ($Li_7Ti_5O_{12}$, blue curve), the two resonances are observed at 3.52 eV (352 nm) and at 1.55 eV (800 nm). Now, from the band structure of the $Li_7Ti_5O_{12}$ phase (dashed grey curve in Figure 4-6(d)) the corresponding dominant excitations could be the transitions from the filled O-2p band to the empty Ti-t_{2g} states ($\Delta E \approx 3.7$ eV) and from the filled Ti-t_{2g} states to the empty Ti-e_g ($\Delta E \approx 1.6$ eV). This higher energy transition from the O-2p to the Ti-t_{2g} states has also been calculated theoretically, corresponding to an energy of 3.44 eV (see reference [128]). Regarding the lower energy transition (i.e. 1.55 eV), apart from a transition mentioned above (i.e., from the filled Ti-t_{2g} states to empty Ti-e_g states, $\Delta E \approx 1.6$ eV), the only other possibility is an intra-band transition within the Ti-t_{2g} band. But these intra-band transitions would correspond to a significantly lower energy in the IR range which has not been evaluated here. Hence, it can be concluded that in the discussed wavelength range (300 nm-1000 nm) two electronic transitions exist, the one at the higher energy corresponding to a transition from O-2p state to empty Ti-t_{2g} states and the one at the lower energy corresponds to the electronic transition from the filled Ti-t_{2g} states to the empty Ti-e_g states. The corresponding real part of the CRI for the $Li_7Ti_5O_{12}$ phase is shown in Figure 4-6(b) ($x = 3$, blue curve). To our knowledge, no experimental data on the dispersion curve for the $Li_7Ti_5O_{12}$ phase has been previously published. Hence, the new data can only be compared to a theoretically predicted CRI by Liu et al.[128]. The principal shape of the real part of the CRI is very

similar, but the quantitative values are different, for instance at λ=450 nm Liu et al. calculated the refractive index to 2.17 whereas the measurement and its evaluation in this work derive 1.33 and at λ = 995 nm the theoretical study reported a value of 1.38, whereas here it is measured to be 1.7. However, such discrepancies are commonly encountered between the computationally and experimentally determined values. This is due to the unavoidable fact that in a real system, structural defects such as vacancies, grain boundaries, or impurities exist and will probably affect the reflectance spectrum. Whereas, in the theoretical work to our knowledge, ideal lattice structures are assumed (besides the general difficulties in the quantitative accuracy of band structure calculations).

For $x = 0$ ($Li_4Ti_5O_{12}$, the red curve in Figure 4-6(a)), a strong resonance peak at 2.8 eV (437 nm) is obtained, this agrees well with the reported band-gap (as mentioned above), hence this resonance can be assigned to an electronic transition from O-2p to Ti-t_{2g}. Additionally, a small peak at the energy corresponding to 1.63 eV is also observed. This could be due to some available unoccupied states from the remaining lithium-rich phase (as the material has been cycled before the measurement). The corresponding real part of the CRI is shown in Figure 4-6(b) (in red). The real part of the CRI becomes less than unity for λ < 450 nm, which is due to the presence of a resonance in that region. At λ = 550 nm, a refractive index of 1.22 is obtained, which is comparable to reports by Özen et al.[146] and Yudar et al.[144] who reported a value of 1.45-1.51. The remaining difference could be due to the model used for evaluation (in the case of Yudar et al.[144]) or due to the different surface morphology of the samples (in the case of Özen et al.[146] as they used spectroscopic ellipsometry which is known to be quite surface-sensitive[151]). A quite contrasting measurement of $Li_4Ti_5O_{12}$ was reported by Zhao et al. with a value of 2.2 at 550 nm. This might be due to the very low layer thickness (86 nm) used by them, which increases the impact of surface roughness when measured with spectroscopic ellipsometry.[151]

Furthermore, in Figure 4-6(a), as lithium is removed (i.e. *x* is decreasing from 3 to 0) the reflectance of the peak at lower energy (or larger wavelength) gradually decreases. This is due to the removal of the lithium-rich phase having a high absorption in the red wavelength range as described above. Interestingly, the peak at the higher energy is continuously shifting towards even higher energy when lithium is removed. This is shown more clearly in Figure 4-6(c) by plotting the positions of the peak maxima versus the Li content (*x*). This is naturally explained by the stabilization of the valence band (shifts to lower energy) with lithium intercalation shown in Figure 4-6(d). According to Liu et al.,[128] this stabilization amounts to 0.5 eV which matches strikingly well with the shift observed in our experiments shown in Figure 4-6(c) that amounts to 0.65 eV.

4.3.2 Phase transformation in thin-film LTO

Besides the evaluation of optical constants, the knowledge of which is inherently needed to develop any kind of optical device, the electrochromic feature can be used to better elucidate the ion migration. This section will discuss a possible way to use the electrochromic feature to better understand phase propagation using the continuous concentration dependence of the complex dielectric function (CDF). With the evaluated CRI, the complex dielectric function (CDF) can be calculated using Equation 4-1.

$$\varepsilon_\gamma = \varepsilon_\gamma' - i\varepsilon_\gamma'' = (n_\gamma - ik_\gamma)^2 \qquad 4\text{-}1$$

As has been mentioned in the introduction, the existence of two phases has been proved but there is still a debate about the movement of the phase boundary or how the phase grows during an actual battery testing or de-/intercalation of lithium.[131] The CDF can be utilized to understand this transformation as the two phases exhibit a huge difference in terms of CRI, or conclusively in CDF as well, as can be seen in Figure 4-6(a) and (b).

Chain and Byrne[152] reported that in a two-phase system, the effective dielectric function of a material depends on the detailed microstructure, more specifically

the geometric arrangement of the two phases, of the system. This is expressed for two extreme cases by Equation 4-2 and 4-3

$$\varepsilon_{eff} = f_{Li4Ti5O12} \cdot \varepsilon_{Li4Ti5O12} + f_{Li7Ti5O12} \cdot \varepsilon_{Li7Ti5O12} \quad 4\text{-}2$$

$$\frac{1}{\varepsilon_{eff}} = \frac{f_{Li4Ti5O12}}{\varepsilon_{Li4Ti5O12}} + \frac{f_{Li7Ti5O12}}{\varepsilon_{Li7Ti5O12}} \quad 4\text{-}3$$

The variables ε_{eff}, $\varepsilon_{Li4Ti5O12}$, $\varepsilon_{Li7Ti5O12}$ represent the effective CDF of the layer and the CDF of the $Li_4Ti_5O_{12}$ phase and $Li_7Ti_5O_{12}$ phase, respectively; $f_{Li4TI5O12}$ and $f_{Li7TI5O12}$ represent the volume fractions of the $Li_4Ti_5O_{12}$ and $Li_7Ti_5O_{12}$ phases. These equations represent the mixture rules for a two-phase heterogeneous microstructure. Equation 4-2 describes the limiting case of a layered microstructure with layers aligned parallel to the substrate, while Equation 4-3 describes the effective CDF for a columnar dual-phase system when the columns of the two phases are aligned perpendicular to the substrate.

The dielectric constant represents the ability of a material to be polarized. This can be treated in an analogous way to a capacitor storing charge. Now, considering that the light is incident on the sample normally. The electric field of the incident light will be parallel to the substrate, and if the two phases are aligned parallel to the substrate or parallel to the electric field, it would give maximum polarization. This is analogous to a parallel capacitor circuit and in this case, the effective capacitance is the summation of each capacitance i.e., similar to Equation 4-2. In the other extreme case, when the two phases are aligned perpendicular to the substrate, they are also perpendicular to the electric field. In this case, it will result in minimum polarization which is analogous to a series connection of capacitors, for which the inverse of effective capacitance equals the summation of the inverse of individual capacitance, similar to Equation 4-3.

When Equation 4-1 and 4-2 are combined to represent the real part of the dielectric function as a function of the imaginary part at a fixed wavelength, i.e. by eliminating the term describing the phase fraction, a linear behavior between the

real vs imaginary part is predicted under the variation of the phase fraction, as shown by a black dashed line in Figure 4-7(a). By contrast, combining Equation 4-1 and 4-3 yields a curved line (part of a hyperbola), as indicated by a brown dashed line in the same figure. The shown curves are calculated using $\varepsilon_{Li4Ti5O12}$ and $\varepsilon_{Li7Ti5O12}$ at the selected wavelength of $\lambda = 951$ nm. Fascinatingly, when the complex dielectric constants from the presented measurements (for λ=951 nm, at varying degrees of intercalation) are plotted on the same graph (shown by hollow circles), they closely follow the green dashed line. This indicates a columnar

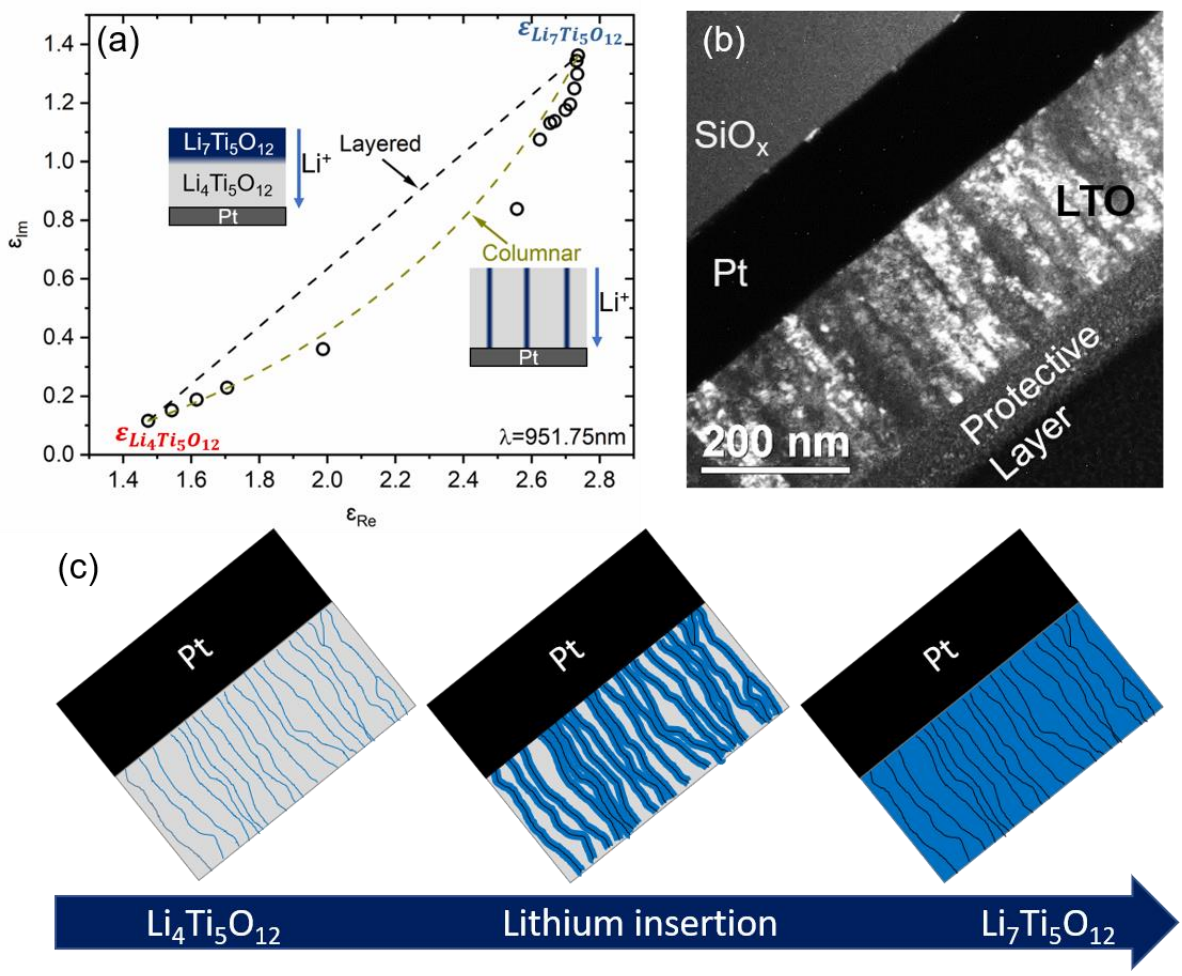

***Figure 4-7**: (a) Real versus imaginary part of the complex dielectric function at λ=951.67 nm for different charge states, extracted using Equation 3. The dashed lines correspond to the layer and columnar growth as per Equations 4 and 5, respectively. (b) Dark Field TEM micrograph revealing the columnar microstructure of the annealed LTO layer. (c) Proposed phase transformation mechanism describing the nucleation of the lithium-rich phase along the grain boundaries followed by growth of this phase towards the grain interior.*[E2]

arrangement of the phases and rejects the naively expected bilayer structure when Li^+ is intercalated from the top of the layer's surface. To better understand this behavior, a dark field TEM (DF-TEM) of the layer is shown in Figure 4-7(b). The figure shows that the grains are aligned perpendicular to the substrate due to the columnar growth during the thin-film deposition. Taking into account the results of Figure 4-7(a) and (b), a reaction mechanism can be proposed as in Figure 4-7(c). The schematic on the left has been drawn by overlapping it to the DF-TEM. Most of the grain boundaries are aligned perpendicular to the substrate and they can facilitate a faster diffusion of lithium.[41,153] This fast lithium enrichment causes the nucleation of the lithium-rich phase along the grain boundaries. As mentioned before, the lithium-rich phase exhibits a metallic behavior. Therefore, the segregation at the grain boundaries will increase the electronic conductivity significantly across the thin film and so would explain the fast dis-/charge ability of the reported thin films. Subsequently, as more lithium is inserted, the reaction front would propagate towards the grain's interior i.e. growing perpendicular to the grain boundaries.

The Electrochemical measurements by Wang et al.[41] support this reaction mechanism. They reported a higher diffusion coefficient of lithium for LTO particles containing more grain boundaries and this was attributed to a faster grain boundary diffusion. By contrast, Kim et al.[154] and Verde et al.[131] suggested different routes. Kim et al. suggested a model to which the lithium-rich phase starts to precipitate near the current collector. Therefore, the lithium-rich phase grows (during insertion) in a layer-like geometry, which is contradicted by the present experimental observation. Verde et al. reported that a transition from $Li_4Ti_5O_{12}$ to $Li_7Ti_5O_{12}$ takes place via *percolation channels* connecting the current collector and the electrolyte, which in consequence would be very close to our model. However, both the study of Kim et al. and the study of Verde et al. deal with a different sample geometry, i.e. with powders and porous thin-film that cannot be compared to the dense thin-film samples used in this study. The only alternate possibility to

produce a columnar heterogeneous phase structure would be the localized formation of $Li_7Ti_5O_{12}$ at the surface (in contact with the electrolyte) in some selected grains and from there the phase boundary could locally propagate deeper into the layer. But presumably, this option is not sound due to the observed very small grain widths. Given the small grain width as seen in Figure 4-7(b) an effective layer of $Li_7Ti_5O_{12}$ would be formed very soon after the beginning of the transformation, thus an effective bilayer geometry would result in contradiction to the presented optical data.

4.4 Summary

A detailed analysis of the optical reflectance spectrum of thin films of spinel structured $Li_4Ti_5O_{12}$ and its change upon lithium intercalation, resulting from the formation of a rock salt-type $Li_7Ti_5O_{12}$, has been performed in the wavelength range from 425 nm to 1000 nm. A reversible electrochromic behavior has been confirmed and the effect of the state of charge on the reflectance spectrum has been demonstrated. The successful modeling of the reflectance spectrum using a two-oscillator Clausius–Mossotti model for many different intercalation states has been reported. The complex refractive index of $Li_7Ti_5O_{12}$ has been measured for the first time. The quantitative explanation of the complex refractive index based on band theory reveals that $Li_7Ti_5O_{12}$ shows two strong resonances corresponding to electronic transitions from O-2p to empty Ti-t_{2g} and from filled Ti-t_{2g} to empty Ti-e_g, whereas $Li_4Ti_5O_{12}$ reveals only one strong resonance corresponding to an electronic transition from O-2p to Ti-t_{2g} (i.e. across the bandgap). Finally, using the complex dielectric function and considering the mixing rules for different heterogeneous phase arrangements, the probable transport mechanism of phase transformation in LTO thin films has been identified. The fast lithium migration through the grain boundaries enables the segregation of a conductive lithium-rich phase in them, thereby increasing the electronic conductivity throughout the thin-film electrode. Hence, this phase distribution mechanism explains the fast dis-/charge capability of thin films of $Li_4Ti_5O_{12}$.

5 Lithium Migration and Phase Transformation in $Li_{4/3+x}Ti_{5/3}O_4$

The previous chapter dealt with the electrochromic behavior and the phase transformation mechanism, elucidated ex-situ, in LTO thin-film of a few hundred nanometers. But the kinetics of this phase transformation was not evaluated. The current chapter will precisely deal with the understanding of the lithium diffusion and the movement of the phase-boundary in LTO, in a micrometer length scale. As mentioned previously, during the phase transformation to $Li_{7/3}Ti_{5/3}O_4$ phase upon lithium insertion, the atoms of lithium at the 8a sites (tetrahedral position) shift to the 16c position (octahedral position), and the insertion of eight additional lithium atoms takes place in vacant 16c position thus filling up all of the octahedral sites.[10,108] This reordering and insertion of lithium atoms, is accompanied by a huge change in the electronic[108] and the optical properties[E2] as is also evident from the previous chapter. However structurally, there is a mere 0.2% change in the volume of the unit-cell, hence the term *zero-strain* phase transformation was coined for it[10].

The fast dis-/charge ability of LTO (achievable by surface modification and reducing particulate size[104]) must be governed by the transport properties of lithium and the kinetics of phase propagation in the electrode, or the electrode particle itself, provided the electronic conductivity is sufficient. However, several studies using nuclear magnetic resonance (NMR)[40,68,155–157] and a few using first principle calculations[158,159] have revealed a high energy barrier (or slow diffusion) for lithium migration in the two phases (strictly speaking for the stoichiometric phase compositions of $Li_{7/3}Ti_{5/3}O_4$ and $Li_{4/3}Ti_{5/3}O_4$), making it difficult to understand the high-rate performance achieved in this material. On the other hand, Ganapathy et al.[62] using first-principle calculations reported a fast Li migration across the phase boundary during the phase transformation to explain the fast dis-/charging ability

of this material. Such fast transport across the interface, formed at the phase boundary, is in contrast to some silicon-based[47–49] and hydrogen-based systems[50,51] where the interface is known to hinder the migration of atoms. The hindrance at the phase boundary leads to a deviation from a normal diffusion-controlled parabolic growth to a slower interface-controlled linear growth of the silicide or hydride phase in the initial stages of atomic transport. The significance of phase boundary, if any, on the kinetics of lithium diffusion and the resulting phase propagation inside of an electrode has not yet been discussed. Presumably due to the assumption of a diffusion-controlled parabolic growth.

This chapter aims at unraveling the kinetics of lithium diffusion and the subsequent phase propagation in $Li_{4/3+x}Ti_{5/3}O_4$ and its temperature dependence. This is achieved by using an innovative technique that exploits the huge change in the optical properties of LTO upon lithium insertion, i.e. the electrochromic (EC) character of LTO, especially in the red wavelength region of the visible spectrum.[E2] The methodology enables us to 'literally' observe the propagating $Li_{7/3}Ti_{5/3}O_4$ phase-front in the electrode. Since the investigated lateral diffusion lengths are in the micrometer range, the results are inherently valid for a commercial battery application (which deal with particles of sizes close to a few micrometers or less). The methodology developed here and the results discussed in this chapter were recently submitted to a journal for publication.[E3] The technique can also be used to characterize other battery materials as they commonly show EC character.[E1,160,161] In the following, the Li-poor spinel phase is denoted as the α-phase and the Li-rich rock salt phase as the γ–phase.

5.1 Experimental realization

5.1.1 Thin-film preparation.

The same methodology as in the previous chapter was used to prepare the thin films. Only this time, the layers were annealed at 550°C in vacuum for two hours. The time is increased to two hours to coarsen the grains, so as to achieve a clear

two-phase reaction, as observable from the electrochemical measurements (see section 5.2.2).

5.1.2 Electrochromic Imaging

This imaging methodology is developed to study the lateral diffusion of lithium and the resulting phase transformation in thin-film electrodes. Figure 5-1 (a) and (b) shows the schematics of the sample and the setup used, respectively. A small area of the sample is coated by an optically transparent, but lithium blocking layer (Kayaku Advanced Materials SU-8 photo/e-beam resist), structured with the help of an e-beam lithography process, described in the subsequent section. The electrochemical cell, shown in Figure 5-1(b), consists of a three-electrode setup controlled by a Gamry Interface 1000 potentiostat. Two lithium foils act as reference and counter electrodes. Hence, all the potentials mentioned in the chapter are stated with respect to lithium and are comparable to those in chapter 4. A platinum metallization provides the electrical contact to the LTO electrode which is acting as the working electrode. 1 M $LiClO_4$ in ethylene carbonate (EC) and

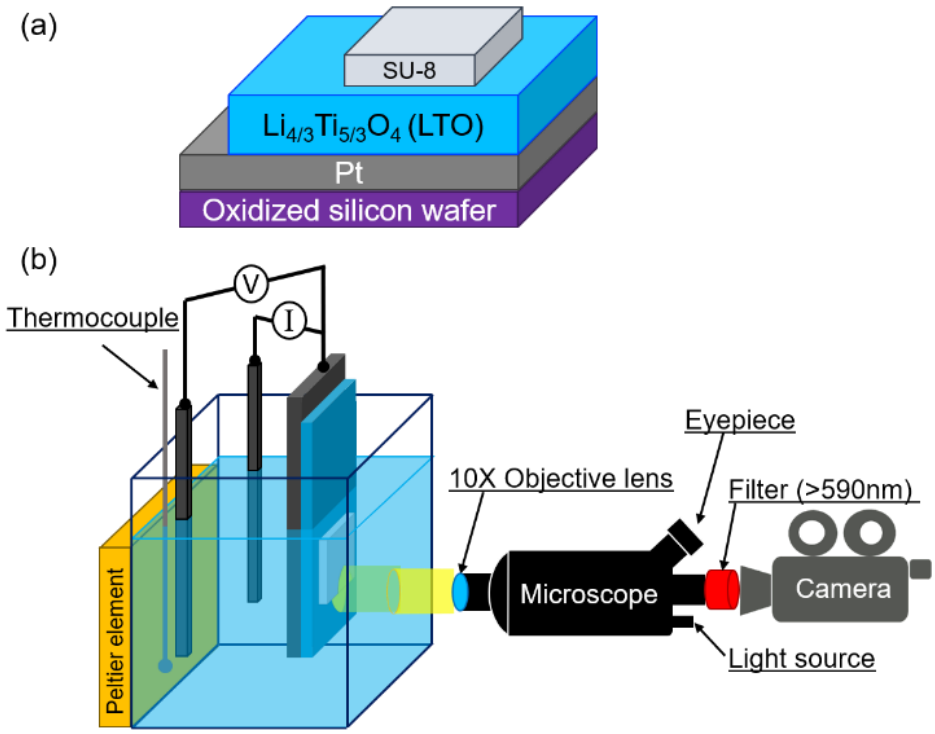

***Figure 5-1**: (a) Schematic of the electrode sample coated with e-beam resist SU-8. (b) Setup for electrochromic imaging with simultaneous electrochemical de-/intercalation of lithium ions in a three-electrode battery setup.[E3]*

dimethyl carbonate (DMC) (1:1 ratio by mass) is used as the liquid electrolyte. The electrochemical cell is assembled in an argon-filled glovebox and is subsequently sealed. The cell has flat faces and is made of optical grade glass (Hellma Analytics 700.016-OG). It is held by a custom-build holder (made from Polyether ether ketone, PEEK) which has two Peltier elements (from Adaptive, manufacture part number ET-031-10-13-RS) placed on two opposite sides of the cell. The Peltier elements are used for heating the cell. Additionally, a K-type thermocouple is inserted in the electrochemical cell to monitor the temperature throughout the measurement. A Mitutoyo microscope unit, with a 10X objective lens (Mitutoyo Plan Apo Infinity corrected long WD objective), is fixed horizontally to focus on the interface of the bare LTO and SU-8 coated LTO. A color filter is placed prior to the camera (Thorlabs DCC1645C) allowing the light with a wavelength greater than 590 nm to pass. The choice of the filter is based on the finding of the previous chapter in which it was shown that the $Li_{7/3}Ti_{5/3}O_4$ phase has a dominant optical absorption in the red wavelength.[E2] To study the diffusion of lithium underneath the barrier layer, a constant voltage of 1 V is applied at time t=0 s and is maintained throughout the experiment; simultaneously a camera records images at regular time intervals. The small difference in grey level due to the SU-8 layer, and variation in the lamp intensity, during the course of the experiment, is corrected by a multiplication factor and an offset to match the intensity of the fully intercalated $Li_{7/3}Ti_{5/3}O_4$ phase in the uncovered SU-8 and the fully de-lithiated LTO phase underneath the SU-8. Furthermore, the drift in the measurement was corrected by aligning the interface (between the bare LTO and SU-8 coated LTO) for all the analyzed frames. Lithiation was studied at three temperatures i.e., 22°C, 45°C, and 55°C.

5.1.3 Lithography

After the required annealing of the active material, electron (e-) beam lithography is used to coat an area with a lithium blocking layer. Kayaku Advanced Materials SU-8 2000.5 photo/e-beam resist (a negative photoresist) was used as a blocking

layer, due to its inability to dissolve in organic solvents (present in the battery electrolyte) and because of its crosslinking nature (upon exposure to e-beam) which will probably help in effectively blocking the lithium ions. The schematics of the samples are given in Figure 5-1 (a).

The layer of SU-8 2000.5 was spin-coated at 1000 rpm for 30 s. Followed by a prebake at 95°C for 2 min. Subsequently, the sample is transferred into the SEM (FEI Scios Dual-beam microscope). A selected area (600 × 550 μm^2) large enough to consider the diffusion in the field of view of the camera as one dimensional and semi-infinite, is exposed with a dose of 1.5 $\mu C\ cm^{-2}$ at 30 kV and using a current of 3.1 pA with a pitch of ca. 155 nm. Subsequently, the sample was post-baked at 95°C for 4 min followed by developing it with propylene glycol monomethyl ether acetate (or PGMEA) from Sigma-Aldrich (CAS number: 108-65-6). The sample is rinsed with iso-propanol and dried in air. Finally, a hard-bake is executed at 150°C for 30 min in air to further crosslink the SU-8 photoresist.

To study the effect of the finite size of the electrode on the growth kinetics, circular patterns were also coated, on a few samples, with diameters of 40, 20, 10, and 5 µm. The lithography used the same methodology, except this time the pitch between each illuminated pixel was 13 nm. The quality/morphology of the lithography has been verified by an FEI Quanta SEM. The microstructure of the layers, with and without the SU-8, has been determined by TEM using a Philips CM200-FEG instrument.

5.1.4 Electrochemical measurement

The cyclic stability and rate performance charging measurements used the same three-electrode setup, controlled with Bio-Logic VSP 300 potentiostat. Only in this case, the LTO electrodes were not coated with a SU-8 barrier layer (i.e., the samples were measured directly after the vacuum annealing).

The specific volumetric capacity of the thin-film electrodes is determined from the absolute capacity (calculated from the integrated current from the

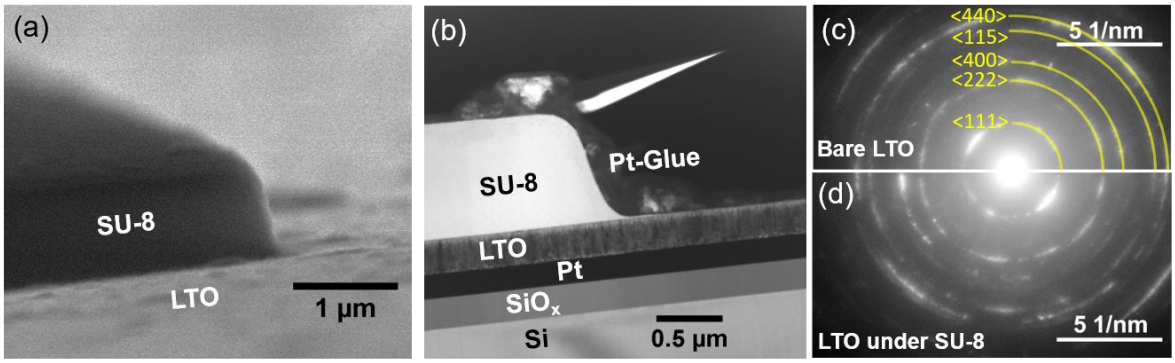

***Figure 5-2**: (a) SEM image of SU-8 film coated on LTO electrode; (b) TEM image of the multilayer stack with the SU-8 coating; (c) diffraction pattern of the LTO layer without the SU-8 coating; (d) LTO layer underneath the SU-8 coating.*[E3]

chronopotentiometry measurement) and the volume of the electrode, determined by the area exposed to the electrolyte and the thickness of the film.

5.2 Results

5.2.1 Structure and morphology

Figure 5-2 (a) shows the Scanning Electron Microscope (SEM) image of a corner of the coated SU-8 barrier on top of the LTO electrode. A sharp interface between the SU-8 and LTO can be observed. To have a closer look at the coated barrier layer and on the sputtered LTO thin-film, a cross-section of the multilayered sample is shown in the bright-field TEM image in Figure 5-2 (b). The thickness and the edge sharpness of the blocking SU-8 layer are ca. 860 nm and ca. 350 nm, respectively. The sharpness is significantly smaller than the resolution of 1 µm of the 10X objective lens used in this study. Furthermore, the LTO layer shows columnar grains. Figure 5-2 (c) and (d) shows the selected area electron diffraction (SAED) pattern from the LTO layer, away and underneath the SU-8 blocking layer, respectively. There is practically no change in the crystal structure of the LTO electrode, hence it can be concluded that the lithography process has no detrimental effects on the crystal structure of the LTO electrode.

5.2.2 Cyclic stability and Fast dis-/charging

Figure 5-3 (a) shows the cyclic stability of the LTO electrode when measured at ca. 1C rate. The capacity of the electrode at the end of the 2nd cycle was

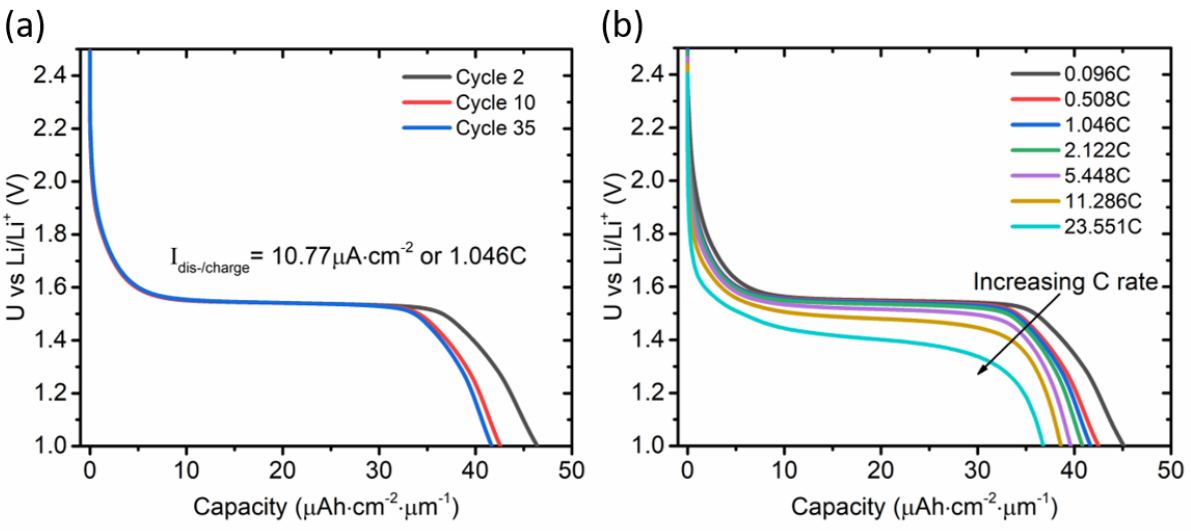

Figure 5-3: *(a) Cyclic stability of LTO electrode during lithium intercalation. (b) Rate capability of LTO electrode (intercalation step) at varying scan rates.*[E3]

46.42 µAh·cm^{-2}·µm^{-1} which decreases to 42.58 µAh·cm^{-2}·µm^{-1}, a loss of 8.3% in the first 10 cycles. However, at the end of the 35th cycle, the capacity was 41.68 µAh·cm^{-2}·µm^{-1} i.e., a further decrease of mere 2.1%. Furthermore, the figure shows a flat plateau at 1.55 V vs Li/Li$^+$, characteristic of the LTO electrode[10]. This zero-sloped plateau in a galvanostatic measurement is a typical feature of the electrodes undergoing phase transformation. Figure 5-3 (b) shows the fast-charging performance of the LTO electrode. The capacity of the LTO electrode, when measured at 0.096C (i.e., slightly more than 10hr to charge or discharge), is 45.12 µAh·cm^{-2}·µm^{-1} and it decreases to 36.79 µAh·cm^{-2}·µm^{-1} (a decrease of just 18%) when measured at 23.55C (or charging in 153 s).

5.2.3 Diffusion of Lithium

As mentioned before, the fast dis-/charging ability of the LTO must relate to the transport property of lithium. Hence, to probe this property, electrochromic imaging is executed. Figure 5-4 shows the diffusion of lithium at room temperature, 22°C. As seen in Figure 5-4 (a), the intercalation process is initiated at time t = 0 s by applying a voltage step (black line) from 2.72 V (the open-circuit voltage, OCV of the electrode) to 1 V vs Li/Li$^+$. The respective current response is shown by the red dotted line. The schematic in the inset of Figure 5-4 (a) shows the area recorded by the optical microscope by a yellow circle where the light from the 10X objective

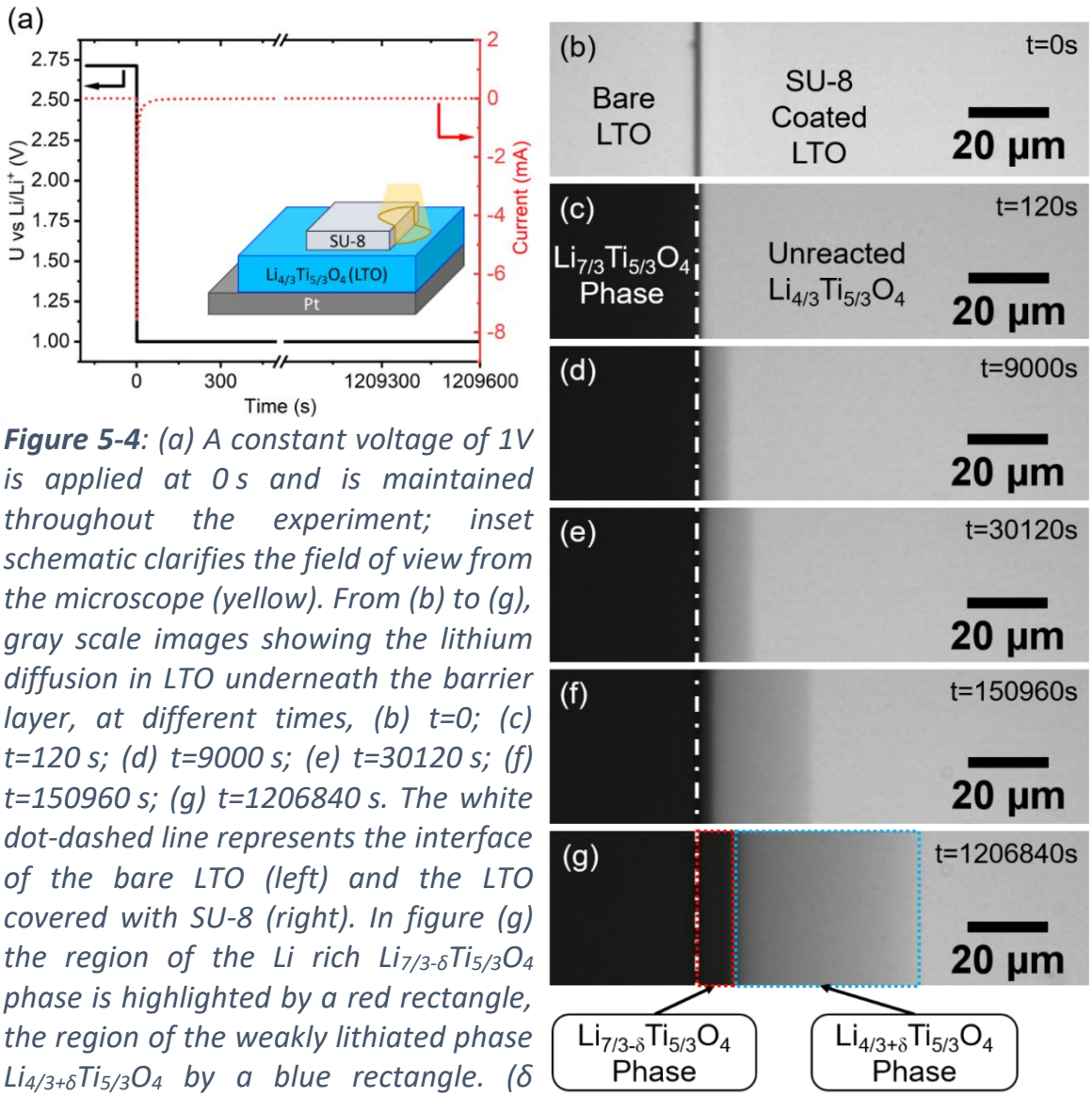

***Figure 5-4**: (a) A constant voltage of 1V is applied at 0 s and is maintained throughout the experiment; inset schematic clarifies the field of view from the microscope (yellow). From (b) to (g), gray scale images showing the lithium diffusion in LTO underneath the barrier layer, at different times, (b) t=0; (c) t=120 s; (d) t=9000 s; (e) t=30120 s; (f) t=150960 s; (g) t=1206840 s. The white dot-dashed line represents the interface of the bare LTO (left) and the LTO covered with SU-8 (right). In figure (g) the region of the Li rich $Li_{7/3-\delta}Ti_{5/3}O_4$ phase is highlighted by a red rectangle, the region of the weakly lithiated phase $Li_{4/3+\delta}Ti_{5/3}O_4$ by a blue rectangle. (δ represents a small change in concentration.) Remaining light grey at the right side represents still completely delithiated $Li_{4/3}Ti_{5/3}O_4$ phase.*[E3]

lens is incident. A top view of the LTO electrode coated with the SU-8 barrier, as seen by the optical microscope, is shown in Figure 5-4 (b). The image was taken just before the voltage step was commenced (at t=0 s). Due to the transparent nature of the SU-8, there is practically no difference in the intensity of the LTO coated with SU-8 and the bare LTO, and only the interface/edge between the uncoated LTO and the blocked LTO layer is visible as a dark line caused by local scattering. The position of this edge has been highlighted by a white dashed-dotted line in Figure 5-4 (c) to (g). Figure 5-4 (c) shows the image taken 120 s after the

applied voltage step. The uncoated part of the LTO has completely turned black i.e., absorbing all the red-light incident on it. This is due to the phase transformation to the completely lithiated $Li_{7/3}Ti_{5/3}O_4$ phase which is known to significantly absorb the red light[E2]. As intended, the blocked part has not transformed at all. After 9000 s (see Figure 5-4 (d)), a dark gray band has formed ahead of the edge/interface (between the blocked LTO layer and bare LTO), suggesting that lithium has diffused laterally into the LTO layer. At time t=30120 s (Figure 5-4 (e)), the dark gray band has progressed even further. In Figure 5-4 (f) at time t=150960 s, an appearance of a black phase underneath the SU-8 layer becomes noticeable. This black phase has even grown further as time progresses to t=1206840 s (13 days, 23 hr, and 14 min) in Figure 5-4 (g). The measurement was stopped after two weeks.

To evaluate the above-obtained images in terms of lithium concentration and phase evaluation, a calibration measurement was executed as shown in Figure 5-5. For this, a similar sample (with SU-8 coating) was intercalated galvanostatically at about 0.1C, the voltage profile of the LTO electrode is shown in Figure 5-5 (a) by a black solid line. Simultaneously, the intensities were recorded at regular intervals from the area not covered by SU-8. These intensities are converted into relative intensity by assuming the intensity of light reflected from the pure $Li_{4/3}Ti_{5/3}O_4$ phase is 1 and that from pure $Li_{7/3}Ti_{5/3}O_4$ phase is 0, and accordingly at different charge states the relative intensities are obtained and are shown by red hollow points in Figure 5-5 (a). The apparent continuous transition of the intensity in the two-phase region is due to an overlap of both phases in the beam direction. Subsequently, a calibration curve is obtained by fitting these relative intensities as depicted by a dotted line in Figure 5-5 (b). The equation of the curve is noted in the figure. Utilizing this calibration curve, the relative intensity profiles obtained during the diffusion experiment, as shown in Figure 5-5 (c), are converted to the concentration profiles in Figure 5-5 (d). From Figure 5-5 (d), a clear phase boundary resulting from the sharp jump of lithium concentration between x = 0.8 to x = 0.2

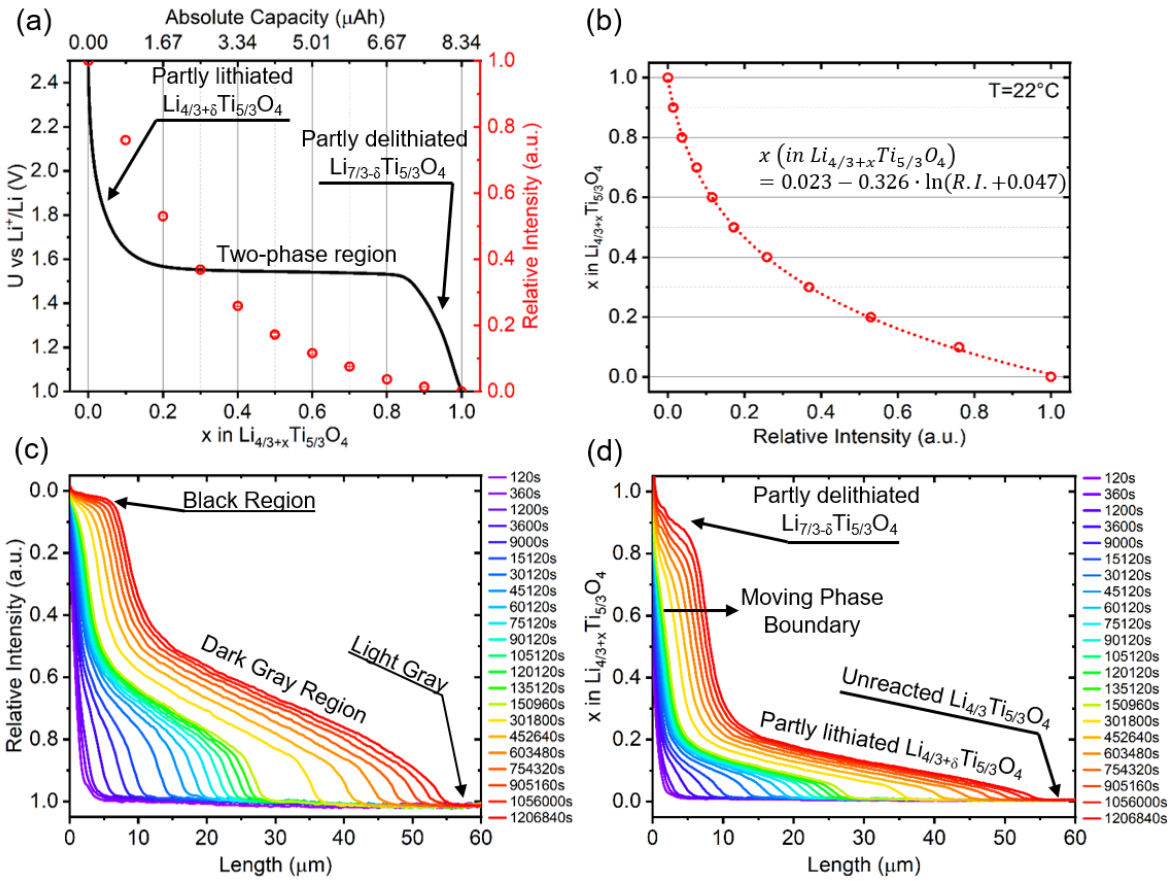

***Figure 5-5**: (a) Evolution of voltage profile as a function of lithium concentration (black solid) and the corresponding relative intensity (red circles); (b) relative intensity vs. Lithium concentration obtained experimentally as shown by hollow red circles and a corresponding fitted curve shown by the red dashed curve. The curve represents a logarithmic decay curve with the equation given in the legend. (c) Relative Intensity profile at different times; (d) Concentration profiles derived from the relative intensity profiles, with the help of the curve as shown in (b).[E3]*

(where *x* is the amount of lithium in $Li_{4/3+x}Ti_{5/3}O_4$) is visible especially for the longest time step (i.e., 1206840 s). Now, correlating Figure 5-4 (g) with Figure 5-5 (d), the concentration in the different gray-scale regions can be identified. In Figure 5-4 (g), moving from left to right, the black phase before the edge/interface (between the bare LTO and SU-8 coated LTO) is the fully intercalated $Li_{7/3}Ti_{5/3}O_4$ phase. The black stripe directly to the right of the edge of the protective coating represents the partially delithiated $Li_{7/3-\delta}Ti_{5/3}O_4$ phase (or Li-rich phase). To the right of this black stripe, the dark gray band belongs to the partially lithiated $Li_{4/3+\delta}Ti_{5/3}O_4$ phase (or Li-poor phase), and finally, the light gray phase to the far-right side represents the unreacted $Li_{4/3}Ti_{5/3}O_4$ phase. A detailed point to note, in the concentration profiles

of Figure 5-5 (d), at the position of 0 µm, the concentration even increases beyond the maximum of x = 1. This is an artifact owing to the additional scattering of the edge of the SU-8 coating.

For diffusional transport with a constant diffusion coefficient, the concentration profile of the diffusor should have a profile corresponding to an error function (for semi-infinite diffusion from a constant source). In contrast, the concentration profile of lithium in the Li-poor region falls quite abruptly to the completely unreacted $Li_{4/3}Ti_{5/3}O_4$ phase, indicating a huge dependence of the diffusion coefficient on the concentration, in this concentration range. This agrees well with the literature[40,41,68,155–158] which reports a very slow diffusion in the unreacted $Li_{4/3}Ti_{5/3}O_4$ phase that increases drastically with a small increase of lithium content. In a steady-state evolution of the concentration profile, a low diffusion coefficient in a certain range of composition has to be compensated by a stronger concentration gradient which provokes a pronounced contrast between the initial fully delithiated $Li_{4/3}Ti_{5/3}O_4$ and the partially lithiated $Li_{4/3+\delta}Ti_{5/3}O_4$, although thermodynamically, both belong to the same phase.

The continuous gray-shading in Figure 5-4 (d) to (g) has to be interpreted by Harrison's type A diffusion[162] i.e., the bulk diffusion and the grain boundary diffusion cannot be distinguished and the measured diffusion coefficient may have a contribution from the grain boundary transport. The discontinuous jump in the concentration profile between the black stripe and the dark grey region clearly confirms the existence of a two-phase reaction. The debated continuous solid-solution[106] is not consistent with these measurements.

5.2.4 Kinetics of the growth of the γ phase: linear to parabolic transition

Knowing the concentration profiles at different time intervals enables accurate characterization of the kinetics of lithium migration and the resulting phase transformation in the LTO electrode. Reactive diffusion has been intensively investigated in the case of the interdiffusion of metallic diffusion couples.[37] In the

case of a steady-state transport, parabolic growth (i.e. thickness proportional to the square root of time) of intermetallic reaction products is a common observation.[52,163] In the very early stages, however, a deviation towards linear kinetics (thickness proportional to time) is expected, although rarely experimentally proven in the reaction of metals. The respective kinetic coefficient for the linear growth, in particular, its temperature dependence and activation energy are widely unexplored. Significant linear regimes might be seen, if the reaction at the phase boundary requires a major reordering of the atomic arrangement at an interface particularly in the context to fast interstitial diffusion, for instance, with the growth of silicides[47–49] and hydrides[50,51]. Such interface-controlled transport results in slow linear growth of the intermetallic/hydride phase in the initial stages of atomic transport (see ref [45]) rather than a faster parabolic growth.[47,49] To allow for such linear growth, we describe the width of the Li-rich γ phase by:

$$t = \frac{c^{\gamma} - c^{\alpha}_{max}}{\kappa \cdot \left(c^{\gamma} - c^{\gamma}_{min}\right)}(w - w_0) + \frac{c^{\gamma}_{min} - c^{\alpha}_{max}}{2D^{\gamma}_{Li} \cdot \left(c^{\gamma} - c^{\gamma}_{min}\right)}(w^2 - {w_0}^2), \qquad 5\text{-}1$$

which is inspired by the work of Gösele and Tu[46], and Tomán et al.[45] and has already been derived in chapter 1 see section 1.3.2. The variable t denotes the time, c^{γ} the maximum concentration (atomic fraction of Li on the octahedral sites) of the Li-rich phase which equals 1, c^{γ}_{min} and c^{α}_{max} are the atomic fractions to both sides of the phase boundary i.e., on the Li-rich side c^{γ}_{min} = 0.85 and on the Li-poor side c^{α}_{max} = 0.15 (from Figure 5-5 (a)), κ is the "barrier" coefficient controlling the linear growth, w the width of the phase, w_0 a possible initial width (in our case, very close to zero) and D^{γ}_{Li} is the chemical diffusion coefficient of Li in the γ phase (in principle concentration-dependent but here averaged over the composition range of the phase in the sense of a Wagner integral[164]).

For quantification, the position of the interface between the two phases is defined at the concentration x = 0.7 in $Li_{4/3+x}Ti_{5/3}O_4$, where the gradient in the composition

is quite steep, hence the exact choice of the interface composition has negligible influence on the results. Figure 5-6(a) shows the evaluated widths of the Li-rich phase as a function of time at different temperatures. Consider the room temperature measurement (22°C, gray squares). It is evidently clear that the γ-phase starts to grow first proportional to time as marked by a gray dotted line with a slope of m_l=6.77×10^{-10} cm·s^{-1}. Only at a later time, it deviates from this linear growth and finally reaches the parabolic regime, as clearly demonstrated by a plot of the square of the width versus time (see Figure 5-6(b)), in which the late data points agree to a straight line with slope m_p=5.32×10^{-13} cm^2·s^{-1}. By using these

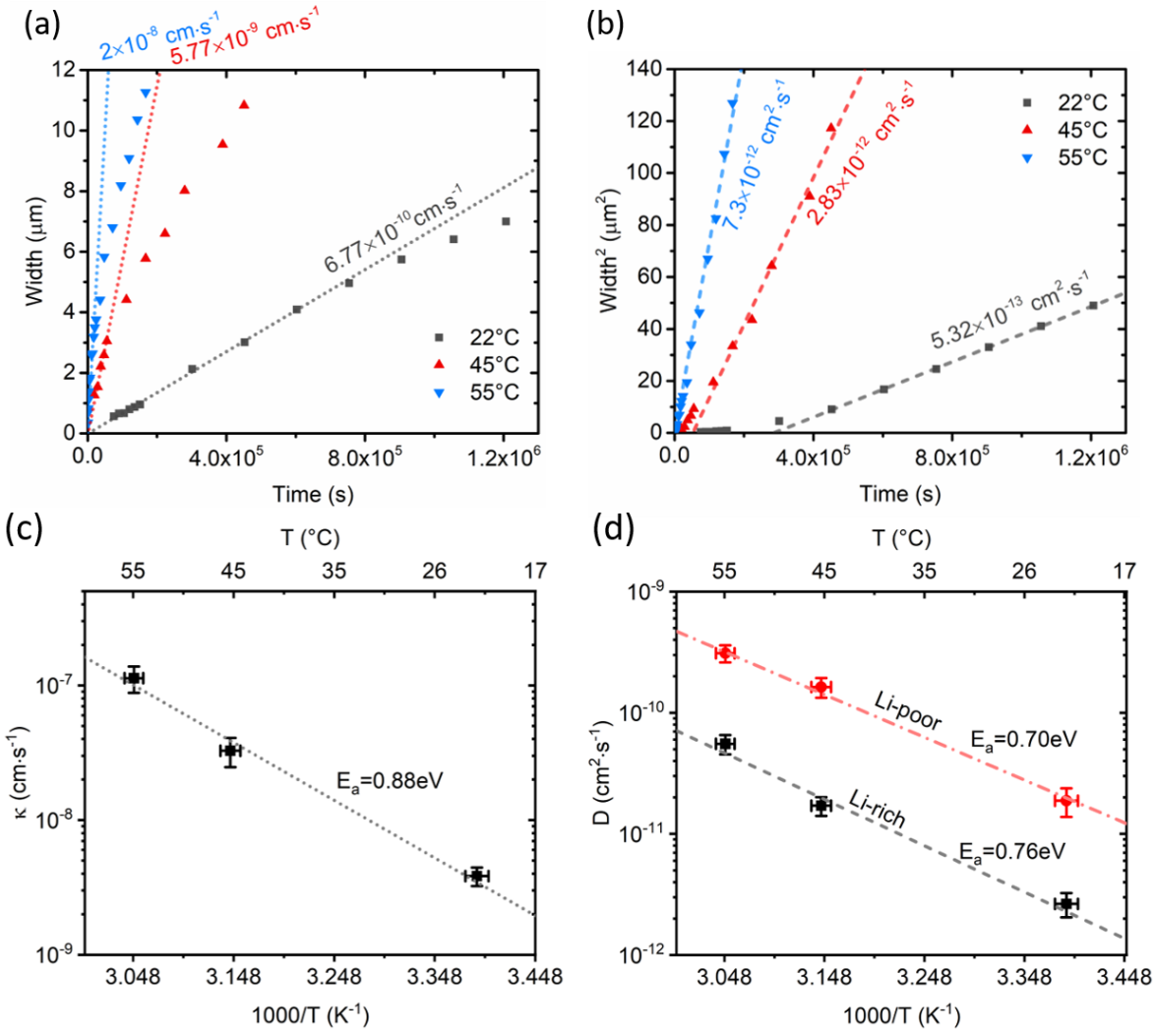

Figure 5-6: *Kinetics of the shift of the phase boundary between the lithium rich phase ($Li_{7/3-\delta}Ti_{5/3}O_4$) and lithium poor phase (($Li_{4/3+\delta}Ti_{5/3}O_4$)) at 22°C, 45°C and 55°C. (a) Width of lithium rich phase versus time; (b) Square of width of lithium rich phase versus time. Temperature dependence of (c) the linear growth constant κ and (d) the parabolic growth constant D.*[E3]

measured slopes and Equation 5-1, the effective diffusion coefficient and the barrier coefficient are evaluated. Also, from the ratio between both the slopes, the critical thickness of the γ-phase at which linear and parabolic growth rates become identical ($w_{\mathrm{cr}}^{\gamma} = \frac{m_{\mathrm{p}}}{m_{\mathrm{l}}}/2$) is calculated. It represents a characteristic thickness that the Li-rich γ-phase has to reach so that further growth becomes diffusion-limited. The barrier coefficient κ at room temperature amounts to 3.84 ×10^{-9} cm·s^{-1} while the diffusion coefficient of Li in the γ-phase is determined to 1.24×10^{-12} cm^2·s^{-1}. Similar observations are made at other temperatures, see Figure 5-6 (a) and (b). The respective transport coefficients along with the respective critical thickness w_{cr}^{γ}, the time to reach this thickness t_{cr} (calculated using Equation 5-1) are listed in Table 5-1.

***Table 5-1**: Transport coefficients of Li in the Li-rich γ phase and its corresponding critical thicknesses at different temperatures, critical time to reach this thickness, the corresponding width of the Li-poor α phase at this time.[E3]*

Temp (°C)	D_{Li}^{γ} ×10^{-12} (cm^2·s^{-1}) From Eq. 5-1	D_{Li}^{γ} ×10^{-12} (cm^2·s^{-1}) From Eq. 5-2	κ ×10^{-9} (cm·s^{-1}) From Eq. 5-1	w_{cr}^{γ} (µm)	t_{cr} ×10^3 (s)	D_{Li}^{α} ×10^{-11} (cm^2·s^{-1}) From Eq. 5-2	w_{cr}^{α} (µm)
22°C	1.24±0.2	2.65±0.6	3.84±0.6	3.93	870.8	1.88±0.5	40.4
45°C	6.60±1.5	17.1±3	32.7±8	2.45	63.7	16.3±3	32.5
55°C	17.0±2	55.4±10	113±25	1.8	13.7	31±5	20

It should be pointed out that the derivation of Equation 5-1 assumes all the incoming flux is used to grow the Li-rich γ phase. This is not completely true, as the Li-poor α-phase is simultaneously taking lithium from the incoming flux, as can be seen in Figure 5-4 and Figure 5-5(d). Nevertheless, Equation 5-1 provides an efficient method to describe the linear to parabolic transition and to quantify the barrier coefficient. But strictly, a correct evaluation of the diffusion coefficients has to use the Boltzmann-Matano (BM) method (see chapter 1 for details on the method) for semi-infinite geometry in the parabolic regime.[37,42,165–167]

This method considers the full concentration profile at a selected time within the parabolic regime. With this, the diffusion coefficient is evaluated for any given c^* along the concentration profile as:

$$D(c^*) = -\frac{1}{2t}\left.\frac{dx}{dc}\right|_{c^*} \int_0^{c^*} (x - x_M)\, dc \qquad 5\text{-}2$$

As usual, t is the time during which the composition profile has developed by diffusion, dx/dc represents the reciprocal of the concentration gradient at the selected position c^*, and $(x - x_M)$ is the distance from a reference plane situated at x_M. In the present case, x_M has to be set to 0 (edge of the protective coating), as at this plane the concentration remains fixed.[165,166] Practically, the integral represents the area under the concentration profile taken along the concentration axis or y-axis in Figure 5-5(d). This area is bounded by the concentration at which the diffusivity is evaluated and by the lowest concentration of mobile lithium (i.e., between x = c and x = 0 in $Li_{4/3+x}Ti_{5/3}O_4$). Using Equation 5-2, the diffusion coefficients at concentrations c = 0.88 (for the γ-phase) and c = 0.1 (for the α-phase) have been evaluated. These corrected diffusivities are also given in Table 5-1 ("From Eq. 5-2"). It is sufficiently clear that in comparison diffusivities evaluated earlier with Equation 5-2 are slightly underestimated. Based on the determined diffusivity, the diffusion depth in the α-phase at the critical transition time is also calculated ($w_{\mathrm{cr}}^{\alpha} = \sqrt{D_{Li}^{\alpha} \cdot t_{cr}}$) and is shown in the last column of Table 5-1, this is used for later discussion.

The diffusion coefficient for the Li-poor α-phase is evaluated to be 1.88×10^{-11} $cm^2 \cdot s^{-1}$ and that of the Li-rich γ phase to 2.65×10^{-12} $cm^2 \cdot s^{-1}$ at room temperature. This signifies that the diffusion in the α-phase is roughly 7 times that of the γ-phase. Based on electrochemical impedance spectroscopy (EIS), Wang et al.[41] reported for the Li diffusivity in the α-phase 2.2×10^{-11} $cm^2 \cdot s^{-1}$ and 3×10^{-12} $cm^2 \cdot s^{-1}$ for the γ-phase, in convincing agreement with the values determined here. Increased diffusivities in the Li-poor phase were also observed by Schmidt et al.[40] using NMR. From their

reported activation energy and pre-factor, at 22°C, the α-phase is predicted to show a diffusion coefficient of 1.74×10^{-12} $cm^2 \cdot s^{-1}$ whereas the γ-phase has a diffusivity of only 1.19×10^{-13} $cm^2 \cdot s^{-1}$.[40] Reproducing the trend between both phases, the values determined from NMR are nevertheless an order of magnitude lower. This is probably because the diffusivities determined from NMR are representative of self-diffusion whereas the values determined here represent chemical diffusion coefficients (including the thermodynamic factor). The diffusivity in the Li-poor α-phase is higher probably due to the possibility of partial occupancy of the 16c sites, along with the 8a sites. This gives more possibility of jumps hence a higher diffusion coefficient.

The evaluated transport coefficients at different temperatures (see Table 5-1) enables the determination of the activation energies. Respective Arrhenius plots are presented in Figure 5-6 (c) and (d). The values for the diffusivities are the ones determined from the BM method. The data of both transport coefficients agree quite well with Arrhenius-like dependences. The activation energy for the barrier coefficient is 0.88 eV, whereas for the two diffusion coefficients they are 0.70 eV and 0.76 eV in the α and γ phases, respectively. The higher activation energy of the barrier coefficient signifies a stronger temperature dependence and so, particularly at low temperatures, the phase propagation is controlled by the slowly migrating interface for a considerably long time.

The activation energy of the chemical diffusion coefficient evaluated here can be compared with other reports. Schmidt et al.[40] reported a value of 0.62 eV, 0.38 eV, and 0.51 eV for the unreacted LTO, partially lithiated α-phase, and the γ-phase, respectively. Hain et al.[157] reported a value of 0.55 eV and 0.45 eV for the γ and α phases, respectively. Both studies determined the activation energy from the jumping frequency seen in NMR spectroscopy (which, as stated before, represents self-diffusion rather than chemical diffusion). Furthermore, Ziebarth et al.,[159] using first-principle calculations at 0 K, evaluated the energetic barrier for lithium

migration in the Li-rich phase (16c to 8a to 16c) to be between 0.2 to 0.51 eV. However, migration from a 16d site to a 16c site required higher activation energy ranging between 0.80 to 0.94 eV, whereas the reverse path needed activation energy between 0.56 to 0.63 eV. Obviously, the values determined here, corresponding to 0.70 eV and 0.76 eV for the α and γ phase, respectively, represent an average of different jumping processes. In addition, as chemical diffusion coefficients, they may also contain an additional contribution from the temperature dependence of the driving force.

5.2.5 Effect of Electrode Geometry

The clearly demonstrated existence of a kinetic barrier for the migration of the phase boundary prompts the question of its impact on the performance in technical battery electrodes. Generally, a battery electrode particle may be better assumed to be of finite size with an approximately spherical geometry where 3-dimensional (3-D) atomic migration is taking place. Due to the small depth of focus of the optical microscope, a 3-D geometry is difficult to analyze with the present

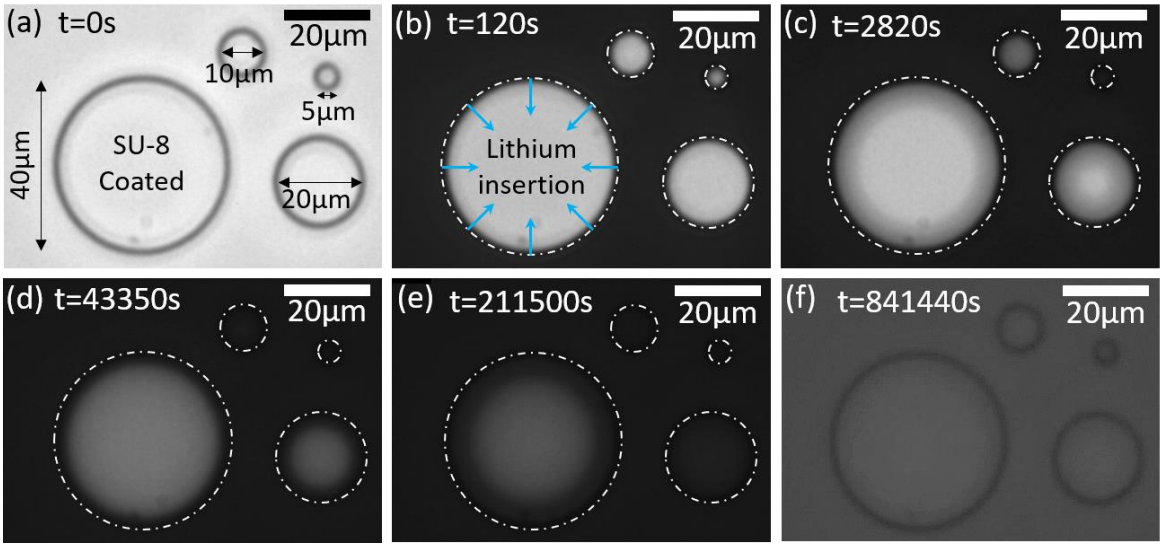

***Figure 5-7**: (a) Different circular lithography patterns observed at t=0 s during the electrocromic imaging experiments. (b) At 120 s, all the uncovered area has transformed into the Li-rich phase (black), while the resist-coated circular areas are clearly visible. Further images taken after longer times: (c) 2820s; (d) 43350s; (e) 211500s and (f) 841440s (enhanced brightness and contrast), when the patterns with radius 2.5µm, 5µm, 10µm and 20µm were completely saturated with the Li-rich phase, respectively.[E3]*

setup. But a planar cylindrical disk (representing a model geometry for 2D migration of atoms) poses no complication. Therefore, the SU-8 was coated in circular-disk geometries with varying radius i.e., *R*= 2.5, 5, 10, 20 µm, as shown in Figure 5-7 (a). Point to note, out of these, the 2.5 and 5 µm are close to the critical transition width determined for the Li-rich phase at room temperatures. Thus, it is expected that the lithiation of these smaller "particles" should be significantly slowed down by linear kinetics. The figure shows the patterns with varying radii on a single substrate at t=0s. Again, for electrochromic imaging of the intercalation at room temperature, the voltage step is initiated at t=0s. As before, the uncovered area is transformed into the $Li_{7/3}Ti_{5/3}O_4$ phase almost immediately, as shown in Figure 5-7 (b) after 120s, whereas it takes 2820s (Figure 5-7 (c)) to completely transform the blocked area of 2.5 µm radius to the Li-rich phase. Still, this would correspond to a charging rate faster than 1C for a relatively big particle of 5 µm in diameter (in the case of a spherical particle of the same diameter, it would be even somewhat faster due to 3-D transport). Subsequently, to completely transform the areas of 5 µm, 10 µm, and 20 µm radius into the Li-rich phase, it needed 43.4 ks, 212 ks, and 841 ks, respectively, as shown in the corresponding Figure 5-7(d), (e) and (f). In the larger disks (10 µm and 20 µm radius), the migration of the phase boundary can be evaluated in detail. This confirms the existence of slower linear growth of the Li-rich phase in the initial stages of lithiation, see Figure 5-8 (a) and (b), respectively. Only at a later time, diffusion-controlled growth of the Li-rich phase is observed as depicted in Figure 5-8 (c) and (d).

It comes as a surprise, however, that the critical thicknesses of the transition to the parabolic regime are systematically smaller for the circular discs in comparison to the 1D semi-infinite geometry. The critical transition thicknesses for the circular disk with 10 µm and 20 µm radius are 1.2 µm and 2.9 µm, respectively, while for the semi-infinite case discussed before, it was 3.9 µm. It appears that the critical thickness decreases when shrinking the particle size, or in other words with decreasing available space for lithium migration. A point to note, since the critical

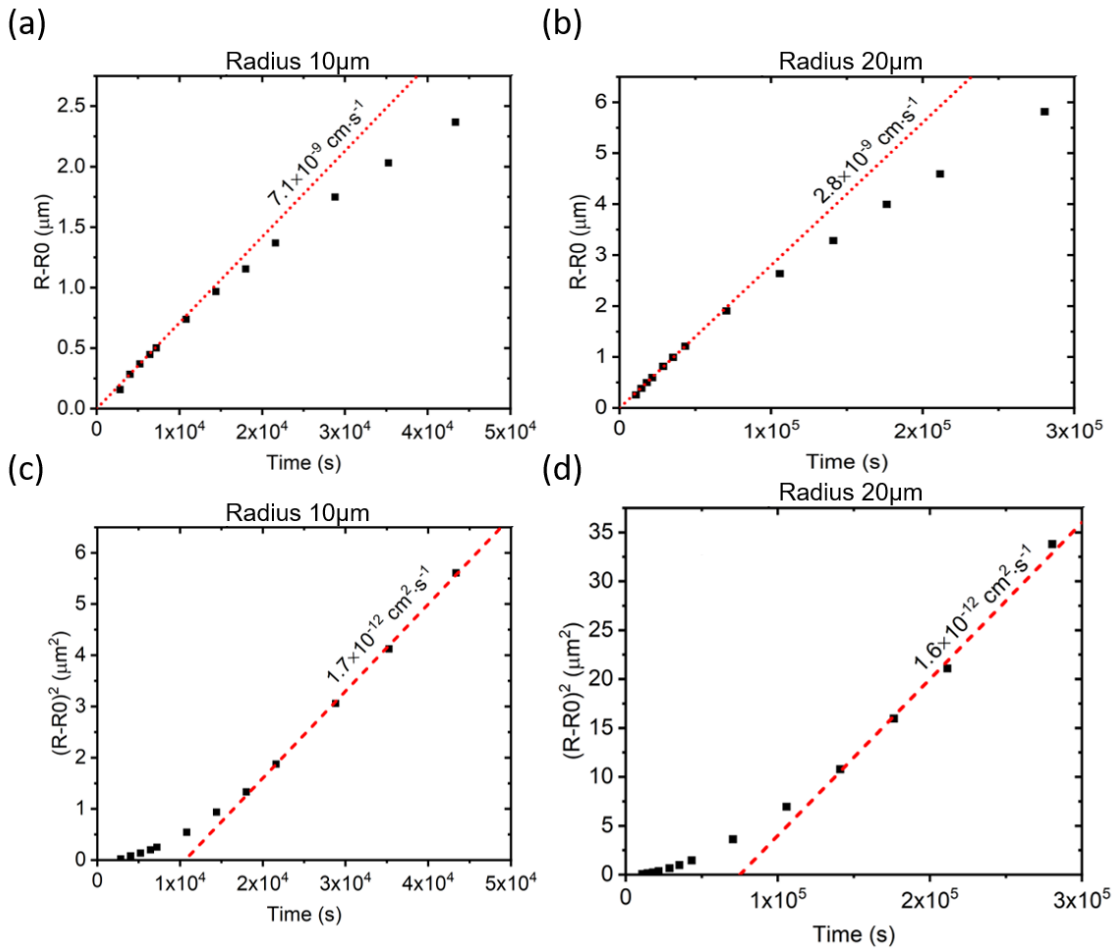

***Figure 5-8**: Growth of Li-rich phase in the circular geometry with radius (a) 10 µm and (b) 20 µm. (c) and (d) show the corresponding plots of the square of width versus time, respectively.[E3]*

thicknesses are reduced in the circular geometry, it takes merely 1/11th and 1/7th of the total time for lithiation in 10 µm and 20 µm disks, respectively, to reach the diffusion-controlled regime so that the full lithiation is effectively controlled by parabolic growth (cf. Figure 5-6(a), Figure 5-8(a,b)) opposed to the initial expectation.

5.3 Discussion

The kinetic barrier evaluated so far, could principally be due to two credible interfaces (for a layer-like growth of a reaction-product), first that at the phase boundary between γ and α phases and second, the Butler-Volmer type interface at the solid/liquid interface. However, the particular geometry of the current set-up excludes any significant impact of the latter, due to the much larger contact area

to the electrolyte in comparison to the transport cross-sectional area perpendicular to the thin-film. As is clearly seen from the fast reaction in the uncoated parts of the electrode, a possible kinetic control by the Butler-Volmer interface can be significant only on the much shorter time scale of a few seconds. Thus, the origin of the here-determined barrier coefficient has to be unambiguously attributed to the interface between the γ and the α phases, at which the majority of the Li atoms are forced to change their interstitial position from 16c to 8a. Such barrier coefficient originating from the phase boundary has not been evaluated in any battery electrode previously, although Berkemeier et al.[53] did report the barrier coefficient for lithium migration for the Butler-Volmer interface in the case of lithium cobalt oxide.

The possible microscopic origin of the kinetic barrier to boundary migration needs further consideration. In the classical case of intermetallic growth via substitutional interdiffusion, and even in the case of interstitial compounds such as the growth of silicides[47–49] and hydrides[50,51], the existence of a kinetic barrier has been justified by the hindered migration of atoms through the phase boundary. Given the fast growth of the Li-poor α phase beyond the interface, this is probably not the case here, (cf. concentration profile in Figure 5-5 (d)). Furthermore, the barrier coefficient is usually seen as a generic property of the interface while the diffusion coefficient is a generic property of the volume, both certainly not depending on the diffusion geometry. Therefore, the here observed dependence of the kinetic transition on the sample geometry is an absolutely striking result.

A detailed kinetic modeling of the observed effect is beyond the scope of this experimental thesis, but at least one possible interpretation should be outlined here. Consider the exemplary situation of an interface oriented perpendicular to a (010) direction of the cubic spinel structure (see left part of Figure 5-9 (a) showing only lithium atoms). Thus, Li sites are stacked in the main diffusion direction in an alternating way between planes of two 8a-sites (per cubic unit cell with 32 atoms),

each having two possibilities for the forward jumps to the neighbored 16c-sites, and planes of four 16c-sites, each having only a single jump possibility in the forward direction. A lithium atom in the γ phase is likely to be occupying a 16c site, and if it were to jump forward into the α phase, it needs to move via an empty 8a site (as shown by the dotted arrow at the Li-rich side).[62,158,159,168] The subsequent jump will occur into the empty 16c in the Li-poor phase, in which most of the 8a sites are filled. Schmidt et al.[40] and Zhang et al.[169] pointed out that a neighboring occupancy of 8a and 16c sites results in severe coulombic repulsion. Therefore, as soon as the Li-ion has occupied the 16c site, it will propagate further, resulting in

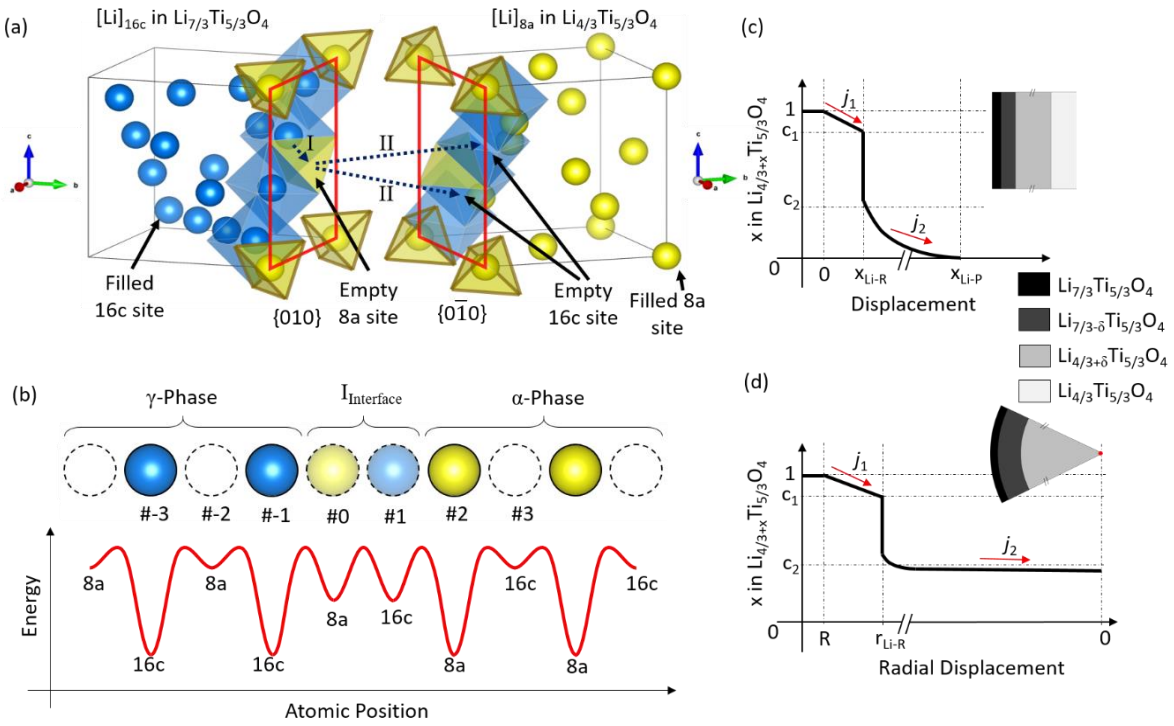

***Figure 5-9**: (a) Position of Li-atoms at 16c sites (Blue) and 8a sites (Yellow) in γ and α phases, and the dotted line shows migration of a lithium atom as shown by dashed arrow, at the phase boundary (highlighted by red edges). (b) Distribution of Li atoms in an exemplary diffusion direction, when viewed from <001> direction. The White (dashed edges), Blue and Yellow circles represent the empty sites, the filled 16c sites and 8a site. The light-blue and yellow circles (dashed edges) represent the partially filled 16c and 8a sites at the phase boundary region. The probable energy distribution at 16c and 8a sites when moving from γ-phase (on left) to α-phase on the right. Illustrative concentration profiles in the diffusion direction for: (c) Semi-infinite diffusion geometry; and (d) A spherical (or circular) particle of radius R, undergoing the phase transformation via radially inward flux, when the Li-poor phase has completely saturated.[E3]*

the outward flux into the volume of the α phase with a much faster diffusion coefficient. Only in statistically rare cases, simultaneous jumps by other Li atoms from 8a (corner atoms at the phase boundary, highlighted by the polyhedral with dark yellow edges in Figure 5-9(a)) into the neighbored 16c sites may form a nucleus of a next lattice plane of the γ phase and so will result in the net movement of the phase boundary.

In consequence, at least two planes must exist at the interface where the Li occupancy is disturbed with respect to the adjacent phase volume. So, an energy landscape can be imagined of the Li sites, as schematically sketched in Figure 5-9(b). Before the interface, the energy of an 8a-site is high while that of a 16c-site is low, beyond the interface just the opposite holds. But at the two interface planes, the site energies of 8a and 16c may approach to an intermediate level because of the disturbed next-neighborhood. For convenience, the planes are numbered by fixing the origin to the 8a plane in the interface. A migration of the interface to the right-hand side requires nucleation of a new rock-salt double-layer, meaning, at least a cooperative shift of Li-ions from the 8a-sites on plane #0 to 16c-sites of plane #1. This nucleation needs a minimum driving force by supersaturation of the Li content at the interface with respect to the equilibrium level in the α phase. Thus, the Li concentration on the two interfacial planes (#0, #1) is decisive for further migration of the interface. In a steady-state condition, this concentration is controlled by the Li fluxes in the vicinity to the interface, formally expressed as:

$$j_{-1\to 0} = \nu^{\gamma}_{\mathrm{c}\to\mathrm{a}}\, c^{\gamma}_{\mathrm{c}}\,(1 - c^{\mathrm{I}}_{\mathrm{a}}) \qquad \textit{5-3 a}$$

$$j_{0\to 1} = 2\nu^{\mathrm{I}}_{\mathrm{a}\to\mathrm{c}}\, c^{\mathrm{I}}_{\mathrm{a}}\,(1 - c^{\mathrm{I}}_{\mathrm{c}}) \qquad j_{1\to 0} = \nu^{\mathrm{I}}_{\mathrm{c}\to\mathrm{a}}\, c^{\mathrm{I}}_{\mathrm{c}}\,(1 - c^{\mathrm{I}}_{\mathrm{a}}) \qquad \textit{5-3 b,c}$$

$$j_{1\to 2} = \nu^{\mathrm{I}}_{\mathrm{c}\to\mathrm{a}}\, c^{\mathrm{I}}_{\mathrm{c}}\,(1 - c^{\alpha}_{\mathrm{a}}) \qquad j_{2\to 1} = 2\nu^{\alpha}_{\mathrm{a}\to\mathrm{c}}\, c^{\alpha}_{\mathrm{a}}\,(1 - c^{\mathrm{I}}_{\mathrm{c}}) \qquad \textit{5-3 d,e}$$

$$j_{2\to 3} = \nu^{\alpha}_{\mathrm{a}\to\mathrm{c}}\, c^{\alpha}_{\mathrm{a}}\,(1 - c^{\alpha}_{\mathrm{c}}) \qquad \textit{5-3 f}$$

In these equations, *j,* ν and *c* represent the directed fluxes between the indexed planes, the jump frequencies (affected by the site energy via Boltzmann activation factors), and the Li concentration on the indexed plane, respectively; the super and

subscript indexes have their natural meaning in the present context (I: interface, α, γ: the two phases, a: 8a-site, c: 16c-site). In the non-equilibrium situation of linear growth, the backward flux $j_{0\to-1}$ can be neglected relative to the corresponding forward flux $j_{-1\to0}$, since the applied cell voltage forces the concentration of Li in the γ phase (c_{c}^{γ}) to much higher levels than the equilibrium, i.e., tending towards 1. In the early stages of intercalation, the concentration gradient in the α phase after the interface and thus the drain flux $j_{2\to3}$ are initially large, therefore c_{a}^{α} in Equation 5-3e is depressed (as lithium is driven away by the high $j_{2\to3}$ from position #2) and therefore the backward flux $j_{2\to1}$ becomes negligible. Consequently, the Li supersaturation at the interface is a constant, solely defined by the balance between the forward fluxes $j_{-1\to0}$ and $j_{1\to2}$. So, the nucleation of the new rock-salt structure and thus the migration of the interface appears with a slow but constant rate, interface migration proportional to time is observed. In the course of further intercalation, however, the concentration gradient in the α phase decreases and so does the forwards flux $j_{2\to3}$ (Equation 5-3f). Consequently, the back flux $j_{2\to1}$ increases, and as soon as it becomes comparable to the corresponding forward flux $j_{1\to2}$, the Li concentration at the interface increases significantly, and with this the nucleation rate, too. Exceeding a certain threshold, the nucleation rate becomes fast enough so that the diffusion transport across the formed γ layer starts limiting the phase growth which then appears as a parabolic time dependence.

In this scenario, it is observed that the concentration gradient in the α phase, although located ahead of the phase boundary in the transport direction, makes a decisive impact owing to the competition for Li that either feeds the supersaturation at the interface or drains into the α phase. Since the Li diffusion width in the α phase is considerably larger than in the γ phase, the reduction of space in the studied finite-sized circular structures to the order of a few micrometers, leads to a much earlier saturation of the Li content in the α phase and therefore depresses the further Li drain (see the illustrative concentration

profiles in Figure 5-9 (c) and (d) for the semi-infinite and finite circular geometry). In final consequence, it is no more the critical thickness of the γ phase, but the diffusion depth within the α phase in comparison to the sample size, which controls the transition into the parabolic regime, exactly as observed in the experiment. In order to prevent hindrance of intercalation by the slowly migrating interface, the anode particles must be chosen small enough so that diffusion width in the Li-poor phase gets larger than the typical particle size.

5.4 Summary

A new methodology to study lithium transport in thin-film battery electrodes is reported in this chapter. It exploits the electrochromic activity of lithium titanate and enables quantitative evaluation in terms of averaged transport coefficients and activation energy. The optical contrast provides convincing evidence for a two-phase lithiation reaction. The diffusion coefficient for lithium in the Li-rich phase $Li_{7/3-\delta}Ti_{5/3}O_4$ at 22°C was determined to be 2.65×10^{-12} $cm^2\cdot s^{-1}$ with an activation energy of 0.76 eV. The diffusion of lithium in the Li-poor phase $Li_{4/3+\delta}Ti_{5/3}O_4$ is about 7 times faster with an activation energy of 0.70 eV. A linear-to-parabolic transition in the phase growth demonstrates a kinetic barrier against migration of the phase boundary. Provided unrestricted diffusion in the Li-poor phase, the respective barrier coefficient amounts to 3.84×10^{-9} $cm\cdot s^{-1}$ at 22 °C with an activation energy of 0.88 eV. The barrier at the interface significantly slows down the growth of the Li-rich phase up to a width of about 4 μm. The migration of the interphase interface is most likely controlled by continuous nucleation of new atomic layers of the Li-rich phase. The nucleation rate depends on the Li supersaturation at the interface and so can be controlled by the diffusion concentration profile in the Li-poor phase. As a practical consequence, the overall kinetics of intercalation in nano- or micro-particles is effectively controlled by the large diffusion width in the Li poor phase rather than by the slow diffusion in the Li-rich phase or the kinetic barrier at the interface.

Conclusion and Outlook

This thesis innovates and utilizes new methodologies that enrich the current understanding of the optical response in two of the well-established electrode materials, namely $LiMn_2O_4$ and $Li_4Ti_5O_{12}$. For the latter, the kinetics of lithium migration was also elucidated.

The quantification of optical constants in these materials was made possible by using thin films, which provide a model geometry for analyzing complex physical phenomena. In this case, the simple geometry helped with the analytical description of the optical spectrum obtained by illuminating the sample normally. The model comprised the complex refractive index (CRI) of the electrode material as defined by the Clausius-Mossotti relation and the summation of multiple reflections at the interfaces governed by Fresnel's reflection coefficients. The extracted the CRI of the material rationalizes the absorption behavior of the films in terms of electronic excitation. Furthermore, the shift in the absorption peaks upon lithiation/de-lithiation could be rationalized by the change in the transition energies resulting from the filling/removal of electrons when lithium is inserted/removed.

In the case of $Li_xMn_2O_4$ (LMO), two significant resonances were identified within the visible region of the wavelength spectrum. They were attributed to the electronic transitions between the O-2p band and the split Mn-d band. The removal of lithium from this cathode material resulted in the shifting of these resonances to higher wavelengths or lower energies.

For the spinel structured $Li_4Ti_5O_{12}$, the model description of the optical spectrum revealed the presence of a single strong resonance. This was assigned to the transition from O-2p to Ti-t_{2g} bands, i.e. across the band-gap of the material. Upon lithium insertion, the $Li_4Ti_5O_{12}$ phase undergoes a phase transformation to the rock-salt type $Li_7Ti_5O_{12}$ phase. Two resonances, corresponding to the electronic

transitions from O-2p to empty Ti-t_{2g} bands, and from the filled Ti-t_{2g} to empty Ti-e_g bands, could be identified for this rock-salt phase.

The possibility to measure reflectance spectra in-situ during an electrochemical measurement was also realized in this work. It resulted in capturing the reversible optical change demonstrated by both the electrode materials. Hence, these two materials could be considered as a possible candidate for an on-chip optical switching application.

Additionally, in the case of LTO, the optical information obtained from the complex refractive index was used to obtain its dielectric properties. The dielectric properties at different intercalation states along with the microstructural information of the material, and the superposition rules for the effective dielectric constant, revealed that the grain boundaries are energetically favorable for the nucleation of the rock-salt phase. Hence, it is concluded that $Li_7Ti_5O_{12}$ is first nucleated at the GB's and further phase growth occurs via bulk diffusion through the grains.

Due to the huge increase in the optical absorption upon lithiation in $Li_{4+x}Ti_5O_{12}$, the material was an ideal candidate for the development of a methodology to probe the kinetics of lithium migration using optical microscopy. The envisioned methodology works by coating a part of the dense sputter-deposited thin-film electrode with an optically transparent, lithium-blocking photoresist, using e-beam lithography. Upon the subsequent electrochemical insertion of lithium in $Li_{4+x}Ti_5O_{12}$, the uncoated area transformed into the $Li_7Ti_5O_{12}$ phase instantaneously. In the blocked area, the lateral migration of lithium was observable. The optical contrast provided evidence for a two-phase lithiation reaction. By heating the cell using externally placed Peltier elements, the kinetic measurements were undertaken at 45°C and 55°C. This revealed Arrhenius-like dependence and the corresponding activation energy of all the transport coefficients. From the obtained concentration profiles, the diffusion coefficient for lithium in the rock-salt

$Li_7Ti_5O_{12}$ phase was determined to be 2.65×10^{-12} $cm^2\cdot s^{-1}$ at 22°C with an activation energy of 0.76 eV. For the spinel structured $Li_{4+\delta}Ti_5O_{12}$ phase, the diffusion coefficient was determined to be 7 times higher than the one for $Li_7Ti_5O_{12}$ phase but with a lower activation energy of 0.70 eV. Surprisingly, the initial stage of the growth of $Li_7Ti_5O_{12}$ with time, i.e. the movement of the phase-boundary, was not following a conventional parabolic dependence but rather a linear dependence. This has been characterized here by a barrier coefficient which is determined to be 3.84×10^{-9} $cm\cdot s^{-1}$ at 22°C with the activation energy of 0.88 eV.

Additional measurements at 22°C with limited diffusion space in smaller circular disk geometry, revealed a surprising result. The critical thickness (linear-to-parabolic transition) depends on the available diffusion space. Consequently, it was established that the origin of the barrier coefficient cannot be simply due to the slow migration of lithium across the phase-boundary, rather it would depend on the continuous nucleation of the Li-rich phase. The nucleation rate is observed to be dependent on the super-saturation of lithium at the interface, and the neighboring concentration gradient. Therefore, only a decrease in the concentration gradient in the Li-poor phase could explain the reduction of the critical thickness with the reduced diffusion space.

The present thesis provides a framework to characterize battery electrodes using their optical properties which can be easily extended to other materials as well. For the case of optical characterization, the additional effects of elemental doping on the optical behavior of an electrode can be looked into, e.g., the effect of nickel doping in LMO, etc.. The realization of the technical goal for an on-chip device needs a few further steps, such as sputtering the active material on top of the silicon waveguide and probing the effects of de-/lithiation on the output signal. The second method, investigation lateral diffusion, can be extended to study: homogeneous nucleation of a phase at ultra-low charging rates, the effect of varying surface area to volume ratio on the kinetics of lithium migration,

differences in lithiation and de-lithiation kinetics, the effects of GB diffusion on Harrison's type A kinetics, etc.

References

Publications by the author towards the completion of this thesis.

E1 Y. Joshi, E. Hadjixenophontos, S. Nowak, R. Lawitzki, P. K. Ghosh and G. Schmitz, "Modulation of the Optical Properties of Lithium Manganese Oxide via Li-Ion De/Intercalation", *Adv. Opt. Mater.*, 2018, 6, 1701362.

E2 Y. Joshi, A. Saksena, E. Hadjixenophontos, J. M. Schneider and G. Schmitz, "Electrochromic Behavior and Phase Transformation in $Li_{4+x}Ti_5O_{12}$ upon Lithium-Ion Deintercalation/Intercalation", *ACS Appl. Mater. Interfaces*, 2020, 12, 10616–10625.

E3 Y. Joshi, R. Lawitzki and G. Schmitz, "*Slow-Moving Phase Boundary in $Li_{4/3+x}Ti_{5/3}O_4$*", Small Methods (Accepted), 2021.

Other references

1 S. Trasatti, *J. Electroanal. Chem.*, 1999, **460**, 1–4.

2 M. Faraday, *Philos. Trans. R. Soc. London*, 1834, **124**, 77–122.

3 B. Scrosati, *J. Solid State Electrochem.*, 2011, **15**, 1623–1630.

4 M. V. Reddy, A. Mauger, C. M. Julien, A. Paolella and K. Zaghib, *Materials (Basel).*, 2020, **13**, 1884.

5 M. Lazzari and B. Scrosati, *J. Electrochem. Soc.*, 1980, **127**, 773–774.

6 K. MIZUSHIMA, P. JONES, P. WISEMAN and J. GOODENOUGH, *Solid State Ionics*, 1981, **3**–**4**, 171–174.

7 M. M. M. Thackeray, P. J. J. Johnson, L. A. A. de Picciotto, P. G. G. Bruce and J. B. B. Goodenough, *Mater. Res. Bull.*, 1984, **19**, 179–187.

8 A. K. Padhi, K. S. Nanjundaswamy and J. B. Goodenough, *J. Electrochem. Soc.*, 1997, **144**, 1188–1194.

9 A. Yamada, S. C. Chung and K. Hinokuma, *J. Electrochem. Soc.*, 2001, **148**, A224.

10 T. Ohzuku, A. Ueda and N. Yamamoto, *J. Electrochem. Soc.*, 1995, **142**, 1431–1435.

11 C. Julien, A. Mauger, A. Vijh and K. Zaghib, *Lithium Batteries*, Springer International Publishing, Cham, 2016.

12 C. G. Granqvist, *Thin Solid Films*, 2014, 564, 1–38.

13 M. Planck, *Ann. Phys.*, 1901, **309**, 553–563.

14 M. Fox, *Optical Properties of Solids*, OUP Oxford, 2010.

15 J. H. Lambert, *Photometria sive de mensura et gradibus luminis, colorum et umbrae*, W. Engelmann, Leipzig, 1760.

16 Beer, *Ann. der Phys. und Chemie*, 1852, **162**, 78–88.

17 L. Cauchy, *Bull. des sc. Math.*, 1830, **14**, 6–10.

18 W. Sellmeier, *Ann. der Phys. und Chemie*, 1871, **219**, 272–282.

19 H. A. Lorentz, *The theory of electrons and its applications to the phenomena of light and radiant heat*, B.G. Teubner, Leipzig, 2nd Editio., 1916.

20 E. Hecht, *Optics*, Pearson Education, Incorporated, 2017.

21 R. Clausius, *Die Mechanische Behandlung der Electricität*, Vieweg Teubner Verlag, Wiesbaden, 1879.

22 O. F. Mossotti, *Mem. di Math. e di Fis. della Soc. Ital. della Sci. Resid. Modena*, 1850, **24**, 49–74.

23 H. A. Kramers, in *Atti del Congresso internazionale dei fisici, vol. 2*, ed. N. Zanichelli, Bologna, 1927, pp. 545– 557.

24 R. de L. Kronig, *J. Opt. Soc. Am.*, 1926, **12**, 547–557.

25 A.-J. Fresnel, *Ann. Chim. Phys.*, 1821, **2**, 102–11.

26 O. S. Heavens, *Optical Properties of Thin Solid Films*, Butterworths Scientific Publication, 1955, vol. 33.

27 P. R. Somani and S. Radhakrishnan, *Mater. Chem. Phys.*, 2003, **77**, 117–133.

28 C. G. G. C. G. Granqvist and C. G. G. C. G. Granqvist, *Handbook of Inorganic Electrochromic Materials*, Elsevier, Amsterdam, 1995.

29 S. K. Deb, *Appl. Opt.*, 1969, **8**, 192.

30 J. S. E. M. Svensson and C. G. Granqvist, *Sol. Energy Mater.*, 1984, **11**, 29–34.

31 A. Fick, *Ann. Phys.*, 1855, **170**, 59–86.

32 T. Graham, *London, Edinburgh, Dublin Philos. Mag. J. Sci.*, 1833, **2**, 175–190.

33 H. Mehrer, in *Defect and Diffusion Forum*, Trans Tech Publications Ltd, 2006, vol. 258–260, pp. 1–14.

34 A. Einstein, *Ann. Phys.*, 1905, **322**, 549–560.

35 M. von Smoluchowski, *Ann. Phys.*, 1906, **326**, 756–780.

36 L. Onsager, *Phys. Rev.*, 1931, **38**, 2265–2279.

37 Z. Balogh and G. Schmitz, in *Physical Metallurgy: Fifth Edition*, Elsevier Inc., 2014, vol. 1, pp. 387–559.

38 S. B. Tang, M. O. Lai and L. Lu, *Mater. Chem. Phys.*, 2008, **111**, 149–153.

39 M. D. Chung, J. H. Seo, X. C. Zhang and A. M. Sastry, *J. Electrochem. Soc.*, 2011, **158**, A371.

40 W. Schmidt, P. Bottke, M. Sternad, P. Gollob, V. Hennige and M. Wilkening, *Chem.*

Mater., 2015, **27**, 1740–1750.

41 C. Wang, S. Wang, Y.-B. He, L. Tang, C. Han, C. Yang, M. Wagemaker, B. Li, Q.-H. Yang, J.-K. Kim and F. Kang, *Chem. Mater.*, 2015, **27**, 5647–5656.

42 C. Matano, *Japanese J. Phys.*, 1933, **8**, 109–113.

43 L. Boltzmann, *Ann. Phys.*, 1894, **289**, 959–964.

44 Z. Erdélyi and G. Schmitz, *Acta Mater.*, 2012, **60**, 1807–1817.

45 J. J. Tomán, G. Schmitz and Z. Erdélyi, *Comput. Mater. Sci.*, 2017, **138**, 183–191.

46 U. Gösele and K. N. Tu, *J. Appl. Phys.*, 1982, **53**, 3252.

47 B. Parditka, H. Zaka, G. Erdélyi, G. A. Langer, M. Ibrahim, G. Schmitz, Z. Balogh-Michels and Z. Erdélyi, *Scr. Mater.*, 2018, **149**, 36–39.

48 F. Nemouchi, D. Mangelinck, C. Bergman, P. Gas and U. Smith, *Appl. Phys. Lett*, 2005, **86**, 41903.

49 B. E. Deal and A. S. Grove, *J. Appl. Phys.*, 1965, **36**, 3770.

50 E. Hadjixenophontos, K. Zhang, A. Weigel, P. Stender and G. Schmitz, *Int. J. Hydrogen Energy*, 2019, **44**, 27862–27875.

51 E. Hadjixenophontos, L. Michalek, M. Roussel, M. Hirscher and G. Schmitz, *Appl. Surf. Sci.*, 2018, **441**, 324–330.

52 G. V. Kidson, *J. Nucl. Mater.*, 1961, **3**, 21–29.

53 F. Berkemeier, T. Stockhoff, T. Gallasch and G. Schmitz, *Acta Mater.*, 2014, **80**, 132–140.

54 R. Usiskin and J. Maier, *Adv. Energy Mater.*, 2021, 11, 2001455.

55 J. Maier, in *Physical Chemistry of Ionic Materials*, John Wiley & Sons, Ltd, Chichester, UK, 2005, pp. 399–499.

56 A. Vasileiadis, N. J. J. de Klerk, R. B. Smith, S. Ganapathy, P. P. R. M. L. Harks, M. Z. Bazant and M. Wagemaker, *Adv. Funct. Mater.*, 2018, **28**, 1705992.

57 M. Z. Bazant, *Acc. Chem. Res.*, 2013, **46**, 1144–1160.

58 R. B. Smith and M. Z. Bazant, *J. Electrochem. Soc.*, 2017, **164**, E3291–E3310.

59 R. E. Usiskin and J. Maier, *Phys. Chem. Chem. Phys.*, 2018, **20**, 16449–16462.

60 J. Maier, in *Physical Chemistry of Ionic Materials*, John Wiley & Sons, Ltd, Chichester, UK, 2005, pp. 268–398.

61 D. Danilov, R. A. H. Niessen and P. H. L. Notten, *J. Electrochem. Soc.*, 2011, **158**, A215.

62 S. Ganapathy, A. Vasileiadis, J. R. Heringa and M. Wagemaker, *Adv. Energy Mater.*, 2017, **7**, 1601781.

63 N. J. J. De Klerk and M. Wagemaker, *ACS Appl. Energy Mater.*, 2018, **1**, 5609–5618.

64 H. Mehrer, *Diffusion in Solids*, Springer Berlin Heidelberg, Berlin, Heidelberg, 2007, vol. 155.

65 N. Kuwata, M. Nakane, T. Miyazaki, K. Mitsuishi and J. Kawamura, *Solid State Ionics*, 2018, **320**, 266–271.

66 C. Schwab, A. Höweling, A. Windmüller, J. Gonzalez-Julian, S. Möller, J. R. Binder, S. Uhlenbruck, O. Guillon and M. Martin, *Phys. Chem. Chem. Phys.*, 2019, **21**, 26066–26076.

67 T. Okumura, T. Fukutsuka, Y. Uchimoto, N. Sakai, K. Yamaji and H. Yokokawa, *J. Power Sources*, 2009, **189**, 643–645.

68 M. Wagemaker, E. R. H. van Eck, A. P. M. Kentgens and F. M. Mulder, *J. Phys. Chem. B*, 2009, **113**, 224–230.

69 J. Bréger, M. Jiang, N. Dupré, Y. S. Meng, Y. Shao-Horn, G. Ceder and C. P. Grey, *J. Solid State Chem.*, 2005, **178**, 2575–2585.

70 L. de Broglie, University of Paris, 1924.

71 C. W. Oatley, *J. Appl. Phys.*, 1982, **53**, R1–R13.

72 L. A. Giannuzzi, B. W. Kempshall, S. M. Schwarz, J. K. Lomness, B. I. Prenitzer and F. A. Stevie, in *Introduction to Focused Ion Beams*, 2005, pp. 201–228.

73 S. Mishra and G. Ceder, *Phys. Rev. B*, 1999, **59**, 6120–6130.

74 V. W. J. Verhoeven, I. M. de Schepper, G. Nachtegaal, A. P. M. Kentgens, E. M. Kelder, J. Schoonman and F. M. Mulder, *Phys. Rev. Lett.*, 2001, **86**, 4314–4317.

75 V. Massarotti, D. Capsoni, M. Bini and G. Chiodelli, 1999, **515**, 509–515.

76 M. Seyedahmadian, *Bull. Korean Chem. Soc.*, 2013, **34**, 622–628.

77 G. E. Grechnev, R. Ahuja, B. Johansson and O. Eriksson, *Phys. Rev. B*, 2002, **65**, 174408.

78 Y. Liu, T. Fujiwara, H. Yukawa and M. Morinaga, 1999, **126**, 209–218.

79 L. Lüken, Westfälische Wilhelms Universität Münster, 2014.

80 M. Molenda, R. Dziembaj, E. Podstawka and L. M. Proniewicz, *J. Phys. Chem. Solids*, 2005, **66**, 1761–1768.

81 S. T. Lee, K. Raveendranath, M. R. Tomy, M. Paulraj, S. Jayalekshmi and J. Ravi, *Appl. Phys. Lett.*, 2007, **90**, 3–6.

82 B. Ammundsen, G. R. Burns, M. S. Islam, H. Kanoh and J. Roziere, *J. Phys. Chem. B*, 1999, **103**, 5175–5180.

83 M. Roeder, A. B. Beleke, U. Guntow, J. Buensow, A. Guerfi, U. Posset, H. Lorrmann, K. Zaghib and G. Sextl, *J. Power Sources*, 2016, **301**, 35–40.

84 Same as E1

85 M. J. Young, H. D. Schnabel, A. M. Holder, S. M. George and C. B. Musgrave, *Adv.*

Funct. Mater., 2016, **26**, 7895–7907.

86 K. Hoang, *J. Mater. Chem. A*, 2014, **2**, 18271–18280.

87 H. Berg, K. Göransson, B. Noläng and J. O. Thomas, *J. Mater. Chem.*, 1999, **9**, 2813–2820.

88 J. Mürter, S. Nowak, E. Hadjixenophontos, Y. Joshi and G. Schmitz, *Nano Energy*, , DOI:10.1016/J.NANOEN.2017.11.038.

89 J. G. Mürter, University of Stuttgart, 2016.

90 D. G. Wickhamt and W. J. Croft, *J. Phys. Chem. Solids*, 1958, **7**, 351–360.

91 T. Ohzuku, M. Kitagawa and T. Hirai, *J. Electrochem. Soc.* , 1990, **137**, 769–775.

92 J.-Y. Luo, X.-L. Li and Y.-Y. Xia, *Electrochim. Acta*, 2007, **52**, 4525–4531.

93 C. Julien, E. Haro-Poniatowski, M. . Camacho-Lopez, L. Escobar-Alarcon and J. Jimenez-Jarquin, *Mater. Sci. Eng. B*, 2000, **72**, 36–46.

94 J. Xie, K. Kohno, T. Matsumura, N. Imanishi, A. Hirano, Y. Takeda and O. Yamamoto, *Electrochim. Acta*, 2008, **54**, 376–381.

95 J. Xie, T. Tanaka, N. Imanishi, T. Matsumura, A. Hirano, Y. Takeda and O. Yamamoto, *J. Power Sources*, 2008, **180**, 576–581.

96 W. S. M. M. Werner, K. Glantschnig and C. Ambrosch-Draxl, *J. Phys. Chem. Ref. Data*, 2009, **38**, 1013–1092.

97 E. W. Weisstein, Levenberg-Marquardt Method, http://mathworld.wolfram.com/Levenberg-MarquardtMethod.html.

98 K. LEVENBERG, *Q. Appl. Math.*, 1944, **2**, 164–168.

99 D. Marquardt, *J. Soc. Ind. Appl. Math.*, 1963, **11**, 431–441.

100 A. Dogariu, A. Kuzmich and L. J. Wang, *Phys. Rev. A*, 2001, **63**, 053806.

101 M. K. Aydinol, A. F. Kohan, G. Ceder, K. Cho and J. Joannopoulos, *Phys. Rev. B*, 1997, **56**, 1354–1365.

102 K. Kushida and K. Kuriyama, *Appl. Phys. Lett.*, 2000, **77**, 4154.

103 X. Sun, P. V. Radovanovic and B. Cui, *New J. Chem.*, 2015, **39**, 38–63.

104 T. Yuan, Z. Tan, C. Ma, J. Yang, Z.-F. Ma and S. Zheng, *Adv. Energy Mater.*, 2017, **7**, 1601625.

105 D. W. Murphy, R. J. Cava, S. M. Zahurak and A. Santoro, *Solid State Ionics*, 1983, **9–10**, 413–417.

106 M. Wagemaker, D. R. Simon, E. M. Kelder, J. Schoonman, C. Ringpfeil, U. Haake, D. Lützenkirchen-Hecht, R. Frahm and F. M. Mulder, *Adv. Mater.*, 2006, **18**, 3169–3173.

107 X. Lu, L. Zhao, X. He, R. Xiao, L. Gu, Y.-S. Hu, H. Li, Z. Wang, X. Duan, L. Chen, J. Maier

and Y. Ikuhara, *Adv. Mater.*, 2012, **24**, 3233–3238.

108 C. Y. Ouyang, Z. Y. Zhong and M. S. Lei, *Electrochem. commun.*, 2007, **9**, 1107–1112.

109 S. Bach, J. . Pereira-Ramos and N. Baffier, *J. Power Sources*, 1999, **81**–**82**, 273–276.

110 A. Nugroho, S. J. Kim, K. Y. Chung, B.-W. Cho, Y.-W. Lee and J. Kim, *Electrochem. commun.*, 2011, **13**, 650–653.

111 T. Yuan, R. Cai, K. Wang, R. Ran, S. Liu and Z. Shao, *Ceram. Int.*, 2009, **35**, 1757–1768.

112 T. Yuan, K. Wang, R. Cai, R. Ran and Z. Shao, *J. Alloys Compd.*, 2009, **477**, 665–672.

113 A. S. Prakash, P. Manikandan, K. Ramesha, M. Sathiya, J.-M. Tarascon and A. K. Shukla, *Chem. Mater.*, 2010, **22**, 2857–2863.

114 M. W. Raja, S. Mahanty, M. Kundu and R. N. Basu, *J. Alloys Compd.*, 2009, **468**, 258–262.

115 J. Wang, H. Zhao, Y. Wen, J. Xie, Q. Xia, T. Zhang, Z. Zeng and X. Du, *Electrochim. Acta*, 2013, **113**, 679–685.

116 C. Jamin, K. Traina, D. Eskenazi, N. Krins, R. Cloots, B. Vertruyen and F. Boschini, *Mater. Res. Bull.*, 2013, **48**, 4641–4646.

117 F. O. Ernst, H. K. Kammler, A. Roessler, S. E. Pratsinis, W. J. Stark, J. Ufheil and P. Novák, *Mater. Chem. Phys.*, 2007, **101**, 372–378.

118 C.-L. Wang, Y. C. Liao, F. C. Hsu, N. H. Tai and M. K. Wu, *J. Electrochem. Soc.*, 2005, **152**, A653.

119 J. Deng, Z. Lu, I. Belharouak, K. Amine and C. Y. Chung, *J. Power Sources*, 2009, **193**, 816–821.

120 F. Wunde, F. Berkemeier and G. Schmitz, *J. Power Sources*, 2012, **215**, 109–115.

121 J. Xie, P.-P. R. M. L. Harks, D. Li, L. H. J. Raijmakers and P. H. L. Notten, *Solid State Ionics*, 2016, **287**, 83–88.

122 X. Yu, R. Wang, Y. He, Y. Hu, H. Li and X. Huang, *Electrochem. Solid-State Lett.*, 2010, **13**, J99.

123 J. Mandal, S. Du, M. Dontigny, K. Zaghib, N. Yu and Y. Yang, *Adv. Funct. Mater.*, 2018, **28**, 1802180.

124 P.-E. Lippens, M. Womes, P. Kubiak, J.-C. Jumas and J. Olivier-Fourcade, *Solid State Sci.*, 2004, **6**, 161–166.

125 D. Liu, C. Ouyang, J. Shu, J. Jiang, Z. Wang and L. Chen, *Phys. Status Solidi*, 2006, **243**, 1835–1841.

126 P. P. -c. Tsai, W.-D. W.-D. Hsu and S. S. -k. Lin, *J. Electrochem. Soc.*, 2014, **161**, A439–A444.

127 A. Samin, M. Kurth and L. Cao, *AIP Adv.*, 2015, **5**, 047110.

128 Y. Liu, J. Lian, Z. Sun, M. Zhao, Y. Shi and H. Song, *Chem. Phys. Lett.*, 2017, **677**, 114–119.

129 L. Sarantuya, G. Sevjidsuren, P. Altantsog and N. Tsogbadrakh, *Solid State Phenom.*, 2018, **271**, 9–17.

130 M. Li, T. Gould, Z. Su and S. Zhang, , DOI:10.26434/chemrxiv.7685651.v1.

131 M. G. Verde, L. Baggetto, N. Balke, G. M. Veith, J. K. Seo, Z. Wang and Y. S. Meng, *ACS Nano*, 2016, **10**, 4312–4321.

132 M. Li, T. Gould, Z. Su, S. Li, F. Pan and S. Zhang, *Appl. Phys. Lett.*, 2019, **115**, 073902.

133 Same as E2

134 F. H. Wunde, Der Westfälischen Wilhelms-Universität Münster, 2015.

135 M. Klinger and A. Jäger, *J. Appl. Crystallogr.*, 2015, **48**, 2012–2018.

136 K. M. Colbow, J. R. Dahn and R. R. Haering, *J. Power Sources*, 1989, **26**, 397–402.

137 B. Zhao, R. Ran, M. Liu and Z. Shao, *Mater. Sci. Eng. R Reports*, 2015, **98**, 1–71.

138 H.-C. Chiu, X. Lu, J. Zhou, L. Gu, J. Reid, R. Gauvin, K. Zaghib and G. P. Demopoulos, *Adv. Energy Mater.*, 2017, **7**, 1601825.

139 Y. H. Rho and K. Kanamura, *Key Eng. Mater.*, 2003, **248**, 155–160.

140 Y. Shen, J. R. Eltzholtz and B. B. Iversen, *Chem. Mater.*, 2013, **25**, 5023–5030.

141 M. Muñ Oz-Castro, N. Walter, J. K. Prü, W. Pernice and H. Bracht, , DOI:10.1021/acsphotonics.8b01708.

142 A. Bideau-Mehu, Y. Guern, R. Abjean and A. Johannin-Gilles, *J. Quant. Spectrosc. Radiat. Transf.*, 1981, **25**, 395–402.

143 T. Larsén, *Zeitschrift für Phys.*, 1934, **88**, 389–394.

144 H. H. Yudar, S. Pat, Ş. Korkmaz, S. Özen and Z. Pat, *Part. Sci. Technol.*, 2017, 1–6.

145 M. Zhao, J. Lian, Y. Jia, K. Jin, L. Xu, Z. Hu, X. Yang and S. Kang, *Opt. Mater. Express*, 2016, **6**, 3366.

146 S. Özen, V. Şenay, S. Pat and Ş. Korkmaz, *J. Phys. D. Appl. Phys.*, 2016, **49**, 105303.

147 Y. R. Jhan and J. G. Duh, *Electrochim. Acta*, 2012, **63**, 9–15.

148 D. G. Kellerman, N. A. Mukhina, N. A. Zhuravlev, M. S. Valova and V. S. Gorshkov, *Phys. Solid State*, 2010, **52**, 459–464.

149 T. Kostlánová, J. Dědeček and P. Krtil, *Electrochim. Acta*, 2007, **52**, 1847–1856.

150 C.-W. Chang-Jian, B.-C. Ho, C.-K. Chung, J.-A. Chou, C.-L. Chung, J.-H. Huang, J.-H. Huang and Y.-S. Hsiao, *Ceram. Int.*, 2018, **44**, 23063–23072.

151 C. A. Fenstermaker and F. L. McCrackin, *Surf. Sci.*, 1969, **16**, 85–96.

152 E. E. Chain and D. M. Byrne, *Thin Solid Films*, 1989, **181**, 323–332.

153 D. M. Cunha, T. A. Hendriks, A. Vasileiadis, C. M. Vos, T. Verhallen, D. P. Singh, M. Wagemaker and M. Huijben, *Cite This ACS Appl. Energy Mater*, 2019, **2**, 3410–3418.

154 C. Kim, N. S. Norberg, C. T. Alexander, R. Kostecki and J. Cabana, *Adv. Funct. Mater.*, 2013, **23**, 1214–1222.

155 M. Wilkening, W. Iwaniak, J. Heine, V. Epp, A. Kleinert, M. Behrens, G. Nuspl, W. Bensch and P. Heitjans, *Phys. Chem. Chem. Phys.*, 2007, **9**, 6199.

156 M. Vijayakumar, S. Kerisit, K. M. Rosso, S. D. Burton, J. A. Sears, Z. Yang, G. L. Graff, J. Liu and J. Hu, *J. Power Sources*, 2011, **196**, 2211–2220.

157 H. Hain, M. Scheuermann, R. Heinzmann, L. Wünsche, H. Hahn and S. Indris, *Solid State Nucl. Magn. Reson.*, 2012, **42**, 9–16.

158 Y. C. Chen, C. Y. Ouyang, L. J. Song and Z. L. Sun, *Electrochim. Acta*, 2011, **56**, 6084–6088.

159 B. Ziebarth, M. Klinsmann, T. Eckl and C. Elsässer, *Phys. Rev. B - Condens. Matter Mater. Phys.*, 2014, **89**, 174301.

160 M. Muñoz-Castro, F. Berkemeier, G. Schmitz, A. Buchheit and H.-D. Wiemhöfer, *J. Appl. Phys.*, 2016, **120**, 135106.

161 M. Rubin, K. Von Rottkay, S.-J. J. Wen, N. Özer and J. Slack, *Sol. Energy Mater. Sol. Cells*, 1998, **54**, 49–57.

162 L. G. Harrison, *Trans. Faraday Soc.*, 1961, **57**, 1191.

163 D. A. Porter, K. E. Easterling and M. Y. Sherif, *Phase transformations in metals and alloys, third edition*, CRC Press, 2009.

164 C. Wagner, *Acta Metall.*, 1969, **17**, 99–107.

165 M. Okugawa and H. Numakura, *Metall. Mater. Trans. A Phys. Metall. Mater. Sci.*, 2015, **46**, 3813–3814.

166 F. Ernst, A. Avishai, H. Kahn, X. Gu, G. M. Michal and A. H. Heuer, in *Metallurgical and Materials Transactions A: Physical Metallurgy and Materials Science*, Springer, 2009, vol. 40, pp. 1768–1780.

167 J. Crank and E. P. J. Crank, *The Mathematics of Diffusion*, Clarendon Press, 1979.

168 W. Schmidt and M. Wilkening, *J. Phys. Chem. C*, 2016, **120**, 11372–11381.

169 W. Zhang, D. H. Seo, T. Chen, L. Wu, M. Topsakal, Y. Zhu, D. Lu, G. Ceder and F. Wang, *Science (80-.).*, 2020, **367**, 1030–1034.

170 J. C. Slater, *Quantum Theory of Molecules and Solid*, Wiley, New York, Volume 4., 1974.

171 F. W. Averill and D. E. Ellis, *J. Chem. Phys.*, 1973, **59**, 6412–6418.

172 H. Adachi, M. Tsukada and C. Satoko, *J. Phys. Soc. Japan*, 1978, **45**, 875–883.

173 M. Methfessel, M. Van Schilfgaarde and R. A. Casali, *Electron. Struct. Phys. Prop.*

Solids, 2000, **535**, 114–147.

174 J. Heyd, G. E. Scuseria and M. Ernzerhof, *J. Chem. Phys.*, 2003, **118**, 8207–8215.

175 J. Paier, M. Marsman, K. Hummer, G. Kresse, I. C. Gerber and J. G. Ángyán, *J. Chem. Phys.*, 2006, **124**, 154709.

176 M. J. Young, A. M. Holder, S. M. George and C. B. Musgrave, *Chem. Mater.*, 2015, **27**, 1172–1180.

Appendix

1. Relative intensity profiles and concentration profiles at 45° and 55°C

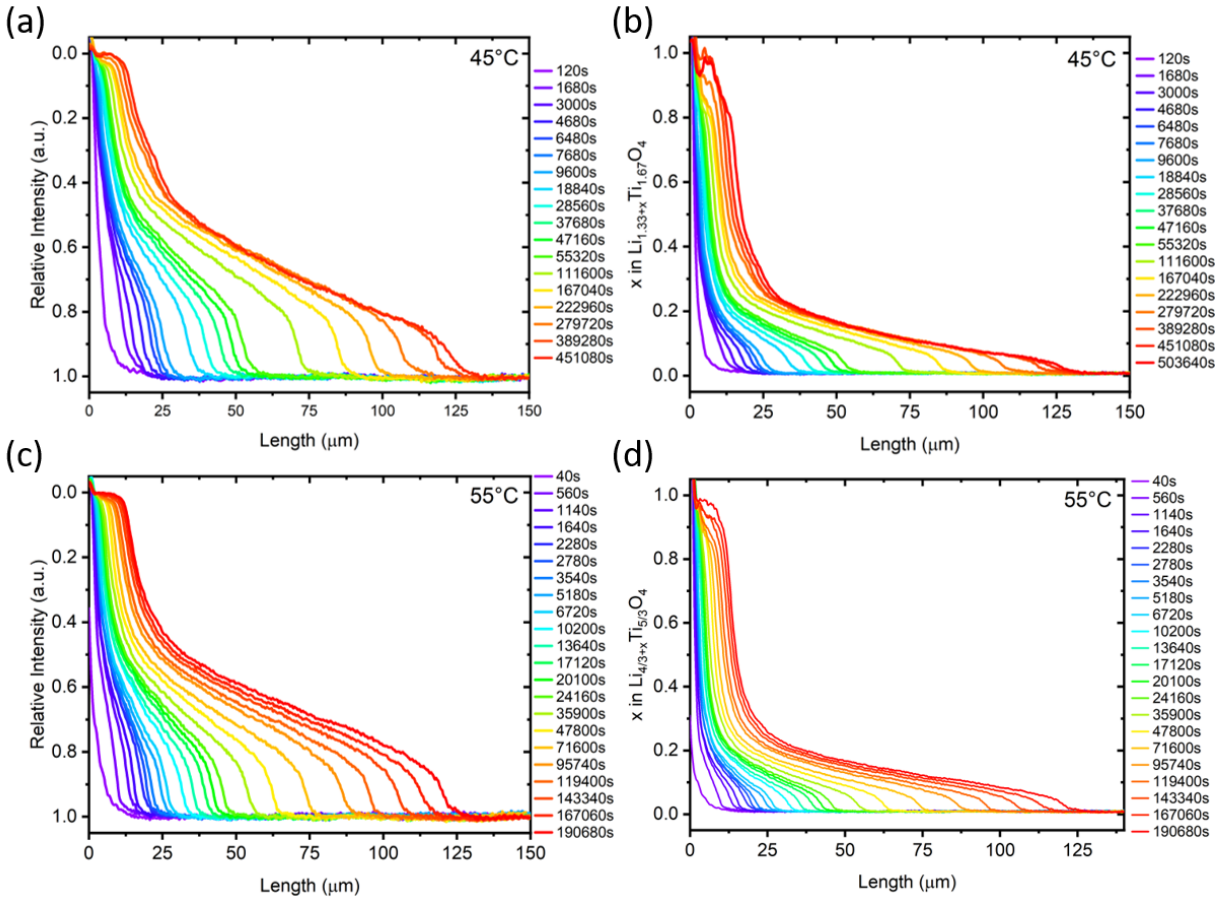

Figure a1: *(a) Relative intensity profile obtained from electrochromic imaging at (a) 45°C and (c) 55°C. (b) and (d) are the concentration profile obtained by using the same calibration curve as in Figure 5-5 (b) for 45°C and 55°C, respectively.*

The relative intensity profiles measured at the other two temperatures are shown in Figure a1 (a) and (c). These profiles are converted into the concentration profiles using the same calibration curve as in Figure 5-5 (b) of the main text. The corresponding concentration profiles are presented in Figure a1 (b) and (d) for 45°C and 55°C, respectively. Using these concentration profiles, the kinetics of phase propagation is determined in Figure 5-6 (a) and (b) of the main text.

List of Figures

List of Tables

List of Abbreviations

EC: Electrochromic

EM: Electromagnetic

CRI: Complex Refractive Index

SIMS: Secondary ion mass spectroscopy

AES: Auger electron spectroscopy

EIS: Electrochemical impedance spectroscopy

PITT: Potentiostatic intermittent transition technique

GITT: Galvanostatic intermittent transition technique

NMR: Nuclear magnetic resonance

r.f.: Radio Frequency

UHV: Ultra high vacuum

XRD: X-ray diffraction

TEM: Transmission electron microscope/y

SEM: Scanning electron microscope

SAED: Selected area electron diffraction

CV: Cyclic voltammetry

CP: Chronopotentiometry

CA: Chronoamperometry

LMO: Lithium manganese oxide

WE: Working Electrode

CE: Counter Electrode

RE: Reference Electrode

DOS: Density of states

LTO: Lithium titanate or $Li_{4/3}Ti_{5/3}O_4$ or $Li_4Ti_5O_{12}$

CDF: complex dielectric function

GAADS: general area detection diffraction system

EC: Ethylene carbonate

DMC: Dimethyl carbonate

PEEK: Polyether ether ketone

PGMEA: propylene glycol monomethyl ether acetate

OCV: Open-circuit voltage

UV: Ultravoilet

Vis: Visible

IR: Infrared

NIR: Near infrared

List of Symbols

$\boldsymbol{z}$: Number of ion exchanged

$\Delta \boldsymbol{G^0}$: Change in Gibbs free energy

$\mathbf{F}$: Faraday's constant

$\boldsymbol{Q_{th}}$: Specific gravimetric capacity

$\mathbf{M_w}$: Molecular weight

$\boldsymbol{E_\lambda}$: Energy of EM radiation

$\mathbf{h}$: Plank's constant

$\mathbf{c}$: Speed of light in vacuum

$\boldsymbol{\lambda}$: Wavelength of EM wave

$\boldsymbol{\nu}$: Frequency of electromagnetic radiation

$\boldsymbol{n_l^*}$: Complex refractive index of 'l' medium

$\boldsymbol{n_l}$: Real part of complex refractive index of 'l' medium

$\boldsymbol{k_l}$: Imaginary part of complex refractive index of 'l' medium

$\boldsymbol{\omega_o}$: Natural frequency of electron

$\boldsymbol{k_E}$: Spring constant corresponding to the restoring force of the nucleus.

$\boldsymbol{N}$: Number of electron per unit volume

$\mathbf{q_e}$: Charge of an electron

$\boldsymbol{f_j}$: Strength of a j^{th} oscillator

$\boldsymbol{\epsilon_o}$: Permittivity of free space

$\boldsymbol{m_e}$: Mass of an electron

$\boldsymbol{\omega_{0j}}$: Resonant angular frequency of a j^{th} oscillator

$\boldsymbol{\omega}$: Angular frequency of the EM wave

$\boldsymbol{\gamma_j}$: Damping factor of j^{th} oscillator

$\boldsymbol{\lambda_{0j}}$: Resonant wavelength of j^{th} oscillator

$\boldsymbol{r_{lm}}$: Fresnel's reflection coefficient for light going through medium 'l' to 'm'

$\boldsymbol{J}$: Atomic flux

$\boldsymbol{D}$: Diffusion coefficient

$\boldsymbol{\kappa}$: Barrier Coefficient

$\boldsymbol{C}$: Atomic concentration

$\boldsymbol{M}$: Mobility of atoms

$\boldsymbol{k_b}$: Boltzmann constant

$\boldsymbol{c}$: Atomic fraction

$\boldsymbol{\mu}$: Chemical potential

$\boldsymbol{I}$: Current

$\boldsymbol{I_0}$: Exchange current

$\boldsymbol{\alpha}$: Charge transfer coefficient

$\boldsymbol{\eta_{eff}}$: Effective over potential

$\boldsymbol{\Delta\phi}$: Potential difference

$\boldsymbol{a_j}$: Activity of the medium j

$\boldsymbol{E^0}$: Standard cell potential

$\boldsymbol{i_{ion}}$: Current density of ionic species

$\boldsymbol{i_{eon}}$: Current density of electrons

$\boldsymbol{\nabla c_{ion}}$: Gradient in ionic concentration

$\boldsymbol{\nabla c_{eon}}$: Gradient in electronic concentration

$\boldsymbol{D_{ieon}^{chem}}$: Common chemical diffusion coefficient in a medium with

comparable kinetics of ions an electrons.

$\boldsymbol{t_{ion}}$: Ionic transference number

$\boldsymbol{t_{eon}}$: Electronic transference number

$\boldsymbol{d}$: Interatomic planar spacing

$\boldsymbol{\theta}$: Angle between the x-rays and the interatomic plane

$\boldsymbol{y}$: Order of reflection in XRD

v: Scan Rate in CV

$\boldsymbol{Ref}$: Reflectance

δ: Thickness of thin-film

$\boldsymbol{R^2}$*:* Quality of fit

$\boldsymbol{\Delta\varphi}$: Change of phase of light

$\boldsymbol{I.L.}$: Insertion loss

$\boldsymbol{E.R.}$: Extinction ratio

$\boldsymbol{\varepsilon_\gamma}$*:* CDF of γ phase

$\boldsymbol{\varepsilon'_\gamma}$: Real part of CDF in γ phase

$\boldsymbol{\varepsilon''_\gamma}$: Imaginary part of CDF in γ phase

$\boldsymbol{f_{Li4Ti5O12}}$: Phase fraction of $Li_4Ti_5O_{12}$

$\boldsymbol{f_{Li7Ti5O12}}$: Phase fraction of $Li_7Ti_5O_{12}$

$\boldsymbol{w}$: Width of Li-rich phase in $Li_{4/3+x}Ti_{5/3}O_4$

$\boldsymbol{\nu}$: Jump frequencies

T: Temperature

Liability agreement

I hereby certify that the dissertation entitled:

“Li-ion transport and optical modulation in thin-film battery electrodes”

is entirely my own work except where otherwise indicated. Passages and ideas from other sources have been clearly indicated.

Ich versichere, dass ich die vorliegende Arbeit mit dem Titel:

“Li-ion transport and optical modulation in thin-film battery electrodes”

selbständig verfasst und keine anderen als die angegebenen Quellen und Hilfsmittel benutzt habe; aus fremden Quellen entnommene Passagen und Gedanken sind als solche kenntlich gemacht.

Ort, Datum

Yug Joshi

Acknowledgement

I would like to thank and dedicate this work to my late father whom I lost during the course of my PhD. I really miss you dad. Wherever you are I hope you are happy. And obviously I also want to thank my mom who played an equally important role as well. Without your constant support I wouldn't have been able to reach this stage of my life. Also I would like to thanks my sister for being there in difficult times.

Prof. Guido Schmitz, I cannot thank you enough for giving me an opportunity to learn and grow in your shadows. I am grateful for all the fruitful discussions we have had and hopefully many more to come. I also want to express my gratitude to Prof. Joachim Maier for the deeply insightful comments and suggestions which helped me to improve this work. I want to acknowledge Prof. Oliver Clemens for taking out the time, to read my thesis and conducting my PhD defense. I would also like to thank Prof. P. K. Ghosh for all the help/encouragement at the end of Masters and in the beginning of my PhD.

I am thankful to Sam and Ke for sharing the responsibility for the Lab-Courses, Helena, Jianshu, Ahmed, Yoonhee and Kuan for the fruitful discussion. I also want to thank Robert for the regular office gossip and many fruitful discussions and also for all the TEM work you did for me and my students. I would specially like to thank Efi and Susann who helped me a quite lot in the beginning of my PhD.

I am also grateful to Peter and Frank for helping me in designing new experiments and for helping me to maintain the glovebox. I also would like to thank Jackie for taking out the time for all the requests that I came with. I also want to express my gratitude to all the students I have supervised during the course of my PhD, you guys really helped me to grow and develop my skills as a supervisor.

And finally I want to thank my girlfriend (and hopefully soon my wife) Dr. Aparna Saksena, I am grateful for everything you have done in making me a better person.

List of publications (2017-2021)

1. Juliane Mürter, Susann Nowak, Efi Hadjixenophontos, Yug Joshi, Guido Schmitz, "*Grain boundary transport in sputter-deposited nanometric thin films of lithium manganese oxide",* Nano Energy **43**, 2018, pp. 340-350. https://doi.org/10.1016/j.nanoen.2017.11.038.
2. Yug Joshi, Efi Hadjixenophontos, Susann Nowak, Robert Lawitzki, Prakriti K. Ghosh, Guido Schmitz, "*Modulation of the Optical Properties of Lithium Manganese Oxide via Li-Ion De/Intercalation*", Advanced Optical Materials **6**, 2018, pp 1701362. https://doi.org/10.1002/adom.201701362.
3. Janina Trück, Efi Hadjixenophontos, Yug Joshi, Gunter Richter, Patrick Stender, Guido Schmitz, "*Ionic conductivity of melt-frozen $LiBH_4$ films*", RSC Advances **9**, 2019, pp 38855-38859. https://doi.org/10.1039/C9RA06821J.
4. Henry A. Müller, Yug Joshi, Efi Hadjixenophontos, Claudia Peter, Gábor Csiszár, Gunther Richter, Guido Schmitz, "*High capacity rock salt type Li2MnO3−δ thin film battery electrodes*", RSC Advances **10**, 2020, pp. 3636-3645. https://doi.org/10.1039/C9RA10125J.
5. Yug Joshi, Aparna Saksena, Efi Hadjixenophontos, Jochen M. Schneider, Guido Schmitz, "*Electrochromic Behavior and Phase Transformation in Li4+xTi5O12 upon Lithium-Ion Deintercalation/Intercalation*", ACS Applied Materials & Interfaces **12**, 2020, pp. 10616-10625. https://doi.org/10.1021/acsami.9b19683.
6. Tobias Kohler, Efi Hadjixenophontos, Yug Joshi, Ke Wang, Guido Schmitz, "*Reversible oxide formation during cycling of Si anodes*", Nano Energy **84**, 2021, pp. 105886. https://doi.org/10.1016/j.nanoen.2021.105886.
7. Yug Joshi, Robert Lawitzki, Guido Schmitz, "*Slow-Moving Phase Boundary in $Li_{4/3+x}Ti_{5/3}O_4$*", Small Methods (Accepted), 2021.

Curriculum vitae

PERSONAL INFORMATION

Yug Joshi

In der Halde 25, 71063 Sindelfingen, Germany
+49-17668745821
yug19891@gmail.com
Sex Male | Date of Birth 19 August 1991

WORK EXPERIENCE

2017-Present Research Assistant

May 2012-July 2012 Industrial Training on Turbine construction
Bharat Heavy Electricals Limited

EDUCATION

2017-Present PhD with Prof. Guido Schmitz, Chair of Material Physics, Institute of Materials Science, University of Stuttgart.

Thesis title: Li-ION TRANSPORT AND OPTICAL MODULATION IN THIN-FILM BATTERY ELECTRODES

2014-2016 Master of Technology in Materials Engineering
IIT Roorkee, India
DAAD-IIT Masters sandwich program
- Master thesis carried out in Stuttgart, Germany in the Institute of Material Science, University of Stuttgart for a period of 7 months

2009-2013 Bachelor of Technology in Mechanical Engineering
Panjab University, India

PERSONAL SKILLS

Mother Tongue: Hindi

Other Languages	Understanding		Speaking		Writing
	Listening	Reading	Spoken Interaction	Spoken Production	
- English	C1	C1	B2	B2	B2
- German	A2	A2	A1	A1	A1

Levels: A1/A2: Basic user; B1/B2: Independent user; C1/C2: Proficient user

Communication Skills: Good communication in English, gained throughout my schooling and university life

Job/ Experimental Skills

- Ion beam sputtering: DC and RF source
- Transmission electron microscopy
- Scanning electron microscopy
- FIB-Liftout for TEM Lamellas
- X-ray diffractometer
- Potentiostat: Bio-Logic (EC lab); Gamry Interface 1000
- UV-Vis-NIR spectroscopy
- UTM: universal testing Machine
- White light interferometer

Digital Competence

- Competent with MS Office Programs
- Computer programming and data analysis using
  - Wolfram Mathematica
  - Originlab Origin
  - C programming